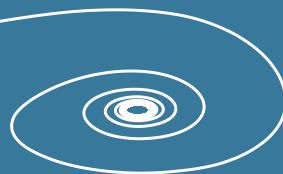


Visualization and measurements of the flow around scaled beach houses

Elise M.P. Leusink



MSC THESIS
DECEMBER 2016

Visualization and measurements of the flow around
scaled beach houses

Author:	Elise M.P. Leusink
Contact:	06 11211890
Graduation supervisor:	dr. K.M. Wijnberg Water Engineering and Management, University of Twente
Daily supervisor:	dr. ir. R. Hagmeijer Engineering Fluid Dynamics, University of Twente

This thesis is dedicated to my father Benno

Abstract

Coastal dunes are crucial elements of the flood defence system of the Netherlands. Windblown sand transport plays a key role in their morphodynamics. Currently, arrays of beach houses are arising in front on the dunes and they act as obstacles in the flow field. It is unknown what effect this has on the evolution of the dunes. The houses are bluff bodies, which are the opposite of streamlined bodies. In this thesis bluff body aerodynamics are reviewed. Bluff body flow is characterized by complex flow structures, e.g. vortices, which arise due to flow separation. In order to understand the effects of the beach houses on the evolution of the dunes it is necessary to first study the flow topology.

This study presents the development of a quantitative flow visualization setup using relatively simple devices to study this flow topology. It comprises a high speed imaging system using 2 moderate speed cameras and a special purpose control system. The high speed imaging system is capable of capturing image pairs with a time interval between $1.5 - 80\mu\text{s}$ and illumination times can be varied between $800\text{ns} - 80\mu\text{s}$. Therefore it can be used for a wide velocity range.

To visualize the flow fields, a tracer particle is required. The feasibility of using smoke as a tracer particle is investigated. The smoke was illuminated by the means of a laser sheet. It is found that in a configuration where two cameras are used smoke is not a suitable tracer particle for quantitative flow visualization. Because the two cameras view the scene from a different angle, both cameras see a different portion of the smoke outside the light sheet. This induced artefacts in the data which could not successfully be removed.

To translate the data obtained to a velocity field, two algorithms have been evaluated. The performance of a particle image velocimetry (PIV) algorithm was compared to that of an Optical Flow estimation (OFE) algorithm. A PIV algorithm calculates a correlation matrix between interrogation areas of two consecutive images. OFE relies on a global method and tracks regions of constant intensity in two consecutive images. Additionally it assumes smoothness of the flow. To assess the effectiveness of the two algorithms, a smoke image was warped with a known displacement field and the relative error was calculated for the PIV and OFE calculation. The OFE algorithm outperformed the PIV algorithm. The calculation resulted in much smaller errors and much denser vector fields. However when using OFE on the real data it tends to overestimate the velocity values.

Acknowledgements

After a year of hard work I can finally start writing the Acknowledgements. This means that the work is almost done! But without the help of many people I would not have been able to complete this project. It is my pleasure to thank everyone involved.

First of all I would like to thank my supervisors Kathelijne Wijnberg and Rob Hagmeijer for their valuable input and thorough feedback during the graduation process, the confidence they had in the project but also for showing understanding for my personal situation. Besides this, I would like to thank you Kathelijne for giving me the opportunity –without knowing me– to conduct a self-proposed project on the beach of Terschelling. This project was very important for me as an artist and a preceding project to my graduation research. Rob, I would also like to thank you for the meetings where we explored the relevant fluid mechanic topics (my favourite subject during my studies), which have been very instructive. I also appreciate your attitude towards the working process, you once referred to the quote *”Soms moet je studenten een beetje laten dwalen en als ze dan verdwalen moet je ze weer naar het juiste pad leiden”*, which fits very well with how I like to work. Additionally, I am grateful for the moments that you took the time to give me confidence in the project again when I myself wasn’t too sure about it.

Second I would like to thank the technicians of the Engineering Fluid Dynamics group, Steven Wanrooij, Herman Stobbe and Wouter den Breeijen for their support during the project. In addition to this, Steven, I would like to thank you for introducing all the new materials and their properties and teach me to work in the metal workshop, the nicest workshop I have ever worked. Herman, thank you for your help every time when we had to remove/install the wind tunnel test section, and in particular for learning me hoisting.

A special thanks goes to Frans Segerink from the Optical Sciences group. Frans, you designed and constructed a key element of my setup: The timer box. Without this it would not have been possible to develop the quantitative flow visualization setup. Also thanks for sharing knowledge about topics regarding optics and for contributing to solutions regarding the project. I greatly appreciate the collaboration. In general I would also like to thank the Optical Sciences group for willing to collaborate and also for providing devices for the experimental investigation.

I would like to acknowledge the Water Engineering and Management group for making this assignment available, and in particular the Engineering Fluid Dynamics group for facilitating the assignment. Additionally, I am grateful to the group not only for the great support but also for providing such a nice working environment. I felt very at home at the department and in the lab!

Above all, I would like to thank Andries Lohmeijer from the company KITT engineering for providing two cameras with optics, which were essential devices for the experimental setup. In addition to this, Andries, I appreciate your support and that you came to the test facility to help me when I was stuck.

Besides, I would like to thank the students who were also working in the lab. During experimental work one sometimes encounters problems, and since we’re all

in the same boat it was nice to have some people to sprout with. But most of all it was nice to give each other a helping hand or to think along with each other projects.

Furthermore, there were a lot of people from other research groups, situated in the West-Horst, who were willing to help me or give me advice when necessary. Among these are technicians, researches and the people from the workshop. I would also like to thank all of you!

Last but not least I would like to thank my family, friends and the people who care for me. Your faith, encouragement and support comforted me during my studies and graduation period, especially during the time I was not feeling very happy. I also appreciate it very much that with some of you I could discuss topics regarding the content of my work. The people I want to name especially are Cor&Denise for their valuable advice and discussions regarding my work but also regarding the academic world, and my Mum: Thank you for all your support over the years, and above all, Mum without you this all would not have been possible!

Thanks!

Contents

Abstract	v
Acknowledgements	vi
1 Introduction	1
1.1 Motivation	1
1.2 From a full scale to a scaled problem	1
1.3 Velocity measurements	3
1.4 Aim and objectives	3
2 Aerodynamics of bluff bodies	5
2.1 Flow separation	5
2.1.1 Boundary layer separation	5
2.1.2 Separation at sharp corners	6
2.2 Flow around prisms	6
2.3 Flow around low-aspect-ratio prisms	7
2.3.1 Upstream: Separation region	8
2.3.2 Flow around the sides and over the free-end	9
2.3.3 Downstream: Wake zone and reattachment	10
2.3.4 Influence of angle of attack	10
2.4 Interference effects	11
2.4.1 Tandem arrangement	11
2.4.2 Side-by-side arrangement	12
2.5 Influence of the boundary layer	13
2.6 Reynolds number (in)dependency	14
2.7 Conclusion	15
3 Background experimental techniques	16
3.1 Principles of hot-wire anemometry	16
3.2 Concepts of image based velocimetry	18
3.2.1 Particle image velocimetry	18
3.2.2 Optical Flow Estimation	25
4 Design implementation experimental setup	29
4.1 Scale model	29
4.2 Hot-wire setup	31
4.3 Flow visualization setup	31
4.3.1 Smoke generator	32

4.3.2	Light source	32
4.3.3	Camera and optics	34
4.3.4	Control system	36
4.3.5	Calibration procedure	37
4.3.6	Timing and optimization of the system	38
4.3.7	Experiments test matrix	40
5	Data analysis & results	41
5.1	HWA: Validation of temperature corrections	41
5.2	PIV	45
5.2.1	Upstream velocity profile	46
5.2.2	Vortex detection	49
5.2.3	Vortex velocity profile	51
5.3	Smoke visualization	52
5.3.1	Image deformation	53
5.3.2	PIV algorithm analysis	55
5.3.3	OFE algorithm analysis	56
5.3.4	Results on smoke image pair	58
6	Discussion	64
6.1	Limitations of the quantitative flow visualization setup	64
6.2	More advanced equipment	66
6.3	Optical flow algorithm	66
6.4	Practical issues	66
7	Conclusions & recommendations	67
7.1	Conclusions	67
7.2	Recommendations	68
7.2.1	Alternative configurations image based velocimetry	68
7.2.2	Visualization of pressure gradients	69
7.2.3	Velocity measurements and sediment transport experiments	69
A	Thwaites' Method	70
B	Laser diode and timer box schematics	72
C	Vortex detection algorithm	76
D	Optical flow vector fields	77
	References	80

Chapter 1

Introduction

1.1 Motivation

Coastal dunes are natural sandy structures and windblown sand transport plays a key role in their morphodynamics. A large part of the Dutch coast is protected against flooding by dunes and they are therefore essential elements of the coastal flood defence system.

Currently the Dutch policy in maintaining coastal safety standards is based on maintaining the location of the Basal Coast Line, which was defined in the year 1990. If the Momentary Coastline tends to move landwards, the sand budget is supplemented by the means of shore-face or beach nourishments. This approach relies on the natural forces of the wind and the waves to transport the sand towards the dunes. This approach has proven to be successful and a large part of the coastal coastline stays in place or is expanding seawards (*Kustlijnkaarten 2015, 2014*).

The strength of the dunes depends primarily on their sand volume and height. Dune safety is assessed with the DUROS-plus model (van de Graaff et al., 2007) where expected erosion, due to a design storm event, is calculated. The remaining dune volume and height should be sufficient for the dune to be safe. Currently arrays of beach holiday houses are arising in front of the dunes along the Dutch coast. These houses act as obstacles in the flow field. As wind is the driving force of aeolian sand transport, these houses modify the natural sediment transport processes. Yet the impact of this modified flow field on dune evolution is not known.

Because dunes in the Netherlands are an important defence against flooding by sea, it is of major interest for Rijkswaterstaat to know the effects of these holiday houses on dune evolution. Since Rijkswaterstaat is the responsible authority, they are now facing the problem to define regulations with respect to the type and position of these houses. It is therefore necessary to understand how these houses will affect the airflow and the related sand transport. Which type, orientation, position and spacing of the houses will ensure the optimal circumstances for dune evolution?

1.2 From a full scale to a scaled problem

As a starting point in understanding the influences of beach holiday houses on the related sand transport it is of interest how the beach holiday houses modify the airflow. Flow around these type of bluff bodies can be investigated by means of



Figure 1.1: (a) Beach holiday house array. Photo adopted from Beeldbank Rijkswaterstaat. (b) Bed form visualization with crates. Photo from experiments conducted on the beach of Terschelling.

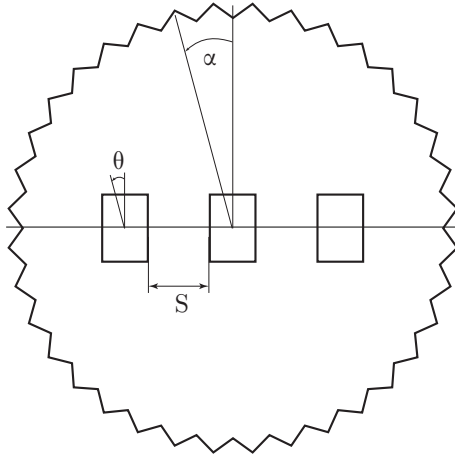


Figure 1.2: schematic representation of the parameters: angle of attack α , orientation angle θ and the spacing S . Note the differences between α and θ : α describes the relative angle of the whole setup, while θ describes the relative angle of the single bluff bodies.

wind tunnel experiments, computational fluid dynamics (CFD) or with field studies. CFD simulations may provide detailed simulated data of the flow field, however it remains difficult to properly simulate the turbulence in the flow. Field studies are complicated by the highly variable conditions in the field, and isolation of important parameters is very difficult. Under laboratory conditions, on the contrary, the important parameters can be varied systematically and influence of the relevant parameters can be isolated. We therefore choose to investigate the flow by means of scaled wind tunnel experiments.

For scaled experiments it's important to consider the geometry of the beach holiday houses. These holiday houses may have various forms: The classical square with a triangle on top of it, i.e., how a child would draw a house. They may also have the shape of a box, or more complicated shapes. But in general the houses are small 1 family sized houses. To not further complicate the problem, a simple geometry will be chosen where a block having the aspect ratio of a shoe box may well represent a simple beach holiday house.

The overall wind direction in the full scale case may change direction in time scales of days. For this reason an important parameter to investigate is the angle

of attack α . With respect to the Rijkswaterstaat question concerning the optimal orientation and spacing of such an array of beach holiday houses, the two main other parameters of interest are the orientation θ of the houses, and the spacing S in between the houses. See figure 1.2 for a schematic representation of these parameters.

1.3 Velocity measurements

As described in previous section we are interested in the airflow around the holiday houses. Insight in the flow field can be obtained by performing velocity measurements. By the start of present research the only available technique in the test facility to measure velocities was the hot wire anemometry. A flow visualization technique was also available which is only able to capture qualitative information of the flow. We wish to obtain quantitative information of the flow, since this can be linked to expected instantaneous sand transport. This section describes the type of velocity measurements that can be conducted with this type of instruments, and identifies the additional development needed for quantitative flow visualization measurements.

Hot wire anemometry Hot wire anemometry (HWA) is a technique to measure flow speeds with a very high temporal resolution (see section 3.1 for a more detailed description of this technique). Unfortunately it is a single-point measurement technique. Besides this it is also incapable of distinguishing the direction of the flow. For this reason it is not suitable to study the complex flow structures associated with bluff body flow. However, this technique can be used to perform single-point measurements to validate the results obtained from the flow visualization setup.

Quantitative flow visualization setup Since we are interested in the flow structures associated with bluff body flow we wish to obtain whole field measurements. A technique which is capable of doing so is particle image velocimetry (PIV). Section 3.2.1 describes this technique in more detail. It is an image based velocimetry which records with a high speed camera the displacement of tracer particles added to the flow. A PIV apparatus was not available in the test facility at the start of this research. The qualitative flow visualization setup, which was available, comprises a LED sheet as illumination source, a smoke generator to inject seeding particles to the flow and an imaging device. To this extend we investigate the feasibility of modifying the current flow visualization setup to a quantitative one, inspired by the working principle of a PIV system.

1.4 Aim and objectives

The aim of present study is stated as follows:

To develop a quantitative flow visualization setup using relative simple devices to study airflow around beach holiday houses taking the qualitative visualization system as a starting point.

In order to achieve the aim stated above, the following objectives need to be fulfilled.

1. Investigate the possibility of using smoke as a tracer particle for a quantitative flow visualization setup.
2. Develop a high speed imaging system, based on one or two moderate speed cameras and a special purpose control system.
3. Evaluate different algorithms to translate the measured data to sufficiently accurate velocity fields.
4. Validate the measurements using hot-wire anemometry.
5. Investigate the sensitivities of vortex structures with respect to the orientation and configurations of a beach house array.

In view of time, objectives 4 and 5 have not been completed within the present investigation. Objective 4 was stagnated by validation of the hot-wire measurements itself. A start with objective 5 has been made by constructing a scale model of a beach house array. Besides this a pilot PIV measurement made it possible to partly study vortex structures in the vicinity of a single house.

Objectives 1–3 have been reformulated into the following research questions which will be addressed in this thesis.

1. To what extend can smoke be used as a tracer particle for a quantitative flow visualization setup?
2. To what extend can a high speed imaging system be developed using one or two moderate speed cameras and a special control system?
3. How do different algorithms perform in translating the measured data to sufficient accurate velocity fields?

Chapter 2

Aerodynamics of bluff bodies

In this chapter a literature review is presented regarding aerodynamics of bluff bodies. Beach holiday houses are bluff bodies, which are the opposite of streamlined bodies. Bluff body flow is characterized by complex flow structures, e.g. vortices, which arise due to flow separation. The pressure gradients which arise due to these vortices affect sediment transport, therefore these vortical structures are particularly of interest with respect to the Rijkswaterstaat question.

This section is organized as follows. First some general aspect concerning flow separation will be discussed. Subsequently time averaged flow and some instantaneous flow patterns around cubic bodies will be described. Next the influence of the angle of attack will be shortly named. Whereafter interference effects of tandem and side-by-side arrangements will be discussed. Some influence of the flow conditions will be noted and finally the gap regarding the knowledge on bluff body flow will be briefly discussed.

2.1 Flow separation

In order to understand the complex flow structures around bluff bodies, it's useful to first consider the main mechanisms behind flow separation. Flow separation always occurs by the presence of an adverse pressure gradient, i.e., in the opposite direction of the main flow (Lawson, 2001; Sychev, Ruban, Sychev, & Korolev, 1998). This will be further explained below. The point where the separation occurs is defined as the *separation point*. This point is unsteady, therefore it is more accurate to define it as a *separation zone* which bounds the positions of the separation points. The main –and active– flow flows over the separated flow. The region beneath the active air is often referred to as *separation bubble*, where the flow has a rotating nature. Further downstream from the separation point the adverse pressure gradient reduces and the flow reattaches at the *reattachment point*. This closes the bubble. If there is not sufficient distance along the surface, reattachment does not occur (Lawson, 2001).

2.1.1 Boundary layer separation

Prandtl was the first to explain flow separation on the basis of his boundary layer theory. Consider a flow over a surface with a thin boundary layer and an outer

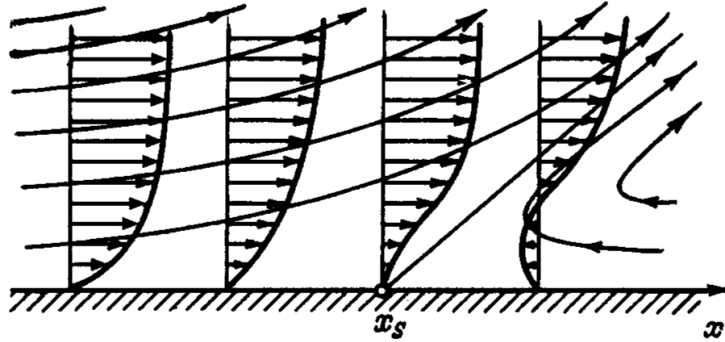


Figure 2.1: Boundary layer flow near the separation point x_s . Figure adopted from Sychev et al. (1998).

potential flow. The no-slip condition requires the fluid to have a zero tangential velocity at the surface. Inside the boundary layer the fluid velocity increases from zero to the velocity outside the boundary layer. All the shear is contained inside the boundary layer and the potential flow is free of shear. As a general rule by Bernoulli's law in potential flow the pressure is high where flow velocity is low and vice versa. Thus, if the flow outside the boundary layer is decelerating, this induces an adverse pressure gradient in the flow just outside the boundary layer. According to Prandtl's boundary layer equations there is no pressure drop inside the boundary layer. Therefore the pressure inside the boundary layer equals the pressure of the flow just outside of it. The flow inside the boundary layer tends to flow in the direction of lower pressure, changing the velocity profile in the boundary layer. Ultimately there exists a point where the shear at the surface equals zero. This is the point where the flow separates, depicted as x_s in figure 2.1 (Lawson, 2001; Sychev et al., 1998).

2.1.2 Separation at sharp corners

When flow flows around a convex corner, i.e., a corner with an interior angle smaller than π (corners in figure 2.4 are examples of convex corners), the flow ultimately separates. To understand this a potential flow will be considered around a convex corner. According to potential flow theory the velocity of the flow is proportional to $\sim r^\alpha$, where $\alpha < 0$ for a convex corner and r is the distance to the corner. This implies an unrealistic infinite large velocity at the corner. According to Bernoulli's law the pressure at this point is infinitely small. The boundary layer adjacent to the wall, directly below the corner, is then subjected to an infinite large adverse pressure gradient causing the flow to separate at the corner. This flow separation does not occur if the corner angle is close to π and the adverse pressure gradient is not sufficient for boundary layer separation (Kundu & Cohen, 2008; Sychev et al., 1998).

2.2 Flow around prisms

Due to the common occurrence of bluff bodies in engineering applications flow around these type of bodies has been studied extensively (McClellan & Summer,

2014). The simplest form of bluff body flow is its two-dimensional equivalent. This two-dimensional flow is studied by placing "infinite" prisms vertically in the flow.

To this extent no distinction has been made between circular or rectangular cross-sections, however it is widely agreed that the main flow features are similar in both flows (Luo, Chew, & Ng, 2003). A circular cross section doesn't have any sharp corners and separation occurs purely due to the mechanism described in section 2.1.1.

As mentioned above, bluff body flows are characterized by unsteady phenomena due to flow separation. Flow separation in the two-dimensional case, for $Re > 40$, leads to periodic vortex shedding from the two sides of the cylinder, which is known to form a Kármán vortex street (McClellan & Summer, 2014). This vortex street is stable for the low Reynolds number range and shows unstable behaviour as the Reynolds number increases.

However many prism like structures employed in engineering applications, e.g., the beach holiday houses, can be better approximated as finite surface-mounted prisms where there is flow over the ground and the free end and their shape has a three-dimensional rather than a two-dimensional character. End-effects start to play a role, and flow around a finite prism differs drastically from flow around a two-dimensional prism (Wang & Zhou, 2009).

The typical flow structures in the near wake of a ground-mounted finite cylinder depend strongly on the ratio between height h and cross stream width w of the prism. As the height decreases, the flow over the free end and the flow over the ground are becoming more important mechanisms in the flow. Below a critical h/w the vortex shedding changes from an asymmetrical Kármán vortex street to a symmetrical arch shaped vortex. This critical value lays somewhere between 2-6, depending on circumstances, and the down wash due to the flow over the free end dominates the wake (Wang & Zhou, 2009). See figures 2.2 and 2.3 for a schematic representation of the flow structures in the different aspect ratio regimes.

2.3 Flow around low-aspect-ratio prisms

Various authors have studied the flow around three-dimensional surface-mounted obstacles with aspect ratios below the critical value, e.g. the studies by Becker, Lienhart, and Durst (2002); Callaud, Davd, and Texier (2005); Lacey and Rennie (2012); Lim, Castro, and Hoxey (2007); R. Martinuzzi and Tropea (1993); Pattenden, Turnock, and Zhang (2005); Sakamoto (1982). R. Martinuzzi and Tropea (1993) were one of the first to provide a general description of the flow around low-aspect-ratio three-dimensional obstacles, placed normal oriented to the flow. The main time-averaged flow features identified by R. Martinuzzi and Tropea (1993) are shown in figure 2.3. These flow features are valid for height-to-width aspect ratios (h/w) below the critical value $\sim 2 - 6$, described in the previous section, and above a critical value of $\sim \frac{1}{4} - \frac{1}{6}$ (R. Martinuzzi & Tropea, 1993). A beach holiday house has an aspect ratio within this range. The flow can be divided into three sections, from which the mean and some time dependence flow features are described below.

- (i) The region upstream from the obstacle where the main flow separates.
- (ii) The flow around the sides and over the free-end.

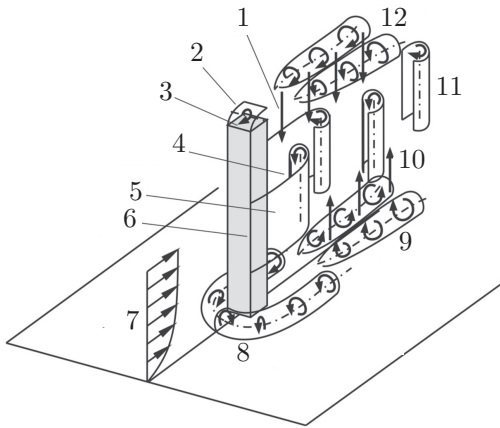


Figure 2.2: Time averaged flow structures around a prism with an aspect ratio higher than the critical value. Numbers correspond to: (1) Downwash, (2) recirculation zone on free-end surface, (3) separation from leading edge on free end, (4) Kármán vortex formation, (5) shear layer, (6) separation from leading corners, (7) boundary layer, (8) horseshoe vortex at prism-wall junction, (9) base vortex structures, (10) upwash, (11) shed Kármán vortex and (12) tip vortex structures. Figure adapted from McClean and Summer (2014)

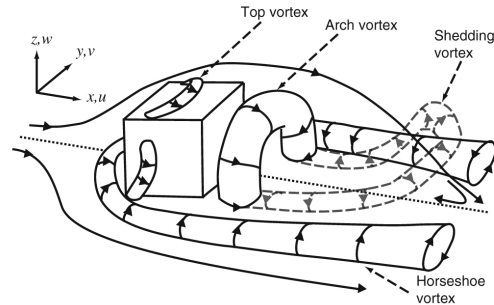


Figure 2.3: Time averaged flow structures around a cube which has an aspect ratio below the critical value. Adapted from Lacey and Rennie (2012)

- (iii) The region downstream of the obstacle, which is characterized by the wake and reattachment of the mean flow.

2.3.1 Upstream: Separation region

In the region upstream of the obstacle the flow separates. This flow separation occurs due to the adverse pressure gradient in the boundary layer adjacent to the wall induced by the stagnating flow. In this separation region the flow is characterized as alternating in between two modes. In one mode the fluid is deflected back upstream in a jet. The fluid moves against oncoming flow, which results in dissipation of energy. As the fluid loses its energy it rolls up to form a series of up to four vortices, and hereby switching to the second mode (R. Martinuzzi & Tropea, 1993).

The stagnation flow impinging on the front face of the obstacle induces a negative vertical pressure gradient, see figure 2.4. This pressure gradient induces the system of vortices to spin down the upstream face of the obstacle (Lacey & Rennie, 2012). The pressure gradient created by the flow around the corners directs the fluid around the obstacle, as depicted in the left of figure 2.4. Hence the system of vortices extends over the entire width and bends around the obstacle to form a horseshoe shaped vortex which extends downstream from the obstacle resulting in two counter rotating vortices downstream of the obstacle. The horseshoe vortex outlines the wake zone (Lacey & Rennie, 2012; R. Martinuzzi & Tropea, 1993).

The unsteady nature of the flow in the separation region, which is confirmed by the study of Pattenden et al. (2005), results in unequally sized recirculation regions. R. Martinuzzi and Tropea (1993) suggest that this implies that the mass flux to the sides of the obstacle is irregular, which is, according to them, a typical feature of

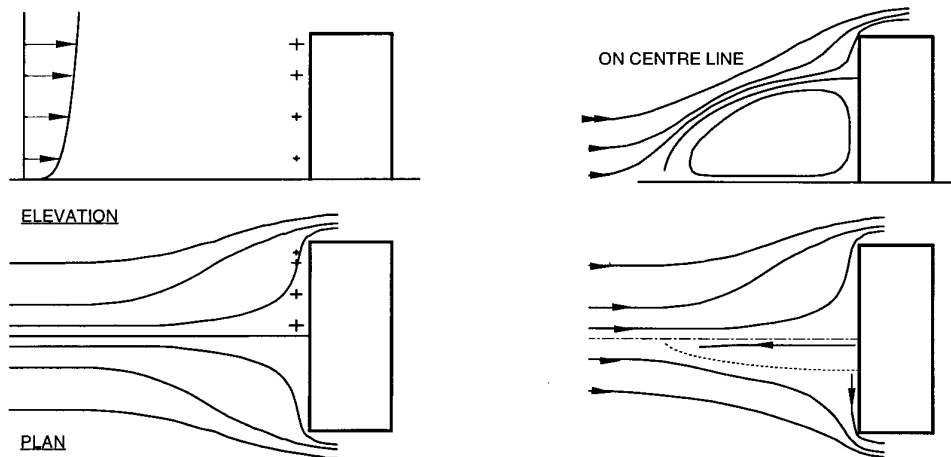


Figure 2.4: Streamlines of stagnating flow in front of a building, with the induced pressure gradient depicted with plus signs (*left*) and the three-dimensional flow caused by this pressure gradient (*right*). Figure adapted from Lawson (2001).

three-dimensional flows.

2.3.2 Flow around the sides and over the free-end

Pattenden et al. (2005) have studied the flow over a surface mounted low-aspect ratio circular cylinder. They concluded from oil film visualizations and PIV measurements, that flow separation due to the sharp leading edge of the obstacle leads to a complex three-dimensional separation bubble. In this separation bubble on top of the obstacle they observed an arch shaped vortex with its bases connected to the top of the obstacle. The presence of this arch shaped vortex is confirmed by the study by Callaud et al. (2005). If no reattachment occurs on top of the obstacle, the arch vortex travels further downstream through the center of the wake.

Downstream from this recirculation region the flow reattaches on top of the obstacle or not. This depends on circumstances like the width-to-height ratio and upstream flow conditions. Flow separation due to the sharp sides generates vortices on the side and the top which interact to form tip vortices at the corners of the free-end (Pattenden et al., 2005). Perhaps these tip vortices interact with the wake to form the arch shaped vortex behind the obstacle.

Callaud et al. (2005) observed in their experiments no reattachment on top of the obstacle. The width of their object was larger than the height and according to R. Martinuzzi and Tropea (1993) the streamwise reattachment length increases as the width of the object increases. Callaud et al. (2005) found the arch vortex, generated on top of the block, to stretch towards the wake. This stretching occurs until its base disunites from the surface and a cyclic vortex shedding phenomena is generated. The Reynolds number in their experiments, based on the model's width was 1000.

2.3.3 Downstream: Wake zone and reattachment

Between the separation point and the point where the main flow reattaches, there is a region of back flow which wraps into the arch vortex. Calluaud et al. (2005) observed two different evolutions of this arch vortex in the same experiment. In the first process they identified first an arch vortex generated on top of the obstacle that detaches from the top face, grows and while it is convected in downstream direction it's altitude decreases. A new vortex generated on top of the obstacle merges with the old vortex while it travels downstream. The new merged vortex escapes towards the wake. The wake resulting from process 1 contained a symmetric topology. In the second process no merging is observed. The vortex originated from the top escapes towards the wake, while maintaining it's altitude. The mechanism of this process is not cyclic. Furthermore, the topology of the wake resulting from process 2 was found to be dissymmetric, in contrast to the symmetric wake topology resulting from process 1. They also concluded that process 1 was dominant compared to process 2.

The tip vortices aligned in streamwise direction appear to be pushed down by the downwash behind the cylinder (Pattenden et al., 2005). According to Wang and Zhou (2009) this downwash is associated with the tip vortices. The circulation of the top vortices is in opposite direction. When two vortices are close to each other in a flow, they interact with each other. Two counter rotating vortices, with direction of rotation as depicted in figure 2.2, induce a downward velocity on each other (Kundu & Cohen, 2008). This might be an explanation for the downwash behind the obstacle.

The ends of the horseshoe vortex interact with the wake and R. Martinuzzi and Tropea (1993) have observed cross-stream velocity components in the wake up to at least 20 heights downstream. The influence of the horseshoe vortex decreases as the width of the object increases, due to the distance between the ends of the horseshoe vortex being further apart. Consequently this results in weaker cross-stream velocity components in the wake (R. Martinuzzi & Tropea, 1993).

The circulation of the arch vortex entrains the surrounding fluid to the axis of symmetry. The shear layer reattaches downstream of this circulation region at the reattachment point. Between the obstacle and upstream of the reattachment point the width of the wake decreases due to the circulation of the arch vortex. R. Martinuzzi and Tropea (1993) observed expansion of the wake after the reattachment point, which they explained by the increase in mass flux –due to shear layer reattachment– close to the wall, which subsequently is entrained by the horseshoe vortex.

2.3.4 Influence of angle of attack

The influence of angle of attack was investigated by various authors. The influence can be summarized as follows. Up to an angle of attack $\alpha = 45^\circ$ degrees the bases of the arch vortex are present. The location of these bases are asymmetric for $0 < \alpha < 45^\circ$ degrees. Besides, α influences the location of the stagnation, separation and attachment point and the width of the wake increases as α increases for $\alpha < 45^\circ$ degrees (Sakamoto, 1982). In addition to this, the near body flow is dominated by strong vortices generated from the top leading edges, these are shed from the body and induce a stronger down wash in the wake for the case $\alpha = 45^\circ$ degrees compared to the case where $\alpha = 0^\circ$ degrees (Castro & Robins, 1977).

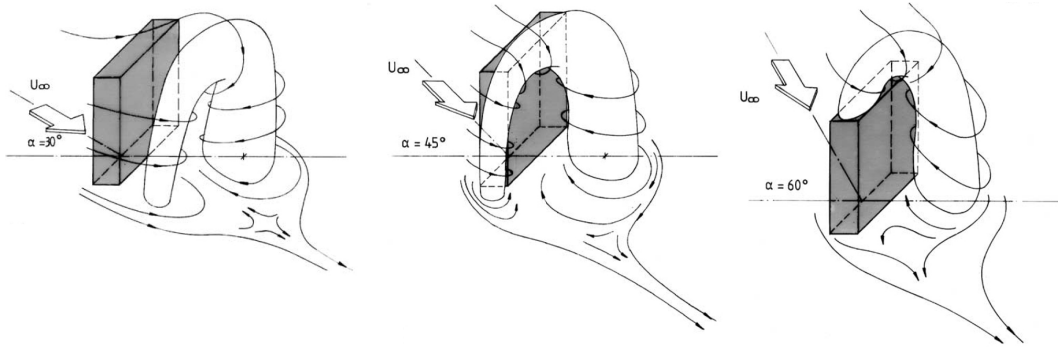


Figure 2.5: Arch vortex topology for various angles of attack. Figure adopted from Becker et al. (2002).

The arch vortex topology proposed by R. Martinuzzi and Tropea (1993) was extended to non-zero angles of attack by Becker et al. (2002) and is depicted in figure 2.5. Note the different positions of the arch vortex in this figure, and the location of one of the legs on top of the obstacle for $\alpha = 60^\circ$ degree. They didn't observe the horseshoe vortex downstream of the obstacle in their experiments, which they attribute to merging and dissipation of the vortices in the near wake.

2.4 Interference effects

Multiple bluff body flow is further complicated due to interference of the flow structures described in the previous sections. In contrast to the two-dimensional case, not so many studies have investigated the flow around three-dimensional multiple bodies (Lim & Ohba, 2014; R. J. Martinuzzi & Havel, 2000). Three-dimensional geometries differ fundamentally from two-dimensional geometries because the direction of the vorticity vector –i.e., the direction perpendicular to the rotating flow– can rotate freely and this can reorganize the flow around a downstream structure (R. J. Martinuzzi & Havel, 2000).

2.4.1 Tandem arrangement

Interference effect of 2 tandem prisms have been studied among others by Sakamoto and Haniu (1987) and R. J. Martinuzzi and Havel (2000). In both studies 4 distinct shedding regimes were identified based on obstacle spacing. In each regime the flow separates in front of the upstream obstacle and the separation zone is –not surprisingly– characterized by the horseshoe vortex. However, distinct flow patterns are observed in the region between the two obstacles. For a detailed description of the flow patterns, the reader is referred to the paper by R. J. Martinuzzi and Havel (2000).

In the smallest spacing regime, it was observed that shedding was interrupted by periods of random fluctuations. No periodic shedding was identified in this regime, as separated shear layer from the side of the upstream prism reattach on the sides of the downstream prism. For intermediate spacings, defined as the cavity locked regime by R. J. Martinuzzi and Havel (2000), continuous vortex shedding was observed. In this regime, the main flow reattaches on the leading edge of the downstream cube. In the third regime, the shedding from the downstream prism locks on to that of the

upstream prism, resulting in a synchronized shedding. In this regime the main flow reattaches in front of the downstream obstacle and a horseshoe vortex is generated in the junction of this obstacle. In the fourth regime the prisms were found to shed independently (R. J. Martinuzzi & Havel, 2000; Sakamoto & Haniu, 1987).

The boundaries of the regimes were defined differently in the two papers. These differences may arise from a different geometry of the prism and different upstream flow conditions. R. J. Martinuzzi and Havel (2000) defined the regimes as: (i) $S/H < 1.5$, (ii) $1.5 < S/H < 2.5$, (iii) $4 < S/H < 6$ and (iv) $S/H > 6$ where S is the spacing between the obstacles and H is the obstacle height. The obstacles in their experiments were two surface mounted cubes, placed in a thin boundary layer with thickness $\delta = 0.07H$ for $Re = 2.2 \cdot 10^4$. The regimes by Sakamoto and Haniu (1987) were defined as: (i) $S/W < 2$, (ii) $2 < S/W < 3.5$, (iii) $3.5 < S/H < 15$ and (iv) $15 < S/H < 50$ where W is the obstacle width. The obstacles in their experiments were two tall square cross-section surface mounted prism with a height of $3H$, placed in a turbulent boundary layer with thickness $\delta = 0.8H$ for $Re = 2.2 \cdot 10^4$ based on obstacle width.

R. J. Martinuzzi and Havel (2004) further investigated this locked regime (intermediate spacing), to identify the shedding mechanism. They concluded that shedding occurs due to interaction of the shear layers from the sides of the upstream cube with the downward flow on the front face of the downstream cube. The separation of the shear layers from the sides of the upstream cube induces a pair of counter rotating vortices, the bases of the arch vortex in the time averaged flow. These vortices are advected downstream in an alternating fashion. The base vortex closest to the front face of the downstream cube induces a spanwise velocity of which the direction depends on the circulation of this vortex. As the vortices are counter rotating, the sign of the spanwise velocity switches through the shedding cycle. The interaction with the separation streamlines –i.e., the streamlines which outline the wake– result in attached flow on 1 side of the downstream cube and separated flow on the other side. The downward velocity on the front face is larger where the flow at the side is separated. This downward velocity splits the vortex, resulting in a partly shed vortex downstream. This all occurs in alternating fashion.

2.4.2 Side-by-side arrangement

Sakamoto and Haniu (1987) investigated the interference effects of two tall prisms in a side-by-side arrangement. They report 4 distinctive flow regimes based on obstacle spacing. For small spacings, $S/W < 1.2$, the two prisms behave as one body. The vortices formed from the shear layers from the sides of the prisms interact to form one large scale vortical structure. For slightly larger gaps, $1.2 < S/W < 1.8$, the gap flow suppresses the formation of vortices from the shear layers from the outer sides of both prisms. For intermediate gaps, $1.8 < S/W < 3.0$, they observed the flow around the prisms to be asymmetric. The flow through the gap was directed into the wake behind the first or the second prism. This flow pattern was found to be unstable, i.e., the changes in direction occurred in irregular time intervals. For larger gaps, $S/W > 3$, both prisms shed vortices individually forming their own vortex street. For the gap distances studied, they found both vortex streets to interact.

A numerical modelling study by Lim and Ohba (2014) addressed interference

effects of three wall-mounted cubes submerged in a deep boundary layer. Their study focusses on aerodynamic loads on the cubes and they report little about the flow structure. For the cubes in side-by-side arrangement they report the reattachment length of the separated flow to be the longest for $S = 0.5H$ and the shortest for $S = 3H$ which represents a single cube according to the authors. Furthermore they mention that the vortex structures around the cubes differ with a change in gap distance. For an increase in gap distance, the horseshoe vortices around the cubes separate into individual vortex systems to merge in between the gaps. These structures disappear in the gaps due to the acceleration of the flow in the gaps. This was observed in their simulated data for gap ranges of $S = 0.5H$, $S = 1.0H$ and $S = 1.5H$.

2.5 Influence of the boundary layer

The studies described above were performed under various upstream conditions. The bluff body flow was studied in a fully developed channel flow (R. Martinuzzi & Tropea, 1993), submerged in a deep turbulent boundary layer (Becker et al., 2002; Castro & Robins, 1977; Lacey & Rennie, 2012; Lim et al., 2007; Lim & Ohba, 2014; Sakamoto, 1982; Sakamoto & Haniu, 1987) or with smooth upstream flow conditions and a thin laminar boundary layer (Becker et al., 2002; Callaud et al., 2005; Castro & Robins, 1977; R. J. Martinuzzi & Havel, 2000, 2004; Pattenden et al., 2005). To this extend it is important to define the influence of these different type of boundary layers on the flow properties.

Figure 2.6 shows the time averaged velocity profiles for both types of boundary layers. It is evident from this figure that the turbulent profile is "fuller" and contains more energy. For this reason a turbulent boundary layer is more capable of withstanding an adverse pressure gradient, compared to the laminar boundary layer, and therefore a turbulent boundary layer delays separation, moving the separation point further downstream (Kundu & Cohen, 2008). In other words, a turbulent boundary layer has a larger shear at the surface. Therefore a more severe adverse pressure gradient is necessary to decrease the shear at the surface to zero: the point where flow separation occurs. This reasoning doesn't hold when separation occurs at a sharp corner. As explained before flow will always separate at a sharp corner, the properties of the boundary layer will thus not influence this (Lawson, 2001). Furthermore it should be noted that turbulence influences reattachment, more specific it is the main mechanism in restoring energy into the layers of air adjacent to the surface, resulting in a shorter separation bubble (Lawson, 2001).

The study of Becker et al. (2002) investigated the differences of the flow structure in two types of boundary layers: (i) a simulated atmospheric boundary layer which represents a typical urban environment and (ii) without additional boundary layer simulation. But they don't describe the characteristics of the latter boundary layer. They observed in their visualization experiments that there is no fundamental change in the vortical structures for the different boundary layers, however the dimensions of the flow regimes did differ. The flow in the simulated atmospheric boundary layer showed a shorter reattachment length downstream of the obstacle. This smaller separation bubble was already observed in the study by Castro and Robins (1977), and this observation in both studies agree well with theory. Furthermore, Becker

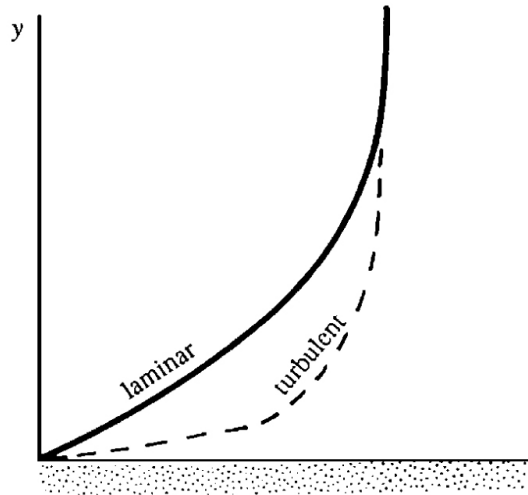


Figure 2.6: Schematic representation of a time averaged laminar and turbulent boundary layer velocity profile. Figure adapted from Kundu and Cohen (2008).

et al. (2002) show that periodic shedding is not observed in the case with the thick turbulent boundary layer in contrast to the periodic shedding observed in the case with the thinner boundary layer.

The study by Castro and Robins (1977) examined flow around a cube in two types of boundary layers – a thick atmospheric turbulent boundary layer of 10 times the body height H and a thin laminar boundary layer of approximately $0.2H$. They further note, in addition to the smaller wake, that in the case of the turbulent boundary layer the wake decays within a distance of six cube heights. They also report that the size and intensity of the upstream horseshoe vortex scale with the thickness of the oncoming boundary layer. Due to the influence of a turbulent boundary layer on the location of the separation point, the size of the upstream horseshoe vortex should be smaller, because separation occurs closer to the obstacle than for a laminar boundary layer.

2.6 Reynolds number (in)dependency

Let's first recap what the Reynolds number is. The Reynolds number – a non dimensional parameter – is defined as UL/ν , where U and L are the typical velocity and length scale in the problem and ν is the kinematic viscosity of the fluid. The Reynolds number is the ratio of inertia forces to viscous forces and the magnitude of the Reynolds number indicates which of those forces are dominant in the flow problem or if they're of equal importance. Two flows are said to be dynamically similar if the dimensionless parameters the flow depends on are equal. Scaled experiments rely on this concept, because data from scaled experiments can be applied to full scale experiments if the dimensionless parameters are kept constant (Kundu & Cohen, 2008). The Reynolds number discussed below is based on the bluff body dimension – e.g. the height or width – and is different from the Reynolds number determining the transition from a laminar to turbulent boundary layer, which is based on the distance along the wall.

It is generally assumed that flow around surface-mounted bluff bodies with sharp

edges is Reynolds number independent, provided that $Re > (2 - 3) \cdot 10^4$. Most previous studies rely on this assumption as the laboratory Reynolds number range is generally a few orders in magnitude smaller than the full scale Reynolds number. The last decade this assumption is being questioned and Lim et al. (2007) have studied explicitly the Reynolds number (in)dependency for flow around a cube submerged in a thick boundary layer, i.e., a turbulent boundary layer. They distinguish two cases defined by cube orientations of zero and 45° degree to the oncoming flow. Where the latter case is the typical example of flow with strong relatively steady concentrated vortex regions over the cube.

They show that in the first case the mean pressure and velocity fields are not significant Re -dependent, but they do observe a Re -dependence on the fluctuating quantities –these are related to shedding frequency. They explain this dependency due to the slowly extending range of scales in the energy spectra as Re increases. For the second case, which they describe as vortex dominated flow, they observe clear Re effects in the mean flow field. These are most evident in the regions close to the vortex cores. Re -dependency on the fluctuating quantities is also observed for this case.

Castro and Robins (1977) observed no Re -effects for flows with turbulent upstream conditions, but they did observe Re -effects in their experiments with smooth upstream conditions. Other studies (Becker et al., 2002; R. J. Martinuzzi & Havel, 2000) however, have observed no Re -dependency in their experiments with smooth upstream conditions on the surface shear stress (for $Re < 5 \cdot 10^4$), shedding frequency (for $3 \cdot 10^3 < Re < 4 \cdot 10^4$) and reattachment length (for $4 \cdot 10^4 < Re < 2 \cdot 10^5$).

The Re -(in)dependency remains a difficult topic to investigate, whereas there remains a fairly large gap between the laboratory range of Reynolds numbers and the Reynolds number in full scale conditions (Lim et al., 2007). Lim et al. (2007) argue that if specific flow properties do depend on the Reynolds number, corrections should be made to the experimental data before it is applicable to full scale conditions. At present it is still unclear how to make such corrections.

2.7 Conclusion

In general the different authors from the papers reviewed above all agree with respect to the time averaged flow structures around single surface mounted prisms. The knowledge about the instantaneous flow structures still seem scattered and deserves future research to obtain a full understanding of the problem. In addition to this, the variations between studies in oncoming flow conditions and bluff body geometries make comparison between the various studies difficult. Furthermore multiple bluff body flow complicates the flow structures, and as noted before, is not that extensively studied. More specifically little is known on the effects of angle of attack and body orientation in combination with spacing between the bluff bodies on vortex characteristics, such as dimensions and strength.

Chapter 3

Background experimental techniques

The purpose of this chapter is to provide the reader of some basic background regarding hot-wire anemometry (HWA), particle image velocimetry (PIV) and optical flow estimation (OFE). For that reason only the basic principles are described. The section on PIV is a bit more detailed, since the quantitative flow visualization setup developed during present study is inspired on the principles of PIV.

3.1 Principles of hot-wire anemometry

HWA was already introduced in the first half of the 20th century and is a measurement technique to measure fluid velocity. It is a single-point measurement and is capable of measuring rapid changing velocity fluctuations due to a very large dynamic response. The thermal inertia of the wire is very small and is further corrected by the anemometer, for this reason it has a very large dynamic response. Hence HWA is a very suitable technique for measuring turbulent fluctuations (McKeona et al., 2007).

A hot-wire is a very small wire, with diameters in the order of μm . Despite it's small dimensions it is an intrusive technique. The sensor material has a resistance which depends on the temperature of the sensor. An electrical current is applied to the wire and the wire is heated due to Joule heating. This heating is primarily lost due to forced convection. As a consequence of this the hot-wire is incapable of distinguishing the direction of the flow. A simplified heat balance is of the form (McKeona et al., 2007)

$$R_w I_w^2 = (T_w - T_a) \phi_{conv}(U, \dots) \quad (3.1)$$

where R_w is the resistance of the wire, I_w is the current through the wire, T_w is the temperature of the wire, T_a is the ambient temperature and ϕ_{conv} is a convection function depending on the fluid velocity U among other parameters. The LHS of the heat balance represents the heating rate and the RHS represents the cooling rate. It is possible to obtain U from R_w and I_w if the relation between resistance R and temperature T is known. This relation is often assumed to be linear and is given by

(McKeona et al., 2007)

$$\begin{aligned} R_w &= R_0(1 + \chi(T_w - T_0)) \\ R_a &= R_0(1 + \chi(T_a - T_0)) \end{aligned} \quad (3.2)$$

where T_0 and R_0 denote the reference temperature and sensor resistance at reference temperature, R_a the resistance at ambient temperature and χ (K^{-1}) is the temperature coefficient of resistivity of the wire material around T_0 . The change in resistance generates a measurable signal. HWA can be operated in 3 modes:

1. The current I_w is kept constant, this is referred to as constant current anemometer (CCA), and R_w can directly be measured.
2. The temperature T_w and thus the resistance R_w is kept constant by a feedback loop. This is referred to as constant temperature anemometer (CTA). The value of the current I_w which is necessary to keep R_w constant can then be measured.
3. The voltage $E_w = R_w I_w$ across the sensor is kept constant. This is referred to as constant voltage anemometer (CVA). The value of the current I_w which is necessary to keep R_w constant can then be measured.

The main difference between these operation modes is the handling of the thermal inertia of the wire. For CCA and CVA this needs to be compensated in the electrical circuit, while for CTA this is already done automatically, as the temperature is kept constant by a feedback loop (McKeona et al., 2007).

The heat balance eq.(3.1) can be written in terms of dimensionless numbers including all the wire and flow parameters.

$$Nu = Nu\left(M, Re, Gr, Pr, \gamma, \frac{T_w - T_a}{T_a}\right) \quad (3.3)$$

where Nu is the Nusselt number, M is the Mach number, Re is the Reynold number, Gr is the Grasshoff number, Pr is the Prandtl number and γ is the ratio of the heat capacities at constant pressure and constant volume (McKeona et al., 2007). The Nusselt number is the ratio total heat transfer to conductive heat transfer and can be defined as

$$Nu = \frac{R_w I_w^2}{\pi l k (T_w - T_a)} \quad (3.4)$$

where l length of the wire and k is the thermal conductivity of the fluid. For incompressible airflows the Mach number M , which represents the ratio of flow velocity to the speed of sound, and γ don't have any influence. Pr is fixed for air for a large temperature range. And Gr , which represents the ratio of buoyancy forces to viscous forces is assumed to be much smaller than Re . Eq.(3.3) then reduces to (McKeona et al., 2007):

$$Nu = Nu\left(Re, \frac{T_w - T_a}{T_a}\right) \quad (3.5)$$

Several heat transfer functions have been proposed from experimental data. One of the more popular ones is of the form

$$Nu = a + bRe^{1/2} \quad (3.6)$$

where a and b are empirical determined values. Using relations eq.(3.2) and eq.(3.4), eq.(3.6) can be rewritten as

$$\frac{R_w I_w^2}{R_w - R_a} = A + BU^{1/2} \quad (3.7)$$

$$\text{with } A = \frac{a\pi lk}{\chi R_0}$$

$$B = \frac{b\pi lk}{\chi R_0} \left(\frac{\rho d}{\mu} \right)^{1/2}.$$

Eq.(3.7) is also known as King's Law. A and B are often referred to as constants, they however do depend on the fluid temperature and wire diameter (McKeona et al., 2007).

The values A and B are to be determined with a calibration procedure. For a single wire only the normal velocity has to be changed. The velocity must be measured with another device, e.g. a pitot static tube. It is common to perform the calibration in 20-30 steps within the selected velocity range. From the obtained data a fit can be calculated using a power law like King's Law. It is also possible to use a polynomial or spline fit between for example the measured voltage E and the flow velocity U (McKeona et al., 2007).

3.2 Concepts of image based velocimetry

Several image based techniques have been developed since the eighties, and the application and development of these techniques has increased quickly when analogue recording and evaluation were replaced by digital methods. Among these methods are laser speckle interferometry, a technique from which particle image velocimetry (PIV) and digital image correlation (DIC) have originated. Laser speckle interferometry was developed to measure deformation and strain for engineering applications: the scatter by coherent light on a surface created a random interference pattern, from which the displacement or strain can be obtained. Digital image correlation strongly resembles this techniques, as the deformation of a speckle pattern applied to a surface can be evaluated from 2 consecutive images. The principle behind particle image velocimetry, where the flow velocity is obtained from a particle displacement, is closely related to the principle behind DIC (Raffel, Willert, Werely, & Kompenhans, 2007). Optical flow estimation (OFE) found its origin in a different field, the field of computer vision. This section describes the basic principles of particle image velocimetry and OFE.

3.2.1 Particle image velocimetry

Particle image velocimetry (PIV) is a very popular tool for quantitative flow visualization. Common fluids like water and air are optically transparent and flow

can be made visible by adding tracer particles to the flow. Even though tracers are added to the flow, PIV is commonly referred to as a non intrusive technique as the requirement of the tracers is to accurately follow the flow. The concept of PIV relies on illuminating these particles and obtaining image pairs with a short Δt between image 1 and image 2. Evaluation of the displacement of the particles gives information on the velocity of the flow. PIV is a measurement technique which is able to capture the velocity on a large number of points simultaneously in contrast to single-point measurements. In this respect it is possible to study coherent flow structures as observed in turbulent flows, which is less straightforward using single-point measurements. Furthermore, the ability to capture the velocity at a large number of points reduces the time needed to acquire experimental data (McKeona et al., 2007).

In the last decades and with the availability of more advanced equipment planar PIV, where only the velocity field in a plane can be obtained, has been extended to more sophisticated methods like stereo and tomographic PIV, extending the analysis from a 2-dimensional flow to a 3-dimensional flow. This section only describes the basic principles behind planar PIV.

Tracer particles

Mechanical properties PIV relies on indirect measurement of fluid velocity. It measures the velocity of the tracer particles rather than the fluid velocity itself. Therefore it is important that the tracer particle follows the flow accurately. The differences of fluid and particle velocity can be estimated by

$$\mathbf{u}_p - \mathbf{u} \simeq \frac{2}{9} \frac{r^2(\rho_p - \rho_f)}{\mu} \frac{d\mathbf{u}_p}{dt} \quad (3.8)$$

and is derived from the Basset-Boussinesq-Oseen equation. In eq. 3.8 \mathbf{u}_p is the particle velocity, \mathbf{u} is the fluid velocity, ρ_p is the density of the particle, ρ_f is the fluid density and r is the particle radius. More details on the derivation is given in McKeona et al. (2007) and references therein. From eq. 3.8 it is clear that the particle follows the fluid flow accurately if $\rho_p = \rho_f$. This condition is easily met for liquid flows, where a wide variety of materials is available and relative large particles can be used. Common used tracer particles of water flows are within the range of $5\mu\text{m} < 2r < 50\mu\text{m}$. For airflows this condition cannot be achieved that easily and a ratio of $\rho_p/\rho_f = O(10^3)$ is commonly used. If $\rho_p \gg \rho_f$ the response time of the particle to variation in the fluid velocity is commonly modelled as exponential decay with a relaxation time given by:

$$\tau = \frac{2}{9} \frac{r^2 \rho_p}{\mu} \quad (3.9)$$

This relaxation time should be smaller than the smallest time scales of the fluid flow (McKeona et al., 2007). From eqs.(3.8-3.9) we see for τ and $(\mathbf{u}_p - \mathbf{u})$ to be small, the size of the particle should be very small. Common used particle diameters are in the order of $1\mu\text{m}$ with a density of 10^3 kg/m^3 . This corresponds to a relaxation time of $\tau = 3\mu\text{s}$ (McKeona et al., 2007).

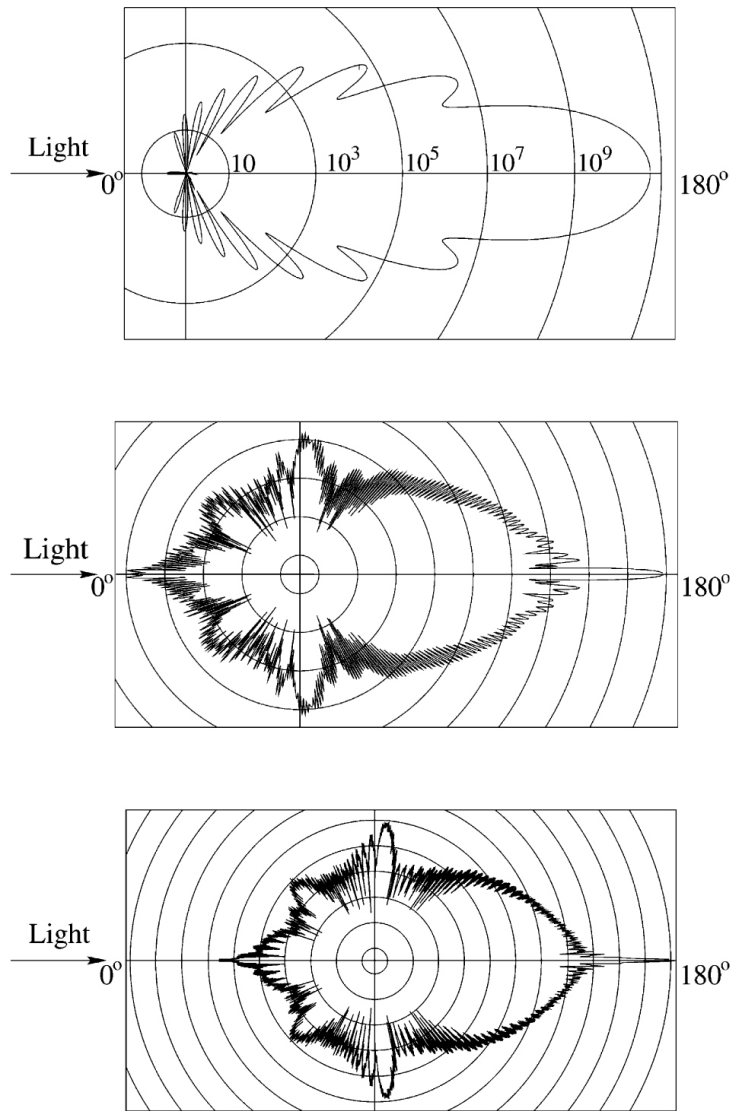


Figure 3.1: Mie scatter diagrams by a glass particle in water. From top to bottom: $d_p = 1 \mu\text{m}$, $d_p = 10 \mu\text{m}$, $d_p = 30 \mu\text{m}$. The radial lines denote the intensity magnitude. Intensity scales of the two lower diagrams are as in upper diagram. Figure adopted from Giancoli (1998).

Scatter properties The particle size should thus be small enough to follow the flow accurately, however, they have to be large enough to scatter enough light to be visible. The common used particle diameters are larger than the wavelength of light λ , this means that they scatter within the Mie regime. The scatter intensity depends on the particle diameter and the ratio of refractive index of the particle to refractive index of surrounding medium. The refractive index of water is higher than that of air, therefore the scatter intensity in air is atleast one order of magnitude higher. In this respect tracer particles used in water flows should be larger compared to air flows (McKeona et al., 2007; Raffel et al., 2007).

Figure 3.1 shows typical Mie scatter diagrams. In this figure it is visible that the scatter amplitude increases as the particle diameter increases. It is also visible that the scatter amplitude is also strongly dependent on the viewing angle. Largest scatter amplitudes can be obtained with viewing angles of 180° degree. However, due to practical reasons a viewing angle of 90° is commonly used (Raffel et al., 2007).

The scatter diagrams also show that de particle doesn't block the light, but it scatters the light in all directions. The particles also receive light scattered from other particles. As the particles are commonly illuminated in a thin light sheet, they benefit from largest scatter amplitude which arises from the 180° degree scatter angle. A high density of tracer particles can thus increase the particle image intensity. There is a limit to this, because a higher particle density also induces more scattering outside the light sheet and therefore increases background noise (Raffel et al., 2007).

Imaging

A typical PIV setup is depicted in figure 3.2. It usually comprises a pulsed illumination source with optics forming a thin light sheet illuminating the particles in the flow and a high speed camera which records the particle pattern and its displacement.

Lasers are a popular light source for PIV. They can produce a pulsed, collimated and monochromatic light beam which can easily be shaped into a thin light sheet. A light sheet is commonly achieved with the use of cylindrical and spherical lenses. Figure 3.3 shows an example of such a configuration using only cylindrical lenses. In this arrangement the first cylindrical lens is used to expand the size of the beam in 1 direction. The light rays are made parallel with the 2nd cylindrical lens and the last cylindrical lens reduces the thickness of the sheet. To minimize erroneous calculations due to out of plane movements, the thickness of the light sheet should be a lot smaller than the width or height of the light sheet, typically in the order of 1% (McKeona et al., 2007).

For good quality PIV recordings it is necessary that the particle images do not contain motion blur. This can be achieved by a short enough illumination or exposure time. A good criterion is that the displacement of the particles should be smaller than the particle itself. A short illumination or duration time also means that less light can be captured by the imaging device. Therefore it is necessary that the intensity of the light sheet is high enough that the particles can be seen by the camera (McKeona et al., 2007).

The imaging device should be able to capture two images with a short enough time interval in between. For time resolved PIV the frame rate of the imaging device should be large enough to capture the details of the flow. A rule of thumb is that the

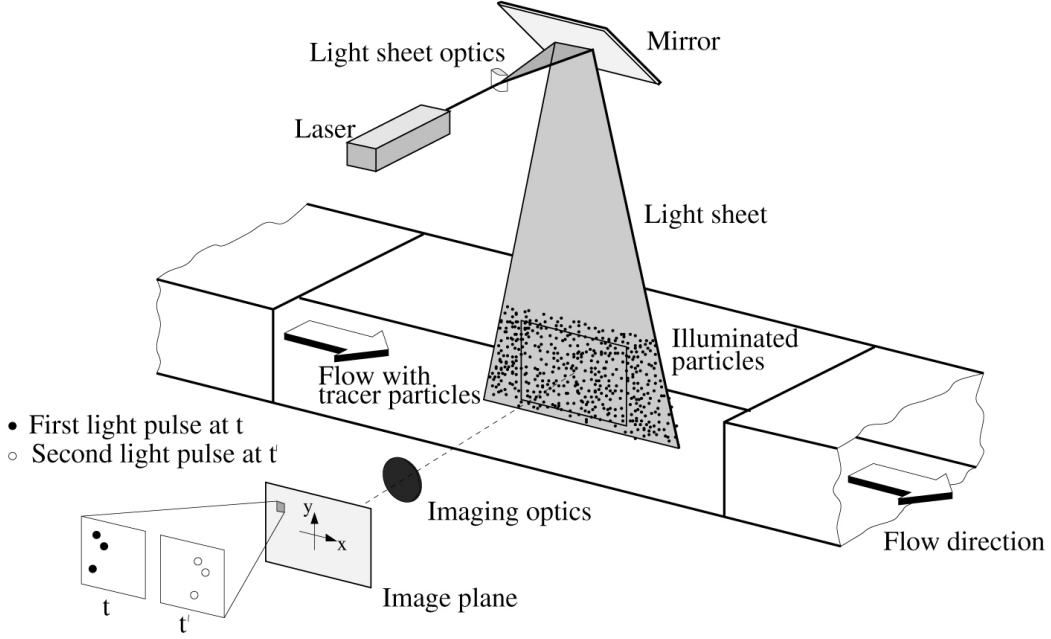


Figure 3.2: Typical PIV setup, figure adopted from Raffel et al. (2007).

particle displacement should be at least 50% smaller than the size of the interrogation area. For image evaluation PIV recordings are divided into sub-windows which are called interrogation areas.

All these considerations limit the spatial and temporal resolution of the system, e.g., the shortest possible time interval between the consecutive images limit the flow velocity or field of view (FOV) which can be studied. An other aspect which limits the spatial resolution of an image is often referred to as diffraction limited imaging. A distinct point source, e.g., a small scattering particle, doesn't appear as a point in the image plane but forms a diffraction pattern. This is a consequence of focussing a parallel beam. For a low exposure recording a small disc, known as the Airy disc can be observed. For high exposure recordings Airy rings are visible around this disc. A large aperture corresponds to a small Airy disc whereas a small aperture corresponds to a large Airy disc. The diameter of the Airy disc d_{diff} represents the smallest particle image d_{τ} that can be obtained for a given configuration. The diameter of the Airy disc depends on the focal number $f_{\#} = f/D_a$ which is the ratio of focal length f and aperture diameter D_a , wavelength of light λ and the magnification factor M which is the ratio of distance of image plane and lens to distance of object plane to lens:

$$d_{\text{diff}} = 2.44f_{\#}(M + 1)\lambda \quad (3.10)$$

The particle image diameter d_{τ} can be approximated as

$$d_{\tau} = \sqrt{(Md_p)^2 + d_{\text{diff}}^2} \quad (3.11)$$

where d_p is the particle diameter. More details on the origin of these equations can be found in Raffel et al. (2007). The first term in the root of eq. 3.11 is named

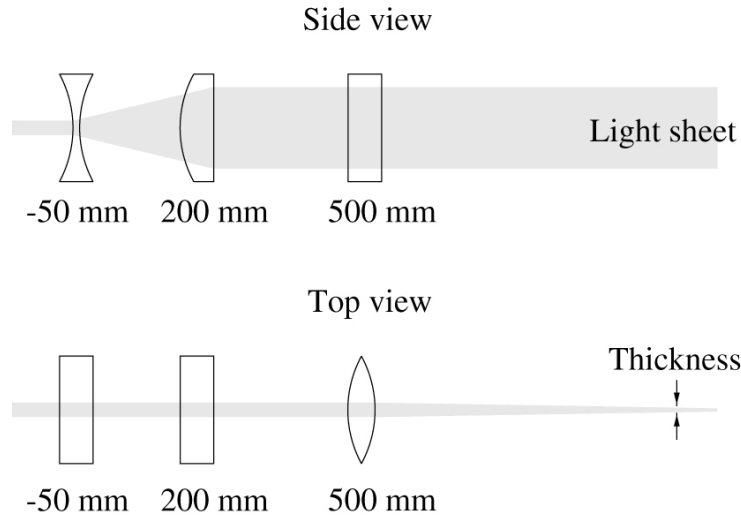


Figure 3.3: Example of a light sheet optics configuration. Figure adopted from Raffel et al. (2007)

the geometric image. From eq. 3.11 is clear that if $Md_p \ll d_{\text{diff}}$ the particle image $d_\tau \simeq d_{\text{diff}}$ and vice versa if $Md_p \gg d_{\text{diff}}$ the particle image $d_\tau \simeq Md_p$.

Data processing

Pre-processing Good quality PIV recordings contain images with (1) homogeneous seeding, (2) uniform illumination and (3) uniform image background. In practice these conditions are usually not perfectly matched. Image enhancement of the data can compensate for this (McKeona et al., 2007). Several image enhancement techniques are available, only a selection of them are described here.

Low- and high-pass filtering are straightforward pre-processing techniques. A high-pass filter can be applied to remove a non-uniform image background. A low-pass filter on images is sometimes referred to as a blurring filter. It removes frequencies above a cut-off frequency. It creates a smoother signal and in images this appears as a blurred image. This can be useful for suppressing noise. *Intensity capping* removes image intensities above a certain threshold. Brighter spots in PIV images contribute more to the correlation peak, which can lead to erroneous image evaluation. *Adaptive histogram equalization* operates on small regions in the image. Most frequent gray values of the image histogram are spread out over the whole range of data. Low and high exposed parts in the image are optimized independent, which result in higher contrast images, also for the regions with small intensity gradients (McKeona et al., 2007; Thielicke & Stamhuis, 2014b).

In some cases image restoration is also required. In PIV recordings deformations might be present due to perspective distortion or lens aberration. In the latter case straight lines become curved lines in the image plane. Image restoration attempts to fix these distortions (McKeona et al., 2007).

Image Evaluation The PIV analysis is based on dividing the image into small interrogation areas and calculating a correlation between the interrogation region of

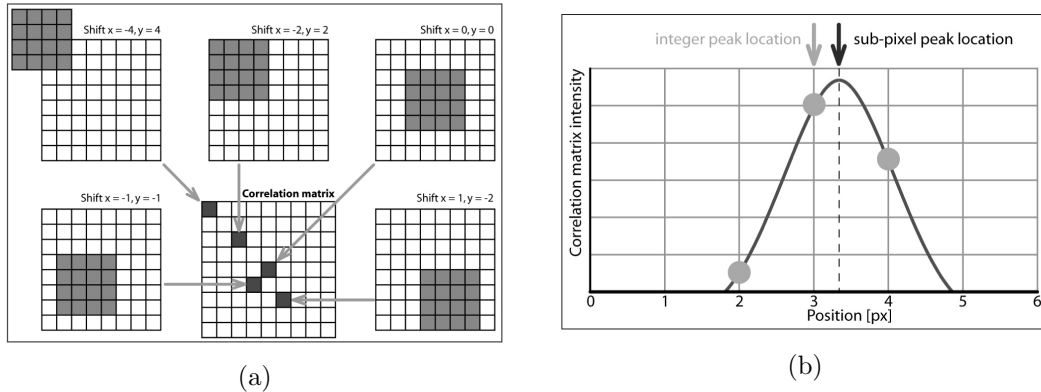


Figure 3.4: (a) Schematics of correlation calculation. (b) Sub-pixel accuracy. Figures adapted from Thielicke and Stamhuis (2014b)

image 1 and 2. This correlation is calculated with the discrete correlation function

$$C(m, n) = \sum_i \sum_j A(i, j) B(i - m, j - m) \quad (3.12)$$

where A and B are the corresponding interrogation areas of image 1 and 2. This correlation can be calculated in the spatial domain, generally referred to as direct cross correlation (DCC), or in the frequency domain, using a discrete Fourier transform (DFT). A schematic representation of how the correlation matrix is computed in the spatial domain is given in figure 3.4a. The correlation matrix C will contain a peak where the correlation is highest, the location of this peak gives the most probably particle displacement from image 1 to image 2 (Thielicke & Stamhuis, 2014b).

The correlation matrix is stored in cells with finite sizes, therefore the location of the peak is an integer value. Sub-pixel accuracy can be achieved by fitting a one- or two-dimensional gaussian to the data in the correlation matrix surrounding the peak. This principle is schematically explained in figure 3.4b.

Particles which have moved out of the interrogation area induce some loss of information. This loss of information induces a larger background noise in the correlation matrix, and therefore a lower peak to noise ratio. This complicates identifying the location of the peak and therefore the accuracy of the analysis decreases. Several window shifting and deformation techniques have been developed. The correlation is then first performed on larger interrogation areas. Here after the displacement is used to shift and/or deform the interrogation area. The shifted and deformed interrogation area is subdivided into smaller windows and a new correlation matrix is calculated. Figure 3.5 depicts an example of this window deformation technique (Thielicke & Stamhuis, 2014b).

Post-processing The correlation procedure will result in a vector field with a resolution equal to the number of interrogation areas. Commonly these vector fields will contain spurious vectors and post-processing is then inevitable. A basic method to filter outliers is to set velocity limits. This can be done manually, or with a standard deviation filter. The threshold is then set within n -standard deviations from the mean velocity value. Where the number n defines the strictness of the filter. A more robust method is to use a local median filter. This filter evaluates the

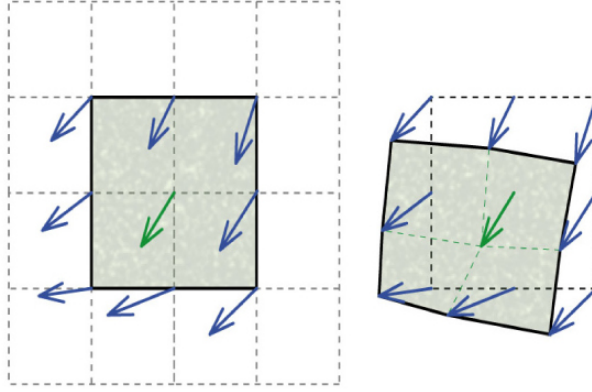


Figure 3.5: Example of how window deformation is performed by PIVlab. Figure adopted from Thielicke and Stamhuis (2014b).

velocity fluctuation around the neighbourhood of a vector. After outliers have been removed data interpolation may be performed to fill in the missing vectors.

3.2.2 Optical Flow Estimation

Optical flow is the apparent motion that arises due to motion of objects and/or the observer in videos or image sequences. The motion in the real world may be 3-dimensional and is projected into a 2-dimensional motion in the image plane. OFE is a tool used widely in the field of computer vision, for applications like 3D shape acquisition, object recognition, object tracking and scene understanding among many others (Fleet & Weiss, 2005).

Several methods have been proposed for OFE, including local methods (e.g, correlation methods, feature tracking) and global methods (e.g., energy based methods, gradient based methods) (Fleet & Weiss, 2005). A large number of optical flow approaches, however, is based on the original formulation of Horn and Schunck (1981). This section will describe the underlying assumptions of this method.

Brightness and smoothness constraint

Let $I(x, y, t)$ denote the intensity of a pixel in an image at time t . The intensity of this pixel is assumed to remain constant when displaced Δx , Δy at time $t + \Delta t$:

$$I(x, y, t) = I(x + \Delta x, y + \Delta y, t + \Delta t) \quad (3.13)$$

A Taylor expansion of the RHS of eq.(3.13) about the point (x, y, t) gives:

$$I(x + \Delta x, y + \Delta y, t + \Delta t) = I(x, y, t) + \Delta x \frac{\partial I}{\partial x} + \Delta y \frac{\partial I}{\partial y} + \Delta t \frac{\partial I}{\partial t} + h.o.t \quad (3.14)$$

Substitution of this approximation in eq.(3.13), dropping higher order terms and rearranging yields

$$I(x, y, t) + \Delta x \frac{\partial I}{\partial x} + \Delta y \frac{\partial I}{\partial y} + \Delta t \frac{\partial I}{\partial t} = I(x, y, t) \quad (3.15)$$

$$\frac{\Delta x}{\Delta t} \frac{\partial I}{\partial x} + \frac{\Delta y}{\Delta t} \frac{\partial I}{\partial y} + \frac{\partial I}{\partial t} = 0 \quad (3.16)$$

Taking the limit as $\Delta x \rightarrow 0$, $\Delta y \rightarrow 0$ and $\Delta t \rightarrow 0$ this becomes

$$\frac{dx}{dt} \frac{\partial I}{\partial x} + \frac{dy}{dt} \frac{\partial I}{\partial y} + \frac{\partial I}{\partial t} = 0. \quad (3.17)$$

Using $u = dx/dt$ and $v = dy/dt$ this leads to

$$u \frac{\partial I}{\partial x} + v \frac{\partial I}{\partial y} + \frac{\partial I}{\partial t} = 0 \quad (3.18)$$

which is also known as the *brightness constraint equation*. In fluid mechanics the LHS of eq.(3.18) is also known as the material derivative. The derivation of eq.(3.18) is after Horn and Schunck (1981).

This brightness constancy assumption is the starting point for many OFEs, however one can imagine many cases where this assumption doesn't hold. For example an object moving towards a light source, the brightness of this object will increase as the distance between the object and light source will decrease. Even though this assumption may seem unrealistic, it seems to work well in practise (Fleet & Weiss, 2005).

The brightness constraint equation (3.18) is one equation with two unknowns. Another constraint is necessary to be able to solve for u and v . Horn and Schunck (1981) introduce a 2nd constraint which assumes smoothness of the optical flow velocity. In cases where objects are subject to rigid movement or deformation this may be a valid assumption. The assumption may break down at the edges of the object or where occlusion between objects finds place. This constraint can be expressed as minimization of the square of the magnitude of the gradient of the optical flow velocity (Horn & Schunck, 1981):

$$|\nabla u|^2 = \left(\frac{\partial u}{\partial x}\right)^2 + \left(\frac{\partial u}{\partial y}\right)^2 \quad (3.19)$$

$$|\nabla v|^2 = \left(\frac{\partial v}{\partial x}\right)^2 + \left(\frac{\partial v}{\partial y}\right)^2 \quad (3.20)$$

Minimization

Even if the brightness constancy assumption is perfectly valid, eq.(3.18) will not equal zero due to noise present in the images. Therefore the problem is to minimize the sum of errors in the brightness constraint equation and to minimize the square of the magnitude of the gradient of the optical flow velocity. The total error to be minimized is then

$$\Phi = \int_{y_0}^{y_N} \int_{x_0}^{x_N} (\lambda^2 \Phi_s^2 + \Phi_i^2) dx dy \quad (3.21)$$

$$\text{where } \Phi_s^2 = \left(\frac{\partial u}{\partial x}\right)^2 + \left(\frac{\partial u}{\partial y}\right)^2 + \left(\frac{\partial v}{\partial x}\right)^2 + \left(\frac{\partial v}{\partial y}\right)^2 \quad (3.22)$$

$$\text{and } \Phi_i = u \frac{\partial I}{\partial x} + v \frac{\partial I}{\partial y} + \frac{\partial I}{\partial t} \quad (3.23)$$

$$= \frac{\partial I}{\partial t} + (\mathbf{u} \cdot \nabla) I \quad (3.24)$$

where $\mathbf{u} = (u, v)^\top$ is the optical flow velocity and λ is a regularization parameter. Horn and Schunck (1981) derive the following 2 equations from minimizing eq.(3.21):

$$\left[\frac{\partial I}{\partial t} + (\mathbf{u} \cdot \nabla) I \right] \frac{\partial I}{\partial x} = \lambda^2 \nabla^2 u \quad (3.25)$$

$$\left[\frac{\partial I}{\partial t} + (\mathbf{u} \cdot \nabla) I \right] \frac{\partial I}{\partial y} = \lambda^2 \nabla^2 v \quad (3.26)$$

As it is not trivial how to get from eq.(3.21) to eqs.(3.25-3.26) we choose to do the full derivation.

The solution which minimizes eq.(3.21) is assumed to be $\mathbf{u}_0 = (u_0, v_0)^\top$, and to find the suitable values a small perturbation is introduced

$$\begin{aligned} u(x, y) &= u_0(x, y) + \epsilon u_1(x, y) \\ v(x, y) &= v_0(x, y) + \delta v_1(x, y) \end{aligned} \quad (3.27)$$

where ϵ and δ are arbitrary parameters and $\mathbf{u}_1 = (u_1, v_1)^\top$ are arbitrary functions. The perturbation is required to be zero at the boundaries of the domain, yielding the following boundary conditions:

$$\mathbf{u}_1(x_0, y) = \mathbf{u}_1(x_N, y) = \mathbf{u}_1(x, y_0) = \mathbf{u}_1(x, y_N) = 0 \quad (3.28)$$

Inserting eq.(3.27) into eqs.(3.22)-(3.23) and inserting this into eq.(3.21) yields

$$\begin{aligned} \Phi(\epsilon, \delta) &= \int_{y_0}^{y_N} \int_{x_0}^{x_N} \left\{ \lambda^2 \left[\left(\frac{\partial}{\partial x} (u_0 + \epsilon u_1) \right)^2 + \left(\frac{\partial}{\partial y} (u_0 + \epsilon u_1) \right)^2 + \left(\frac{\partial}{\partial x} (v_0 + \delta v_1) \right)^2 \right. \right. \\ &\quad \left. \left. + \left(\frac{\partial}{\partial y} (v_0 + \delta v_1) \right)^2 \right] + \left[(u_0 + \epsilon u_1) \frac{\partial I}{\partial x} + (v_0 + \delta v_1) \frac{\partial I}{\partial y} + \frac{\partial I}{\partial t} \right]^2 \right\} dx dy \quad (3.29) \end{aligned}$$

The minimum of Φ is found by setting the derivatives w.r.t ϵ and δ to zero. Furthermore, since the solution is assumed to be \mathbf{u}_0 , we know that this occurs when $\epsilon = \delta = 0$, i.e.:

$$\frac{\partial \Phi}{\partial \epsilon} \Big|_{\epsilon=\delta=0} = \frac{\partial \Phi}{\partial \delta} \Big|_{\epsilon=\delta=0} = 0 \quad \forall(\mathbf{u}_1) \quad (3.30)$$

First we find the derivative with respect to ϵ :

$$\begin{aligned} \frac{\partial \Phi}{\partial \epsilon} \Big|_{\epsilon=\delta=0} &= \int_{y_0}^{y_N} \int_{x_0}^{x_N} \left\{ \lambda^2 \left[2 \frac{\partial}{\partial x} (u_0 + \epsilon u_1) \frac{\partial u_1}{\partial x} + 2 \frac{\partial}{\partial y} (u_0 + \epsilon u_1) \frac{\partial u_1}{\partial y} \right] \right. \\ &\quad \left. + 2 \left[(u_0 + \epsilon u_1) \frac{\partial I}{\partial x} + (v_0 + \delta v_1) \frac{\partial I}{\partial y} + \frac{\partial I}{\partial t} \right] \frac{\partial I}{\partial x} u_1 \right\} dx dy \Big|_{\epsilon=\delta=0} \\ &= \int_{y_0}^{y_N} \int_{x_0}^{x_N} \left\{ 2 \lambda^2 \left[\frac{\partial u_0}{\partial x} \frac{\partial u_1}{\partial x} + \frac{\partial u_0}{\partial y} \frac{\partial u_1}{\partial y} \right] \right. \\ &\quad \left. + 2 \left[u_0 \frac{\partial I}{\partial x} + v_0 \frac{\partial I}{\partial y} + \frac{\partial I}{\partial t} \right] \frac{\partial I}{\partial x} u_1 \right\} dx dy = 0 \end{aligned} \quad (3.31)$$

Using the equality

$$\frac{\partial}{\partial x} \left(u_1 \frac{\partial u_0}{\partial x} \right) = \frac{\partial u_1}{\partial x} \frac{\partial u_0}{\partial x} + u_1 \frac{\partial^2 u_0}{\partial x^2} \quad (3.32)$$

leads to:

$$\begin{aligned}
\frac{\partial \Phi}{\partial \epsilon} \Big|_{\epsilon=\delta=0} &= \int_{y_0}^{y_N} \int_{x_0}^{x_N} \left\{ 2\lambda^2 \left[\frac{\partial}{\partial x} \left(u_1 \frac{\partial u_0}{\partial x} \right) - u_1 \frac{\partial^2 u_0}{\partial x^2} + \frac{\partial}{\partial y} \left(u_1 \frac{\partial u_0}{\partial y} \right) - u_1 \frac{\partial^2 u_0}{\partial y^2} \right] \right. \\
&\quad \left. + 2 \left[u_0 \frac{\partial I}{\partial x} + v_0 \frac{\partial I}{\partial y} + \frac{\partial I}{\partial t} \right] \frac{\partial I}{\partial x} u_1 \right\} dx dy \\
&= \int_{y_0}^{y_N} \int_{x_0}^{x_N} \left\{ 2\lambda^2 \left[\frac{\partial}{\partial x} \left(u_1 \frac{\partial u_0}{\partial x} \right) + \frac{\partial}{\partial y} \left(u_1 \frac{\partial u_0}{\partial y} \right) - u_1 \nabla^2 u_0 \right] \right. \\
&\quad \left. + 2 \left[u_0 \frac{\partial I}{\partial x} + v_0 \frac{\partial I}{\partial y} + \frac{\partial I}{\partial t} \right] \frac{\partial I}{\partial x} u_1 \right\} dx dy \\
&= 2\lambda^2 \int_{y_0}^{y_N} u_1 \frac{\partial u_0}{\partial x} \Big|_{x_0}^{x_N} dy + 2\lambda^2 \int_{x_0}^{x_N} u_1 \frac{\partial u_0}{\partial y} \Big|_{y_0}^{y_N} dx \\
&\quad + 2 \int_{y_0}^{y_N} \int_{x_0}^{x_N} \left\{ -\lambda^2 u_1 \nabla^2 u_0 + \left[u_0 \frac{\partial I}{\partial x} + v_0 \frac{\partial I}{\partial y} + \frac{\partial I}{\partial t} \right] \frac{\partial I}{\partial x} u_1 \right\} dx dy = 0
\end{aligned} \tag{3.33}$$

From the boundary conditions (3.28) it follows that the first two integrals on the RHS of above equation equal zero, leading to:

$$\begin{aligned}
\frac{\partial \Phi}{\partial \epsilon} \Big|_{\epsilon=\delta=0} &= 2 \int_{y_0}^{y_N} \int_{x_0}^{x_N} \left\{ \left(-\lambda^2 \nabla^2 u_0 + \left[u_0 \frac{\partial I}{\partial x} + v_0 \frac{\partial I}{\partial y} + \frac{\partial I}{\partial t} \right] \frac{\partial I}{\partial x} \right) u_1 \right\} dx dy \\
&= 0 \quad \forall u_1
\end{aligned} \tag{3.34}$$

Since this equation has to hold for all u_1 , the only way for the integral to be zero is if

$$\begin{aligned}
-\lambda^2 \nabla^2 u_0 + \left[u_0 \frac{\partial I}{\partial x} + v_0 \frac{\partial I}{\partial y} + \frac{\partial I}{\partial t} \right] \frac{\partial I}{\partial x} &= 0 \\
\rightarrow \left[\frac{\partial I}{\partial t} + (\mathbf{u}_0 \cdot \nabla) I \right] \frac{\partial I}{\partial x} &= \lambda^2 \nabla^2 u_0
\end{aligned} \tag{3.35}$$

Following a similar derivation for $\partial \Phi / \partial \delta = 0$ at $\epsilon = \delta = 0$ yields

$$\left[\frac{\partial I}{\partial t} + (\mathbf{u}_0 \cdot \nabla) I \right] \frac{\partial I}{\partial y} = \lambda^2 \nabla^2 v_0 \tag{3.36}$$

Eqs. (3.25-3.26) are two equations with two unknown, these sets of equations can thus be used to calculate the optical flow velocity components for each point in the image. Parts in the image where the brightness gradient is zero there is no information to constrain the velocity of the brightness pattern. Velocity estimates will be based on neighbouring velocity values. Velocity information is thus filled in in regions where the brightness gradient is zero (Horn & Schunck, 1981).

Chapter 4

Design implementation experimental setup

4.1 Scale model

We wish to study the flow around a beach house array where the relevant parameters under investigation are spacing, orientation and angle of attack (see section 1.2). For this purpose the scale model is designed such that these parameters can easily be adjusted. The dimensions of the scale model are limited by the dimensions of the test section of the wind tunnel, they should be considerably smaller to avoid side effects. However, they should also not be too small because it limits the range of Reynolds numbers that can be studied. This again limits the number of houses the array is composed of. The details of the scale model are described below, and choices are based on above considerations.

The holiday houses are modelled as solid blocks and the beach is modelled as a flat plate. The reason to choose for this rather simple geometric representation is that a more complex geometry will increase the number of parameters in the problem.

For the preliminary tests a single house was constructed with dimensions larger than that of the model houses in the house array, such that a larger Reynolds number flow could be studied. The model house was constructed from a pile of medium density board (MDF) slabs. The dimensions of the block where $H \times W \times D$, where $H = 120\text{mm}$, $W = 124\text{mm}$ and $D = 248\text{mm}$. The block was mounted on a 36-pointed star made of 12 mm thick plywood. The star was created with a laser cutting technique and the negative of the star was used as the surrounding plate. The 36-pointed star can be rotated with increments of 10° degrees.

The array of houses was constructed from 3 solid brass blocks, where $H = 48\text{mm}$ (effective), $W = 50\text{mm}$ and $D = 100\text{mm}$, see figure 4.1. The houses were placed on top of a 36-pointed star made of 10mm thick PMMA with a slit along the center line, see figure 4.2b. Each block contained an axis at the bottom which could move freely through the slit, and could rotate around their axis. The configuration was fixed by means of 2 mm thick metal top plates where different spacing and configurations were cut out with a laser cutting technique. Several magnets connected the top plates to the PMMA. See figure 4.2a for a schematic depiction of a top plate.

The plate was mounted within an aluminium stage tower and placed in the



Figure 4.1: Beach house array. Orientation angle is 60° degree.

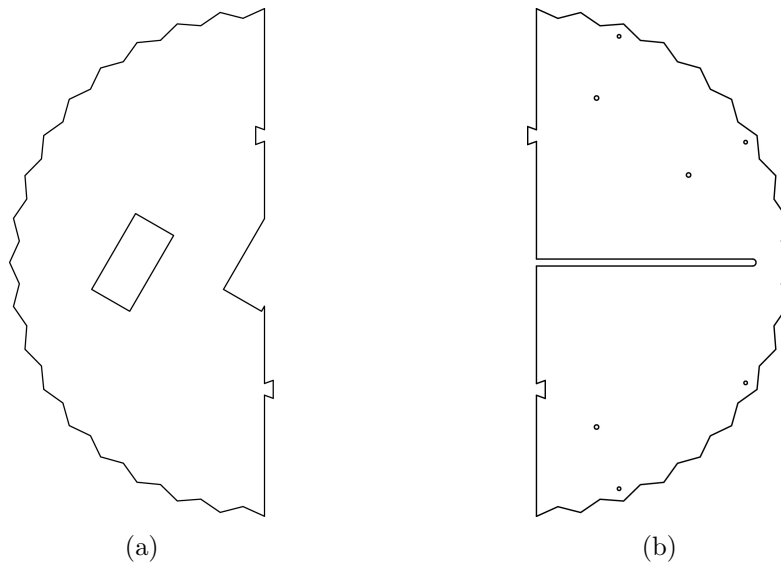


Figure 4.2: (a) Example of a top plate with orientation angle 30° degree. (b) Schematics of shape of PMMA plate with slit

open jet in front of the test section of the Silent Wind tunnel of Engineering Fluid Dynamics group (University of Twente). The dimensions of the test section are 700 mm high \times 900 mm wide. The leading edge of the plate was located at a horizontal distance of 210 mm from the test section.

Leading edge

The houses in the full scale case are submerged in a thick turbulent boundary layer. The rapid varying flow structures present in this boundary layer increase the number of parameters in the problem. Therefore we choose to study the flow with a thin laminar boundary layer. For the development of a thin laminar boundary layer on the plate it is important to consider the shape of the nose of the leading edge. A common practise in boundary layer studies is to use a nose with an elliptical shape. This shape, however, often leads to flow separation near to the junction and the formation of a separation bubble. This flow separation is caused due to a rapid increase in pressure near the junction where the curvature is not continuous but

the slope is (Narasimha & Prasad, 1994). The development of Blasius' flat plate boundary layer can be achieved by using a very thin plate, which is due to practical reasons not feasible. An other option is a very sharp leading edge, this however is prone to impairment and might be dangerous to work with. Narasimha and Prasad (1994) analysed the development of a thin laminar boundary layer on a family of super-elliptical nose shapes. The curvature at the junction of a super-ellipse and the flat plate is continuous. A super-ellipse is described by the curve

$$\left(\frac{a-x}{a}\right)^n + \left(\frac{y}{b}\right)^n = 1 \quad 0 \leq x \leq a, n > 2 \quad (4.1)$$

where a is the length of the nose and $2b$ is the thickness of the plate. If $n = 2$ it would be a normal ellipse. Narasimha and Prasad (1994) used the method of Thwaites (1949) to perform boundary layer calculations in order to determine the shapes least prone to flow separation. For details on the method of Thwaites see appendix A. They found that separation is likely to be avoided for a super-ellipse with $n = 2.5$ or $n = 3$ with a nose length of 3 times the plate thickness, i.e. $a/2b = 3$. After the analysis of Narasimha and Prasad (1994) we chose to design the shape of the nose as an super-ellipse with $n = 3$ and axis ratio $a/b = 6$. The nose is moulded out of an aluminium strip.

4.2 Hot-wire setup

For the hot-wire measurements the straight single sensor miniature probe of Dantec Dynamics (55P11) is used. The sensor is made of platinum-plated tungsten and has a diameter of approximately $5\mu\text{m}$ and a length of approximately 1.25mm . The probe is operated in CTA mode which is controlled by the StreamLine Pro system and data acquisition is performed with the StreamWare Pro software package.

For the boundary layer measurements the probe is placed normal with respect to the plate and through the plate, and can be traversed in the z -direction. For this purpose a probe support is constructed which consists of a aluminium pipe. The probe support is mounted to a manual translation stage, which can be traversed with increments of 0.01mm .

Calibration is carried out in the closed test section of the wind tunnel with a static pitot tube. The pitot tube is located at the center of the test section at a height of 180mm . The hot-wire is located at a distance of 93mm from the center line, to ensure the hot-wire is not in the wake of the pitot tube, and at a height of 180mm . Atmospheric pressure is measured with a mercury barometer, temperature is measured with the StreamLine Pro temperature probe and the perfect gas law ($p_0 = \rho RT$) is used to determine the density of the air. Velocity is calculated with Bernoulli's law from the pressure difference measured with the pitot tube.

4.3 Flow visualization setup

In this section the flow visualization setup is described. The aim is to develop a 2D image based velocimetry system. A key element is visualizing the flow, which can be done by seeding the flow with tracer particles. For this purpose a smoke generator will be used.

For image based flow velocimetry it is necessary to obtain two time correlated images of the flow. The exposure time of each recording should be sufficiently small, such that no motion blur is visible in the images. This depends on the magnification factor $M(\text{mm/px})$, free stream velocity U_∞ (m/s) and the maximum allowed displacement of a particle. The criterion described in 3.2.1 that the particle displacement should be smaller than the particle itself cannot be used because single particles will not be visible as is described below. Instead we use the criterion that the maximum allowed displacement is 2 pixels. If $U_\infty = 20\text{m/s}$ and $M = 0.1\text{mm/px}$ then the exposure time should be $10\mu\text{s}$. This is 25 times shorter than the fastest available shutter speed for consumer digital single lens reflex (DSLR) cameras. The feasibility to record images with a sufficiently high signal depends on the brightness of the light source and the light sensitivity of the camera.

An other important property in studying plane flow, that the region of interest is to be illuminated by means of a light sheet. The number of unwanted out of plane features captured depends on the thickness of the sheet, and therefore a thin sheet is required.

The development of the setup was limited by the budget and available devices. The high speed camera, available at the Engineering Fluid Dynamics group, will not be able to record useful data under the limited lighting conditions. No other high speed camera is available. High speed imaging can also be done by controlling the pulse width of the light source and triggering the camera. For this purpose a control system is necessary.

The flow visualization setup thus consists of four main elements: (i) a smoke generator, (ii) a light source, (iii) a imaging device and (iv) a control system. The four elements are described in this section, and if there was a choice between more alternatives, these are described and the choice is motivated.

4.3.1 Smoke generator

Tracer particles will be injected into the flow with the Aerolab smoke generator. The generator produces propylene glycol vapour by heating up the liquid to approximately 250° Celsius. This process results in very small particles with a diameter of 100nm, which is smaller than the wavelength λ of visible light of 400 – 700nm. The consequence is that individual particles will not be visible in images and that particles scatter in the Rayleigh regime, such that the scatter intensity scales with $1/\lambda^4$.

Correlation is accomplished by comparing image structure and intensity gradients. The density of the vapour should therefore not be too uniformly distributed, because then no changes can be identified between recording 1 and 2. This aspect needs further investigation and might lead to a modification of the smoke generator.

4.3.2 Light source

For the flow visualization experiments two different type of light sources are considered: A laser-diode (LD) module and light emitting diode (LED). Photon generation in both devices relies on a semiconductor p-n junction diode. The p-type diode contains a number of positive holes and the n-type diode contains a number of free electrons. When a current is applied the holes and electrons meet at the junction

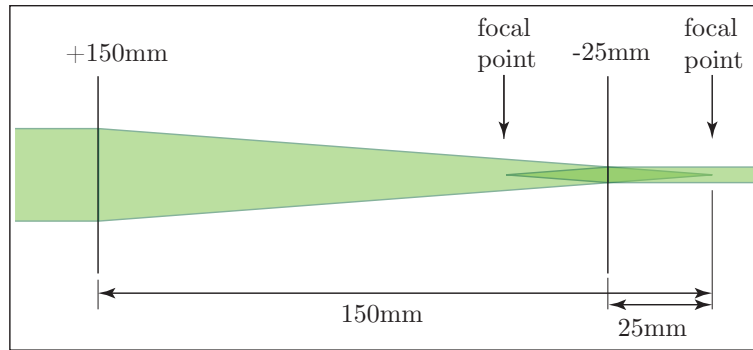


Figure 4.3: Schematics showing how a sheet thickness of the LED line light can be reduced by means of optics. Beam width is 22.6 mm (*left*) and 3.8 mm (*right*).

and recombine, and an excess of energy is released in the form of a photon. The wavelength of the emitted photon corresponds with the energy band gap of the semiconductor. This depends on the type of material used (Giancoli, 1998).

In a laser-diode an optical cavity is present at the p-n junction. The positive holes and electrons are pumped into this region. Electrons with a lower energy can absorb the energy of an incident photon and reach a higher energy state. If this electron drops to the lower energy state it releases a photon by spontaneous emission. However, if a photon strikes an electron in a higher state, it stimulates the electron to emit another photon with the same phase, direction and frequency. This is called stimulated emission. A necessary condition for this is that there should exist more electrons with a higher energy level, so that the probability emission will occur instead of adsorption is higher. Furthermore, the optical cavity acts as a resonance cavity where the population of photons increases rapidly. With a higher number of incident photons stimulated emission will occur more often than spontaneous emission (Giancoli, 1998).

Due to this process of stimulated emission a laser produces strongly coherent light. One of the consequences of this coherence is that it results in collimated light. The rays of collimated light are nearly parallel. This is in contrast to the light emitted by a LED, which diverges. As a consequence the intensity of a LED light decreases rapidly with distance.

LED line light

The in-house build LED line light, similar to the one described by Willert, Stasicki, Klinner, and Moessner (2010), was first investigated as a light source for the flow visualization experiments. The line light has a width of a few cms. This is relatively thick compared to the scale of the model houses. Therefore it was investigated whether it is possible the reduce the thickness of the line light by means of optics. Assuming a parallel beam with a width of 22.6mm (measured), it is possible to reduce the thickness of the sheet with two extra cylindrical lenses with focal distance of 150mm and ± 25 mm respectively to a thickness of 3.8mm, see figure 4.3.

However, the beam is not perfectly parallel, because the light of the line light cannot be assumed to be a point source. The optical fibres have a finite thickness, and can be better approximated as a number of point sources next to each other.

Camera	Nikon D610	Basler acA-1300-gm	
sensor type	CMOS	CCD	
sensor resolution	6016 × 4016	1296 × 966	(px × px)
sensor size	35.9 × 24	4.86 × 3.62	(mm × mm)
pixel size	5.97 × 5.97	3.75 × 3.75	($\mu\text{m} \times \mu\text{m}$)
pixel bit depth	14	12	(bit)
QE	18	57	(%)
SNR _{max}	45.5	38.4	(dB)
DR	67	57	(dB)

Table 4.1: Sensor specifications for the Nikon D610 and the Basler acA-1300-gm

For this reason not all the light rays will be deflected in a parallel fashion and this will affect the angles of the beams entering the 2nd and 3rd lenses. This will induce deflected rays in unwanted directions which will induce light loss. Furthermore, the line light is 50mm high, and the beam expands in height. Largest available cylindrical lenses were 50mm high. This means that not all the light will travel through the lenses, which means that this light is lost. The beam angle is measured to be 90° degrees, this light loss was estimated to be 70% over a distance of 150mm. The light loss due to the efficiency of LED is not included in this analysis.

Laser

Due to the collimated nature of a laser, light from a laser diode can relatively easily be transformed into a line light with line optics. The Optical Sciences group has two in-house built laser diode modules available, a blue laser with $\lambda = 450\text{nm}$ and a red laser with $\lambda = 638\text{nm}$. Only one lens per laser module is necessary to transform the beam into a line, this is achieved with the Powell Line generator from Roithner Laser Technik, resulting in a line of 1 – 2mm width and a fan angle of 30° and 15° respectively. The use of two different color light sources makes it possible to generate a double exposure recording with a RGB camera or a pair of two single exposed images with two cameras. The advantage of using red and blue light is that their wavelengths are far apart in the visible light spectrum.

Selection of light source

Because the price of line optics to generate a light sheet with a laser and the price to reduce the thickness of the LED sheet is comparable, and the high light loss which will be induced by reducing the thickness of the sheet, it is obvious to choose the laser diode as a light source.

4.3.3 Camera and optics

The basic elements of a digital camera are a lens, a light-tight box, a shutter and a sensor. The amount of light captured by a sensor depends on the aperture size, exposure time, sensitivity of the sensor and amount of available light. A large aperture allows more light entering the lens and equivalent a longer exposure time allows more photons to be captured by the sensor.

The performance of a sensor can be described by a number of parameters. A camera sensor is a chip containing a number of photodiodes equal to the resolution of the sensor. Every photodiode converts a certain amount photons into electric charge. The number of photons converted depends on the quantum efficiency (QE) of the photodiodes. Furthermore, a sensor with a larger pixel size has a larger area to capture photons and a greater volume results in a larger photon capacity. This results in a smaller image noise and a higher dynamic range (DR). The dynamic range is the range of intensity levels a sensor can capture between being completely saturated (white) and above the noise level (almost black). The dynamic range is strongly related to the pixel depth, which determines the number of intensity values the number of photons will be divided into, e.g., 2^{12} for a camera with a 12-bit processor. Finally the signal to noise ratio (SNR) the relative amount of the signal over noise. The SNR should be large enough to be able to distinguish the signal in the image from the background noise. The amount of background noise also depends on the manufacturing process of the sensor and how the camera reads out the sensor (McHugh, n.d.).

Camera selection

Two cameras in combination with the available optics are evaluated on their light sensitivity: The Nikon D610, which is available at the Engineering Fluid Dynamics group, and the Basler acA1300-30gm, which was made available by the company KITT engineering. Specifications of their sensors are listed in table 4.1. The Nikon D610 is a digital RGB single reflex (SLR) camera and the Basler acA-1300-gm is a digital monochrome camera. Both cameras have a global shutter and can be triggered externally. The Nikon camera is able to record up to 6fps and the Basler camera can record up to 30fps.

A major difference between a monochrome camera and a RGB camera is that a RGB camera has a Bayer filter in front of the sensor. This is a color filter array with a specific red green and blue color filter arrangement. Every Bayer filter contains a multiple of red filters, blue filters and two green filters. Each filter is placed in front of 1 cell of the sensor. This means that for green light only half of the light is captured and for red and blue only a quarter is captured, throwing away the rest of the light.

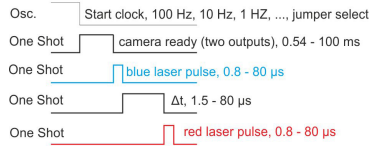
In a double exposed image, where the red laser is used for one of the exposures and the blue laser for the other exposure, the Bayer filter makes it possible to distinguish the two exposures. By identifying the Bayer filter map, one knows which pixel captured the red and blue light.

From table 4.1 it is not so obvious which camera will perform better under low lighting conditions. The Nikon camera has better specifications in terms of pixel size, bit depth, SNR_{max} and DR. The Basler camera, however has a higher QE and no Bayer filter. The value of SNR_{max} represents the highest possible signal to noise ratio, since we expect the available light to be in the lower range –thus a low signal– this value will never be reached. The same argument holds for the DR, it's important that the intensity signal in the captured data is higher than the background noise, but it's not necessary to have a large variation in intensity values.

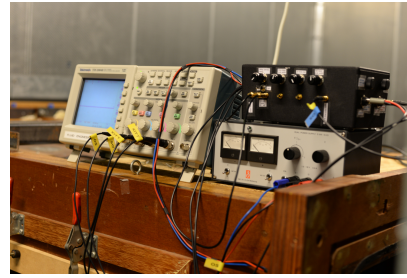
A short experiment was performed to test the light sensitivity of both cameras. The Nikon camera was equipped with a 70-210mm f/4-5.6 lens. The Basler camera



Optical Sciences



(a)



(b)

Figure 4.4: (a) Schematic representation of signals generated by the dual pulse timerbox. The times behind the signals denote the range between the pulse width can be varied. Figure made by F.B. Segerink. (b) Control system as used in the setup.

was equipped with a 50mm $f/0.9$ lens. A lens with a large focal distance for the Nikon camera was necessary to capture the field of view of interest, using this large focal distance restricts the maximum aperture size to be $f/5.6$.

It should be noted that due to the different sensor sizes lenses with the same specifications cannot be compared. An aperture of $f/5.6$ on a full frame camera corresponds with an aperture of $f/0.8$ on a camera with a $1/3''$ sensor for the same depth of field requirements (it's not clear what this implies for lighting conditions). A lens with a focal length of 200mm on a full frame sensor camera corresponds with a 28mm lens on a $1/3''$ sensor for the same angle of view requirements.

Capturing images under the same lighting conditions it was found that the Nikon camera needed approximately four times more light compared to the Basler camera. For this reason the Basler camera is selected as camera for the experiments.

Time correlated recordings

As the Basler camera is a monochrome camera, it cannot distinguish between red and blue light. Due to the scatter properties of the vapour a double exposure in one image might be tedious or impossible to correlate. The camera is not fast enough to capture a sequence of images with a short enough inter framing time. We thus need two cameras to obtain image pairs with a short inter framing time in between image 1 and image 2. With the aid of filters in front of the camera lenses, it can be achieved that one of the cameras only sees the red light and the other camera only sees the blue light.

4.3.4 Control system

A control system in the form of a timer box was designed and constructed by F.B. Segerink from the Optical Sciences group (University of Twente). It comprises a electrical circuit which generates one signal to trigger the cameras and two signals to pulse the lasers. The pulse width of the signals and the time delay in between the laser pulses can be varied. The first signal is periodic, in the form of a square wave with a frequency of 1, 10 or 100Hz. The other signals generated by the timer box are single square waves (one shot) and are triggered by the falling edge of the previous signal, see figure 4.4a for a schematics of the pulse sequence. The layout of the electrical circuit can be found in appendix B. Figure 4.6 shows the output

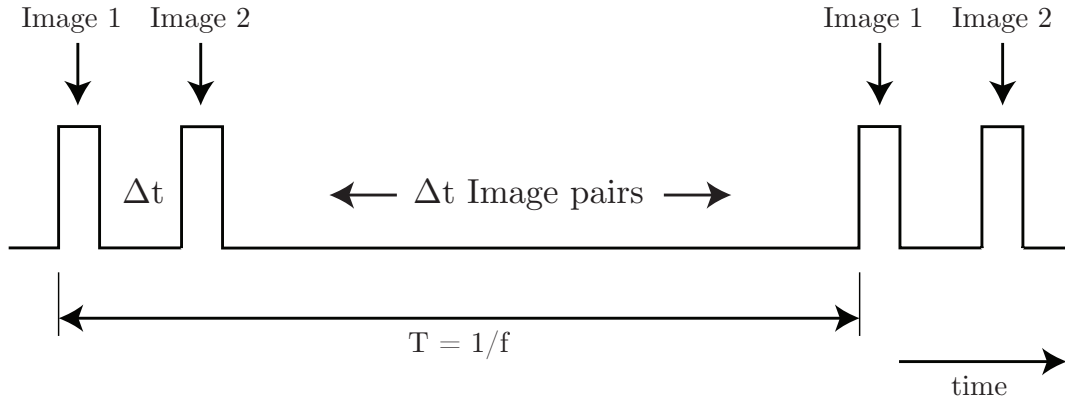


Figure 4.5: Schematic representation of illumination pulse. The inter framing time between the first and second image pair is a lot larger than the inter framing time between image 1 and image 2. T denotes the period and f denotes the frequency of the signal. Figure is not to scale.

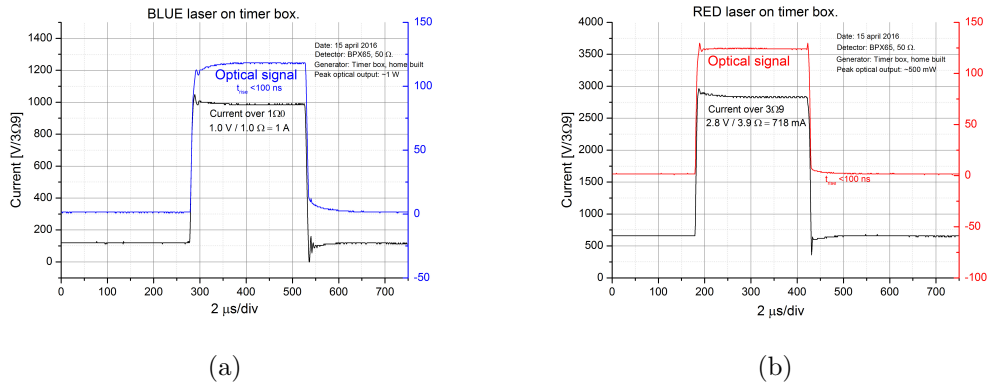


Figure 4.6: Signal of blue (left) and red (right) laser on timer box. The diagram shows that the optical signal follows the electrical signal sufficiently accurate, with $t_{rise} < 100\text{ns}$. Data and figures from F.B. Segerink.

signal of the blue and red laser on the timer box. The control system is visible in figure 4.4b.

The control system in combination with the cameras is able to capture time correlated recordings but is not able to capture time resolved recordings. This is because the cameras are not able to capture images with a high enough frame rate, such that the inter framing time between every consecutive image is sufficiently short. Figure 4.5 illustrates this.

4.3.5 Calibration procedure

The flow visualization setup obtains image pairs using 2 cameras. As it is physically impossible for the cameras to be on exactly the same place, the cameras view the scene from a different angle. This induces a perspective distorting which must be fixed using image restoration. It was also not possible to use the same optics, as they were not available, therefore both images contain distortion due to lens aberration, which is different for both images.

MATLAB features a function `estimateCameraParameters` which is able to estimate camera and lens parameters. From images taken of a checker board pattern

under different viewing angles it is possible to calculate a geometric transformation object. Transforming the images according to this transformation object curved lines in the image plane are mapped into straight lines.

A calibration unit was designed, made of a checker board pattern between two PMMA plates, which was placed prior to the experiments in the plane of interest. Images of this calibration unit, taken with both cameras, can conveniently be used to remove the perspective distortion from the images. Hereafter, the calibration images were used to obtain the same region of interest (ROI). Transformation objects obtained from the calibration images were used to apply the same transformation to the experimental images. As the square size in the checker board pattern is known also the magnification factor can be obtained from the calibration images.

4.3.6 Timing and optimization of the system

Response time cameras The cameras were triggered with the timer box. After a camera receives the trigger signal there is some delay before the camera will react. This is often referred to as the response time of the camera. See figure 4.7 for a schematic representation of the response time. Even though the documentation on the Basler cameras is very detailed, no indication on the response time of the cameras is given. This is due to the fact that too many factors (e.g., operating temperature, production spread, ageing of opto-couplers) may influence this (*User's manual for GigE Cameras*, 2015). We thus have to find this response time experimentally.

A LED was connected to the timer box and one of the cameras is connected to the trigger signal. The camera can be triggered on the rising or falling edge of the trigger signal. The response time for the rising edge is shorter compared to triggering on the falling edge. Furthermore the spreading in response time for the falling edge is larger (*User's manual for GigE Cameras*, 2015). Hence for the first experiments the camera was triggered on the rising edge of the signal. The exposure time of the camera was set much longer than the pulse width of the light source. The exposure delay, i.e. the delay between the response to the trigger and the recording, in the camera was altered until photos were captured with the LED on. A sequence of 100 photos was captured every test. This resulted in a number of images with the LED turned on, and the rest of the images with the LED turned off.

After looking into the details of the system, it turned out that the oscillator in the timer box can have a jitter, i.e. variation in the frequency of the signal, of a few percent and can be temperature dependent. On the contrary the clock in the camera has a μs accuracy. After a while the clock of both devices may get out of phase. The frequency of the oscillator was set to 10Hz. For a jitter of e.g. 5% this can result in a time difference of $\pm 2.5\text{ms}$ for half a period of 50ms. Triggering on the falling edge solved this problem. Due to a different reference point in the signal the jitter of the oscillator is less severe.

Minimizing differences between image pairs Working with 2 cameras, 2 different optics and 2 illumination sources induces differences in the image pairs. First of all, the intensity of both images was not equal. This can partly be contributed to different scatter properties due to different wave lengths of the light, the camera having a different spectral response for red and blue wavelengths, but also

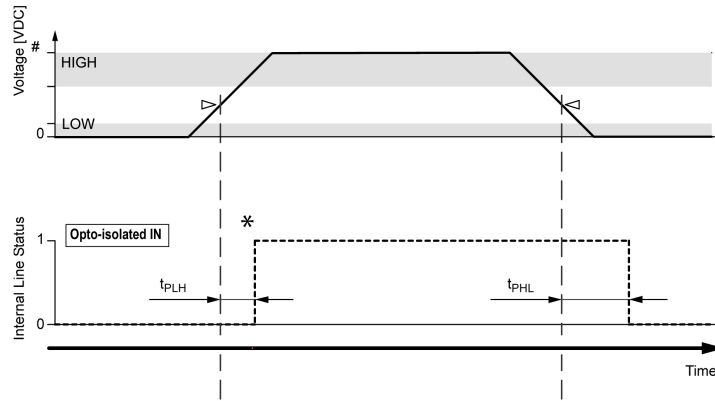


Figure 4.7: Schematics of camera response time t_{PLH} . Top panel depicts the trigger signal and the lower panel depicts the response of the camera when triggering either on the rising or falling edge. Figure adopted from *User's manual for GigE Cameras* (2015)

the optics used had different aperture stops. The aperture was adjusted such that by visual inspection the intensities in both images seemed to be similar.

Secondly, the laser diodes used are designed to produce a certain amount of light, not a perfect beam profile. As a consequence the focus of both lasers is not optimal, resulting in a different thickness of the sheet. After optimizing the focus of the lasers, experiments were performed with slits in a very thin metal sheet, made by means of a laser cutting technique. As a result a slightly improved sheet thickness was obtained.

From the response time tests it became clear that the timing of the cameras could be arranged accurately enough for the signal range used during the experiments, that it was possible to time the system with the cameras. Therefore only 1 laser was sufficient, which was still pulsed with the timer box. Cameras were triggered with the timer box and exposure time and exposure delay were controlled with the camera settings. Reducing the number of lasers also minimized the differences in the image pairs. See figure 4.8 for an example of an image pair. In this figure it is visible that still some differences are present: Image intensity is still not perfectly equal and the 1st image is sharper than the 2nd image. This blurriness was already clear while focussing the cameras. Optics used with camera 2 were difficult to focus perfectly.

Data stream problems The cameras were connected with the computer via the university network, due to the availability of power over Ethernet. The data stream which resulted from two cameras with a frequency of 10Hz was too unstable for 1 computer to handle. This resulted in images with stripes where data information was missing. This problem was fixed by using 2 computers to capture the data. For future experiments it is recommended that camera power is not supplied over the network connection but directly to the camera. The cameras can then directly be connected to one computer.

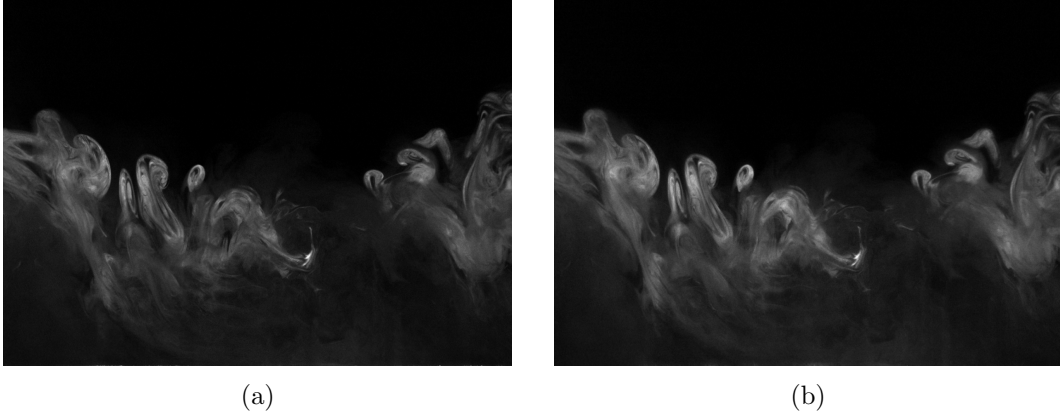


Figure 4.8: Example of image pair

4.3.7 Experiments test matrix

Various experimental runs were conducted. See table 4.2 for the different configurations and wind tunnel settings. Figure 4.9 shows the planes of interest. The free stream velocity of the wind tunnel was calculated from the differential pressure measured with the pitot static tube. The smoke was injected by means of a smoke wand, the laser sheet was used to determine its position. The oscilloscope Tektronix TDS2004B was used to view and set the signals of the timer box. Pylon viewer was used for data acquisition.

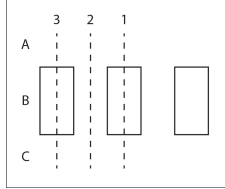


Figure 4.9: Planes of interest. Experiments conducted for planes 1A, 1B, 1C, 2A, 2C, 3A, 3B, 3C

t_{pulse} (μs)	Δt (μs)	U_{∞} (m/s)	S (mm)		
			50	100	150
50	100	3.6	0°	0°, 30°, 60°	0°
35	100	7.5	0°	0°, 30°, 60°	0°
17.5	50	18.4	0°	0°, 30°, 60°	0°

Table 4.2: Experimental test matrix. S denotes the spacing in between the houses, t_{pulse} denotes the laser pulse duration and Δt denotes the delay between the pulses. t_{pulse} and Δt are based on velocity estimates. Right cells of table contain orientation angle θ .

Chapter 5

Data analysis & results

This chapter describes the results of the measurements. Section 5.1 describes the results of a temperature correction for the HWA measurements. It was required to conduct temperature corrections, due to the relatively large temperature variations in the wind tunnel.

Incidentally a candidate PIV system was demonstrated in the wind tunnel of the EFD group and there was an opportunity to use it for a few hours for the current investigation. Therefore it was possible to study vortex structures and velocity profiles in the vicinity of a single house. The results of these measurements are presented in section 5.2.

To translate the smoke images to a velocity field, two algorithms have been evaluated. The performance of a PIV algorithm was compared to that of an OFE algorithm. To assess the effectiveness of the two algorithms, a smoke image was warped with a known displacement field and the relative error was calculated for the PIV and OFE calculation. The best performing algorithm is used to calculate a velocity field from a smoke image pair obtained from the wind tunnel experiments. This analysis is presented in section 5.3.

5.1 HWA: Validation of temperature corrections

Calibration of the hot-wire was carried out over a velocity range of 0 – 40m/s. The temperature in the wind tunnel increases when operating at higher velocities. It was found that the temperature can vary between 18 – 26° Celsius. Because the output signal of the hot-wire is sensitive to ambient temperature changes, it is necessary to perform a temperature correction. The conventional temperature correction equation proposed by Bruun (1995) is valid for temperature variations < 3° Celsius. Temperature variations in our case are higher, therefore we choose to use the method proposed by Hultmark and Smits (2010) which is valid for large temperature variations. The method of Hultmark and Smits (2010) relies on the following concept.

If the hot-wire is operating in constant temperature mode, the resistance of the wire R_w is kept constant by a feedback loop. The heating of the wire is then balanced by the convective heat transfer

$$\frac{E^2}{R_w} = h\Delta T A \quad (5.1)$$

where E (V) is the hot-wire output voltage, h (W/(m²K)) is the convective heat transfer coefficient, $\Delta T = T_w - T_a$ (K) is the difference between the hot-wire temperature and ambient fluid temperature and A (m²) is the surface area of the wire. Introducing the dimensionless number Nusselt $Nu = hd/k$, where d (m) is the diameter of the wire and k (W/(mK)) is the thermal conductivity of the fluid. For subsonic flows $Nu = Nu(Re, Pr)$, where Pr is the Prandtl number. Because the Prandtl number is only weakly dependent on temperature, it's not further included in the analysis. Substituting Nu in 5.1 yields

$$\frac{E^2}{R_w} = \frac{Nu(Re)k\Delta TA}{d} \quad (5.2)$$

which can also be written as

$$Re \equiv \frac{Ud}{\nu} = Nu^{-1} \left(\frac{E^2 d}{R_w k \Delta T A} \right) \quad (5.3)$$

where both sides of the equation are dimensionless and Re and $E^2 d / (R_w k \Delta T A)$ can be seen as a similarity variables. During the conventional calibration procedure U is found directly as a function of E , and if the ambient temperature varies the calibration procedure must be repeated to find the new relationship between U and E . Finding directly a relation between Re and $E^2 d / (R_w k \Delta T A)$ should eliminate the temperature dependence, since all temperature dependent variables (ν , ΔT and k) are included in these variables. However, finding a fit between the two similarity variables is not so trivial, because d and A are usually not precisely known. Since d and A are constants and in the constant temperature mode R_w is also constant, equation 5.3 may also be written as

$$\frac{U}{\nu} = f \left(\frac{E^2}{k \Delta T} \right) \quad (5.4)$$

where f denotes a functional dependence. Hultmark and Smits (2010) found that if calibration is done between U/ν and $E^2/(k\Delta T)$ it is possible to find the true velocity over the wire. They show that calibration curves obtained at different ambient temperatures all collapse into one if calibration is performed according above described procedure.

Above calibration method is adopted and to verify this method calibration is also done in the conventional way. Both methods are compared. U is calculated from the pressure difference measured with the pitot static tube, E and T_a are both measured. ν is calculated as follows, where the relation for μ is after Smits and Zagarola (2005)

$$\nu = \frac{\mu}{\rho} \quad (5.5)$$

$$\rho = \frac{p_0}{RT_f} \quad (5.6)$$

$$\mu = \mu_0 + \mu_1 \quad (5.7)$$

$$\mu_0 = 1.458 \cdot 10^{-6} \frac{T_f^{1.5}}{110.4 + T_f} \quad (5.8)$$

$$\mu_1 = -5.516 \cdot 10^{-8} + 1.100 \cdot 10^{-8} \rho + 5.565 \cdot 10^{-11} \rho^2 \quad (5.9)$$

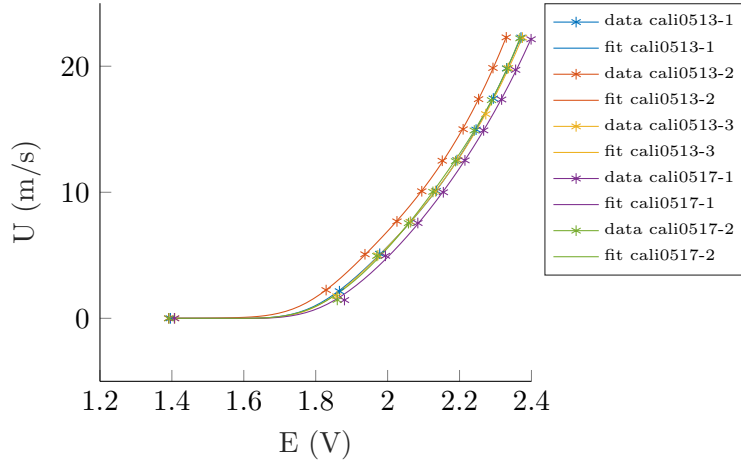


Figure 5.1: Spline fit for 5 calibration curves obtained at two different dates.

where μ is the dynamic viscosity of air, ρ is the density of air, $R = 287(\text{J}/(\text{kgK}))$ is the gas constant for dry air, $T_f = 0.5(T_w + T_a)$ is the fluid temperature. The wire temperature T_w is calculated with the following relations given by Bruun (1995)

$$R_{ref} = R_{20}(1 + \alpha_{20}(T_{ref} - T_{20})) \quad (5.10)$$

$$\alpha_{ref} = \alpha_{20} \frac{R_{20}}{R_{ref}} \quad (5.11)$$

$$T_w = \frac{0.8}{\alpha_{ref}} + T_{ref} \quad (5.12)$$

where R_{20} is the wire resistance and α_{20} is the temperature coefficient both at 20° Celcius. These values are supplied by the manufacturer. T_{ref} is the reference temperature during hardware setup, R_{ref} and α_{ref} are the corresponding resistance and temperature coefficient. Finally k is calculated using the relation given by Kannuluik and Carman (1951)

$$k = 418.4(5.75 \cdot 10^{-5}(1 + 3.17 \cdot 10^{-3}T_f - 2.1 \cdot 10^{-6}T_f^2)) \quad (5.13)$$

A spline fit is calculated using the MATLAB code written by D'Errico (2009). The reason to choose for a spline fit it that a polynomial doesn't always represent the data in a proper way, the spline fit could be done with implementing extra constraints. These constraints are that the slope of the function should be positive, and that the second derivative should be positive, which means that the curve is concave up.

Figures 5.1-5.3 show the different calibration curves. It was expected that the calibration curves of the different calibration moments in figures 5.2-5.3 would collapse into one, which is not the case. It is not understood why the calibration curves don't collapse.

In figure 5.1 is visible that the calibration curve of 0513-2 and 0517-2 are the furthest apart. This was also expected as the temperature differences between the two calibration moments was the largest. The temperature during calibration was $\sim 29^\circ$ for 0513-2 and $\sim 20^\circ$ for 0517-2.

In figures 5.2-5.3 the curves which lay furthest apart are of calibration moments 0513-2 and 0517-1. The temperature during the latter calibration moment was

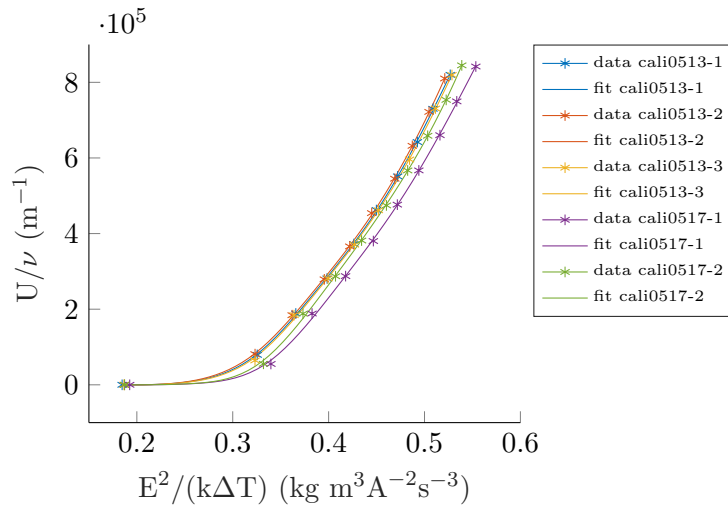


Figure 5.2: Spline fit with "similarity" variables for 5 calibration curves obtained at two different dates.

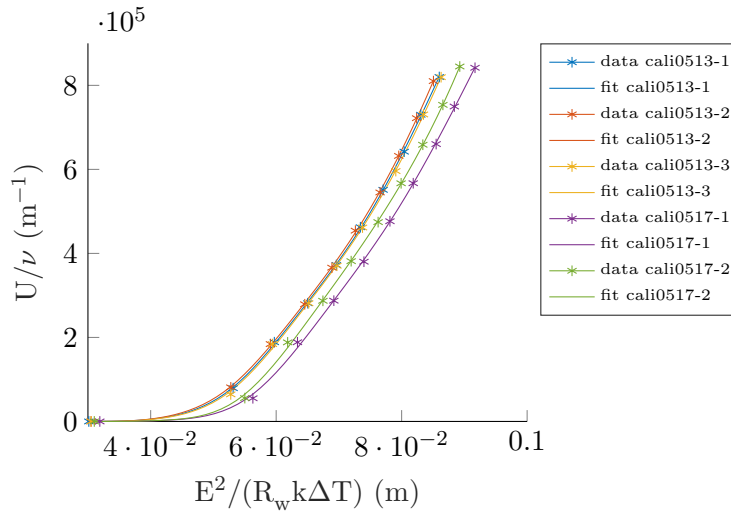


Figure 5.3: Spline fit with "similarity" variables for 5 calibration curves obtained at two different dates.

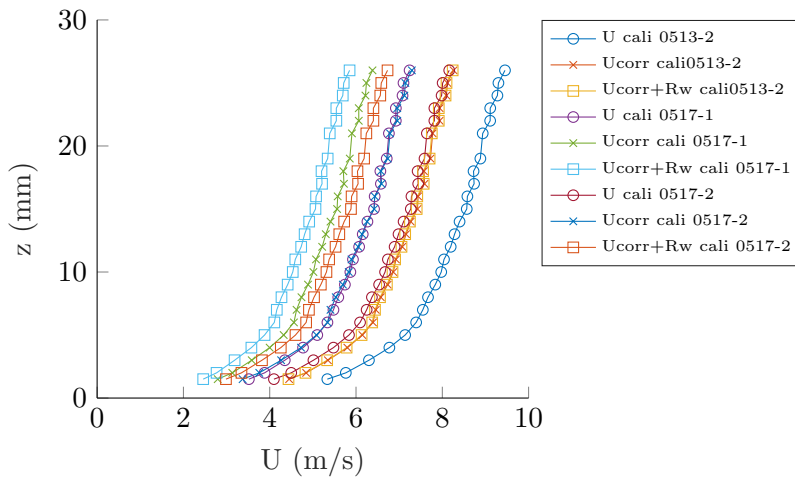


Figure 5.4: Boundary layer profiles where U is calculated from three different fits from 2 calibration dates.

$\sim 21.5^\circ$ Celsius, still a large difference compared to the temperature during 0513-2. The curves which almost seem to collapse are all from the same date (0513) where the temperatures were $\sim 23.5^\circ$, $\sim 29^\circ$ and $\sim 23.5^\circ$. However, the curves from the other calibration date (0517) don't collapse.

Figure 5.4 shows boundary layer profiles for $U_\infty = 10\text{m/s}$. The different fits were used to calculate the velocity. The values are furthest apart when U was calculated from the fit between U/ν and $E^2/R_w k \Delta T$, where the values show $\sim 51\%$ differences. The differences are $\sim 37\%$ when U was calculated from the fit between U/ν and $E^2/k \Delta T$ and $\sim 36\%$. Due to the large differences in the calibrated data hot-wire measurements were not continued.

Analysis in this section was based on including all temperature dependent parameters. The humidity of the air, however, was not included, which affects the convective heat transfer. The specific heat C_p of air depends also on its humidity. The C_p of humid air is larger than the C_p of dry air, and differences can be a few percent. The C_p appears in the Prandtl number $Pr \equiv C_p \mu / k$, and the Prandtl number was not included in this analysis because of its weak temperature dependence. It is recommended to include the Prandtl number in future analysis.

5.2 PIV

By the time of the PIV measurements only the single large house scale model was ready to use, hence this scale model was used during the experiments. The flow was seeded with Di-Ethyl-Hexyl-Sebacat (DEHS) and the particles were illuminated in a light sheet produced with a double pulse Nd:YAG laser and optics. The camera captured 15 image pairs per second. Data acquisition and processing was done with the software package Insight 4G from TSI. Setting used during processing are listed in table 5.1. Obtained velocity fields are further processed with MATLAB.

Figure 5.5 shows the time-averaged velocity fields for free stream velocities $U_\infty = 10.8\text{m/s}$, $U_\infty = 22.7\text{m/s}$ and $U_\infty = 34.6\text{m/s}$. Corresponding Reynolds number based on scale model height h are $0.9 \cdot 10^5$, $1.8 \cdot 10^5$ and $2.8 \cdot 10^5$. Streamlines are calculated with MATLAB's built in function `stream2`. From a first quick observation the topology of the velocity fields during the three different runs look comparable. The horseshoe vortex is visible upstream of the junction, although for $U_\infty = 34.6\text{m/s}$ it doesn't seem to roll up to a closed vortex (see figure 5.5f). The location of the horseshoe vortex is approximately the same for the three different velocities, see figure 5.10 for the location of the center of the horseshoe vortex for the first two velocities. In addition to this, the locations of the stagnation zone on the upstream face of the house are all around $0.6h$ for the three velocities. The agreement in location of the horseshoe vortex and stagnation point is according to expectations, because the Reynolds number range was around the same order of magnitude.

Figure 5.6 shows the normal to the plane vorticity component obtained from the average velocity fields. The vorticity was calculated using MATLAB's built in function `curl`. In all three sub figures a negative vorticity is visible close to the plate, which can be explained by the shear flow in the boundary layer. Negative vorticity peaks around the center of the horseshoe vortex. The region outside the shear layer shows very little vorticity for the runs $U_\infty = 10.8\text{m/s}$ and $U_\infty = 34.6\text{m/s}$, but a negative vorticity dominates the vorticity field for the run $U_\infty = 22.7\text{m/s}$.

Processing	Grid Engine	Recursive Nyquist Grid
	Spot Mask Engine	No Mask
	Correlation Engine	FFT Correlator
	Peak engine	Gaussian Peak
	Starting/Final Spot dimensions	64 - 32
	Maximum Displacement	$dx = dy = 0.25$
Post Processing	Local Validation	Median Test 5x5 (velocity tolerance $dU = 2$)
	Vector Conditioning Processor	5x5 Local mean and Recursive Filling
	Smoothing	Filter size 5x5, $\sigma = 0.8$

Table 5.1: Settings used in Insight 4G software for processing PIV data.

This difference between the three runs is unexpected and might be attributed to uncertainty in the measurements.

5.2.1 Upstream velocity profile

Figure 5.8 shows the approaching velocity profile of the u -component at various distances from the house. The boundary layer thickness δ_{99} is estimated, by evaluating where the velocity equals $0.99u/U_\infty$, from this figure to be $0.3h$ for $U_\infty = 10.8, 22.7$ and 34.6m/s . With the height of the scale model $h = 120\text{mm}$ this results in $\delta_{99} = 36, 48$ and 36mm , which is much thicker than expected.

The velocity profile in 5.8 corresponding to location $x = -1.61(-)$ is measured at a distance $x = 157\text{mm}$ from the leading edge. Corresponding Reynolds number at this location Re_x is

$$Re_x = \frac{U_\infty x}{\nu} \quad (5.14)$$

This yields $Re_x = 1.1 \cdot 10^5, 2.4 \cdot 10^5$ and $3.6 \cdot 10^5$ for the three different free stream velocities. According to theory, the transition from a laminar to a turbulent boundary layer occurs around $Re_x = 10^6$ (Kundu & Cohen, 2008). The boundary layers should still be in the laminar regime. Theory predicts a laminar boundary layer to have a thickness δ_{99}

$$\delta_{99} = \frac{4.93x}{\sqrt{Re_x}} \quad (5.15)$$

which yield $\delta_{99} = 2.3, 1.6$ and 1.3mm . The boundary layer thickness should thus decrease as Re_x increases for a constant x . A turbulent boundary layer should have a thickness δ_{99}

$$\delta_{99} = \frac{0.382x}{Re_x^{1/5}} \quad (5.16)$$

which yield $\delta_{99} = 5.9, 5.0$ and 4.6mm . Also the predicted values for a turbulent boundary layer are not close to the estimated δ_{99} values from our data. The question arises, if it is a boundary layer profile, or is it the velocity profile in separation bubble formed due to separation at the leading edge perhaps? This separation at the leading edge may be due to the fact that the plate was mounted on top of an aluminium beam. This beam acts as a bluff body to the flow and an adverse pressure gradient is created due to stagnating flow on this beam. This pushes against the incoming free stream velocity and might be an explanation for separation at the leading edge. See figure 5.7a for a schematic representation of the geometry of the leading edge.

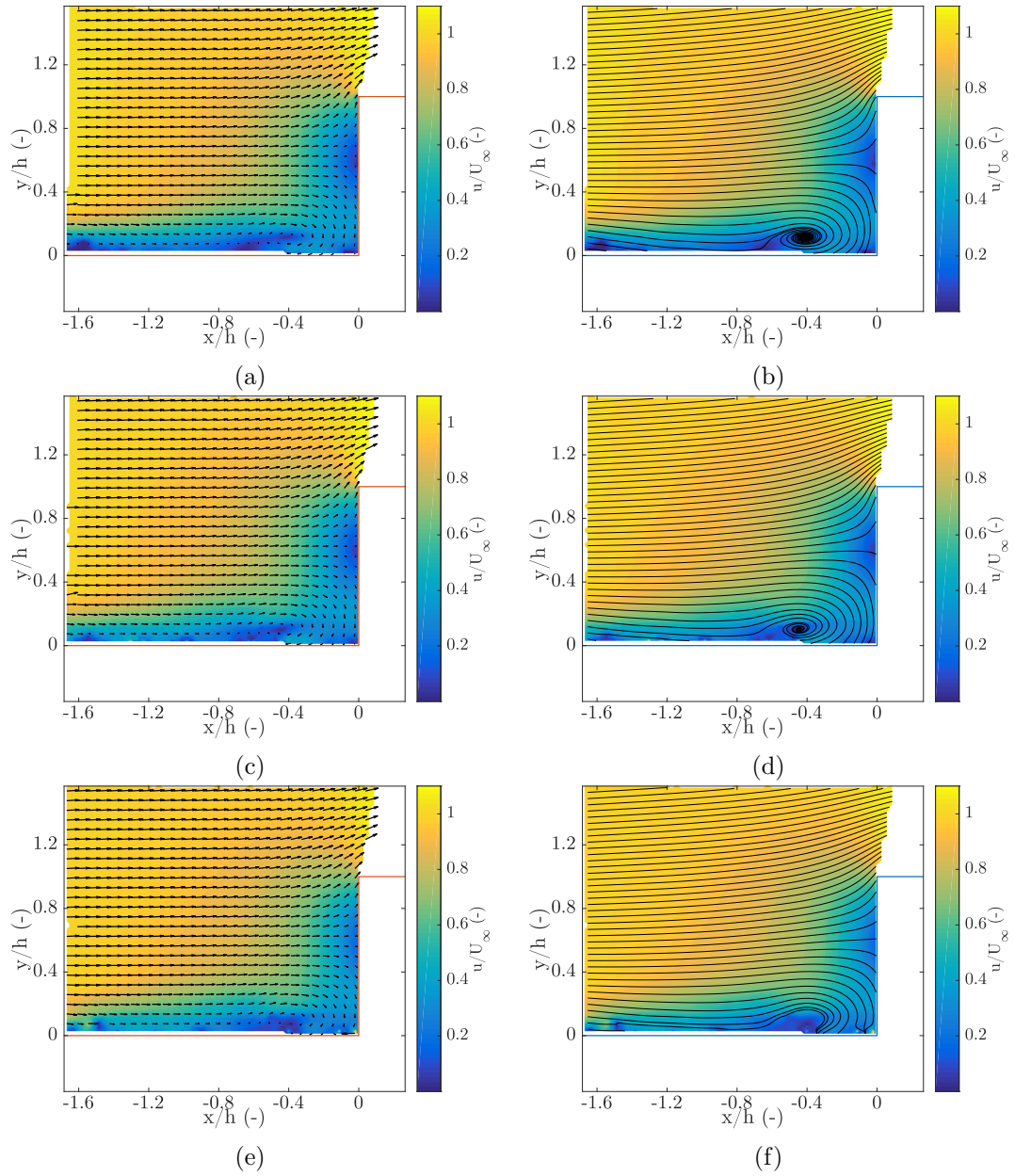


Figure 5.5: Averaged vector plots (*left*) and streamline plots (*right*) for $U = 10.8 \text{ m/s}$ (a and b), $U = 22.7 \text{ m/s}$ (c and d) and $U = 34.6 \text{ m/s}$ (e and f)

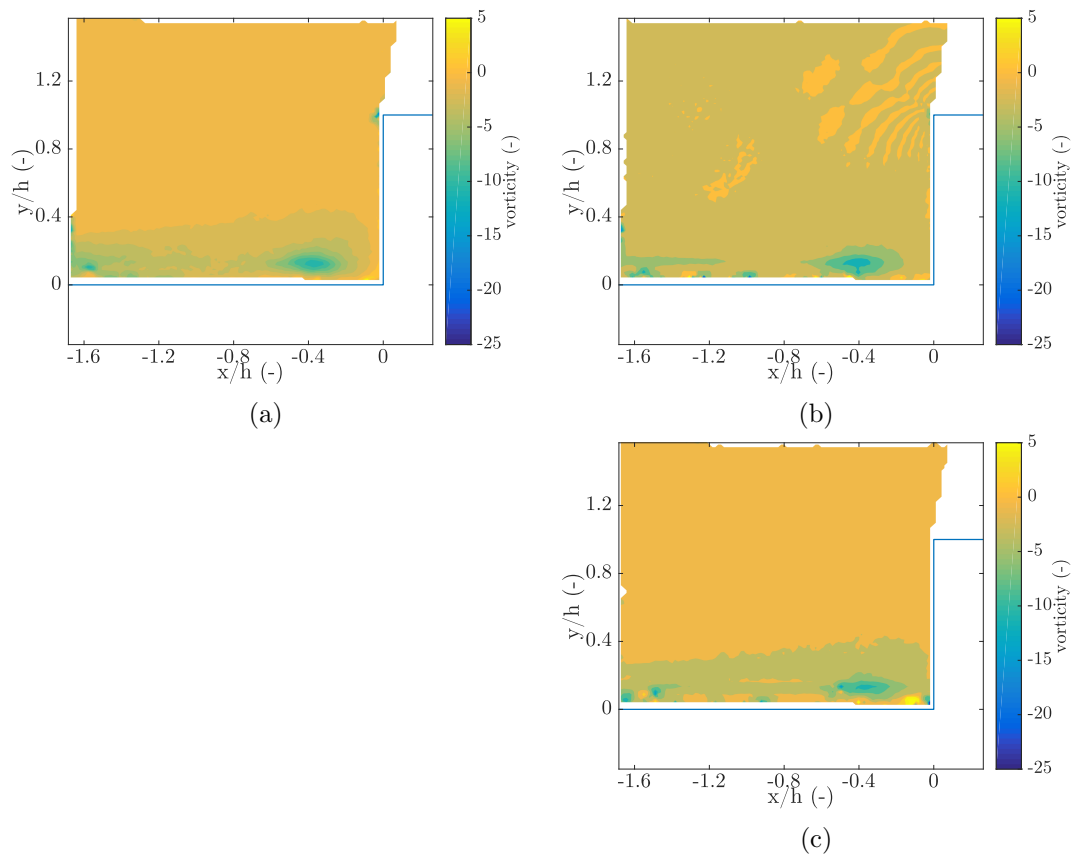


Figure 5.6: Average vorticity plots for (a) $U = 10.8\text{m/s}$,(b) $U = 22.7\text{m/s}$ and (c) $U = 34.6\text{m/s}$

After closer inspection a separation bubble, due to separation at the leading edge is indeed present. In figure 5.7b this separation at the leading edge is visible. The streamlines visible in the right column of figure 5.5 show a downward velocity for $x/h < -1$. Reattachment occurs somewhere between $x/h = -1$ and $x/h = -0.8$. This downward velocity is also visible in figure 5.10. However, a separation bubble contains a region of reverse flow, which is not visible in figure 5.8 for $x/h < -1$.

From figure 5.8 can be observed that the shape and deformation of the velocity profiles are comparable for the three different velocities. However, the region of reversed flow seems to be largest for $U_\infty = 22.7\text{m/s}$ and smallest for $U_\infty = 34.6\text{m/s}$. These differences could be due to measurement uncertainty close to the wall, which is explained below. Furthermore it is apparent that the shear on the wall $(\partial u/\partial y)_{y=0}$ decreases when the distance to the house decreases. At the location where $(\partial u/\partial y)_{y=0} = 0$ flow separation occurs. However, data points close to the wall carry a larger uncertainty. This might be attributed to the fact that correlation close to the wall might have issues due to reflections which may lead to erroneous correlation. It is therefore difficult to obtain the exact location of flow separation induced by the stagnating flow on the block.

5.2.2 Vortex detection

In order to detect the location of the vortices in the datasets a MATLAB code was written. The basic idea of the code relies on the fact that the opposite velocity components of a vortex around a point should differ in sign. A more detailed description how the code find vortex centres is given in appendix C.

Figure 5.9 shows the vortex centres found in the instantaneous velocity fields. First it should be noted that not in every instantaneous velocity field vortex centres were found, furthermore in a number of instantaneous velocity fields more than one vortex center was found. Apparent in this figure is that most vortices concentrate in comparable areas: $x = [-0.6, -0.2]$ and $y = [0.05, 0.2]$.

Striking and somewhat counter intuitive is that for increasing velocities a decreasing number of vortex centres were detected in a decreasing number of instantaneous velocity fields. Furthermore, no vortex center was detected in the average velocity field for $U_\infty = 34.6\text{m/s}$. This result agrees well with the fact that no closed vortex is

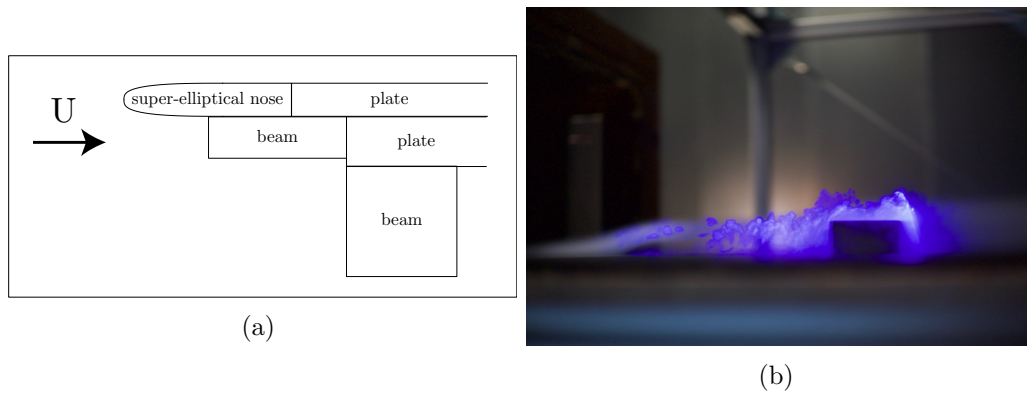
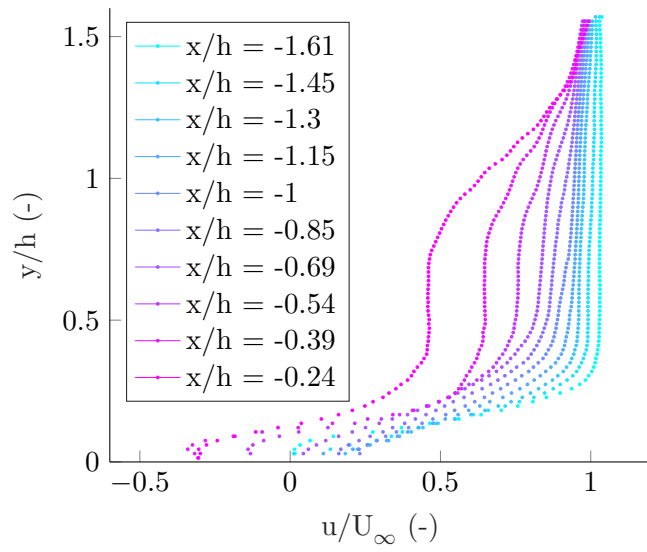
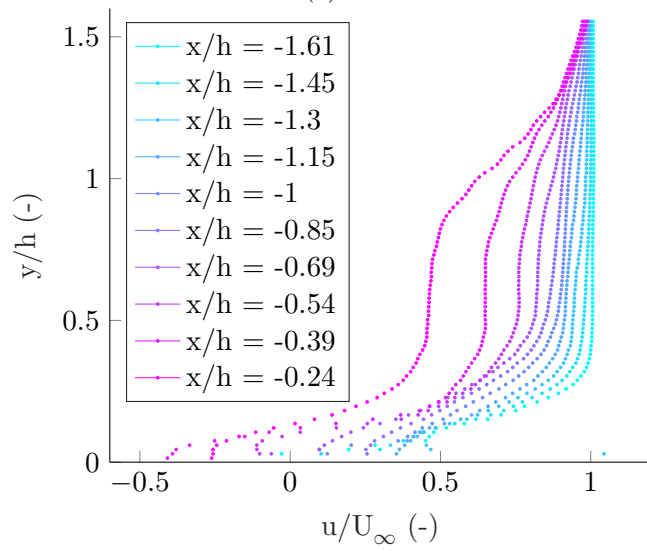


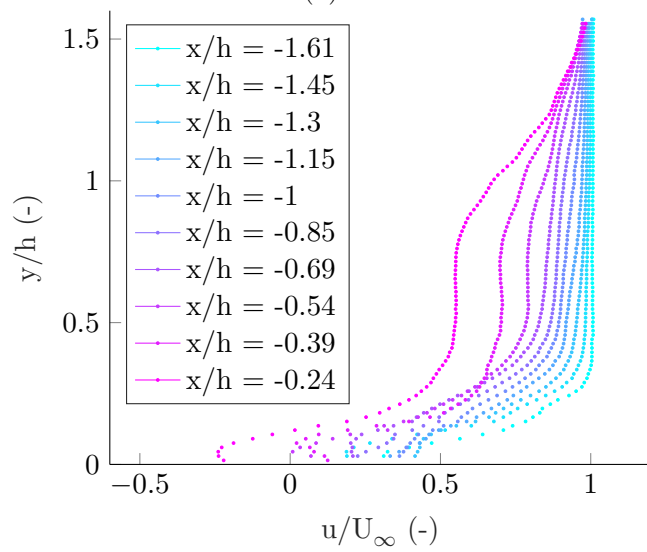
Figure 5.7: (a) Schematic representation of super-elliptical nose with beam below. (b) Photo showing separation at leading edge. Photo by P. Jonkman.



(a)



(b)



(c)

Figure 5.8: Approaching velocity profile of u -component at various distances from the block for (a) $U = 10.8 \text{ m/s}$, (b) $U = 22.7 \text{ m/s}$ and (c) $U = 34.6 \text{ m/s}$

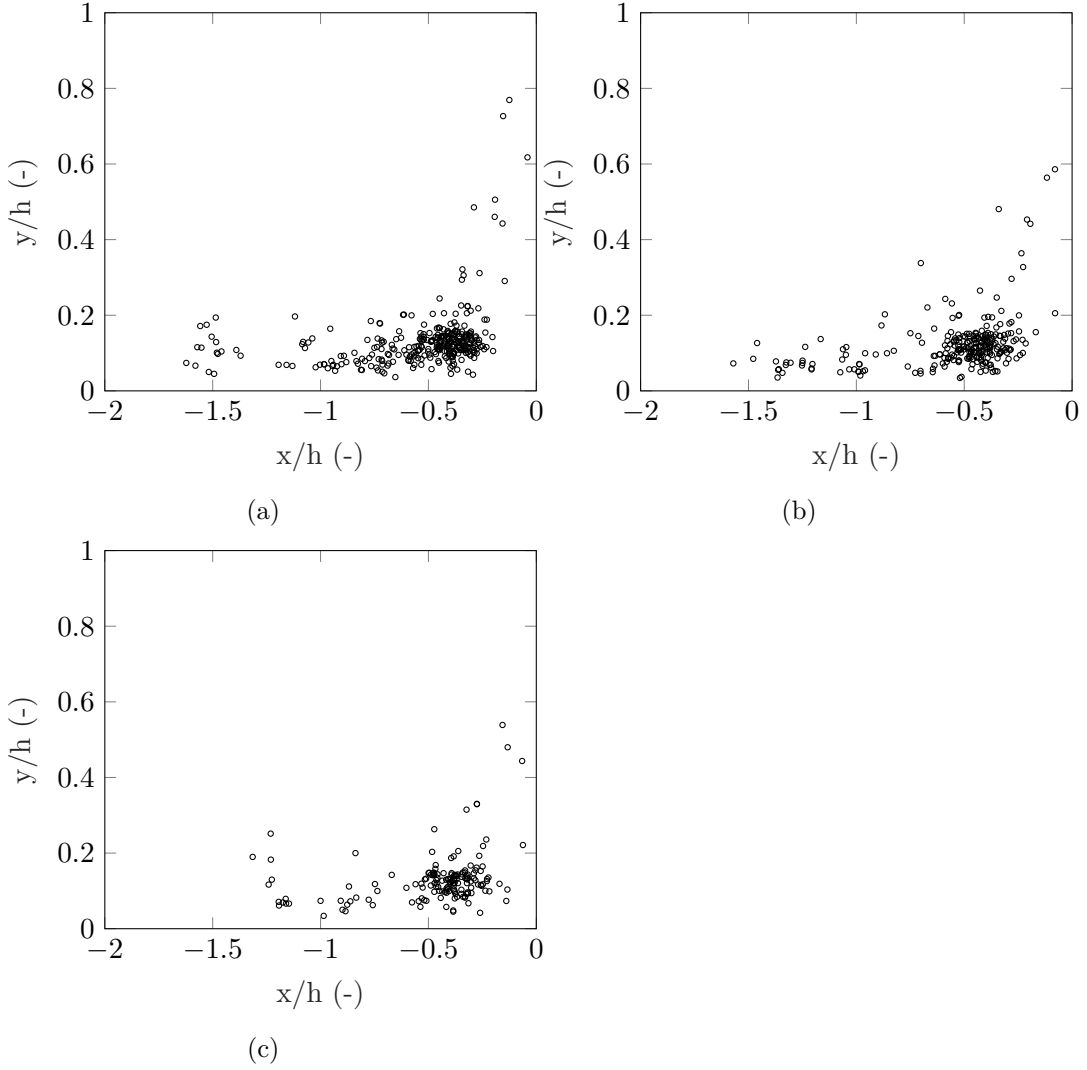


Figure 5.9: Vortex center locations found from instantaneous velocity fields. The algorithm searched 500 velocity fields per velocity. (a) $U = 10.8\text{m/s}$ where 323 vortex centers were detected in 256 instantaneous velocity fields. (b) $U = 22.7\text{m/s}$ where 256 vortex centers were detected in 222 instantaneous velocity fields. (c) $U = 34.6\text{m/s}$ where 161 vortex centers were detected in 147 instantaneous velocity fields.

observed in figure 5.5f. However, the underlying mechanism is not yet understood. Perhaps the flow structures get more irregular at higher velocities and therefore less perfectly closed vortices are observed. The PIV data is not time resolved, only 15 image pairs per second are obtained. The time scale of the velocity fluctuations might be shorter for the higher velocities, and maybe less vortices are recorded which doesn't mean that less vortices were present.

5.2.3 Vortex velocity profile

Figure 5.10 shows the velocity profile of the v -component of the vortices found for $U = 10.8$ and $U = 22.7\text{m/s}$. Velocity profile is plotted for constant y . The choice for showing the v -component, is that main flow is in x -direction and u -component will have a main flow part. Real vortices may often be approximated as a combination

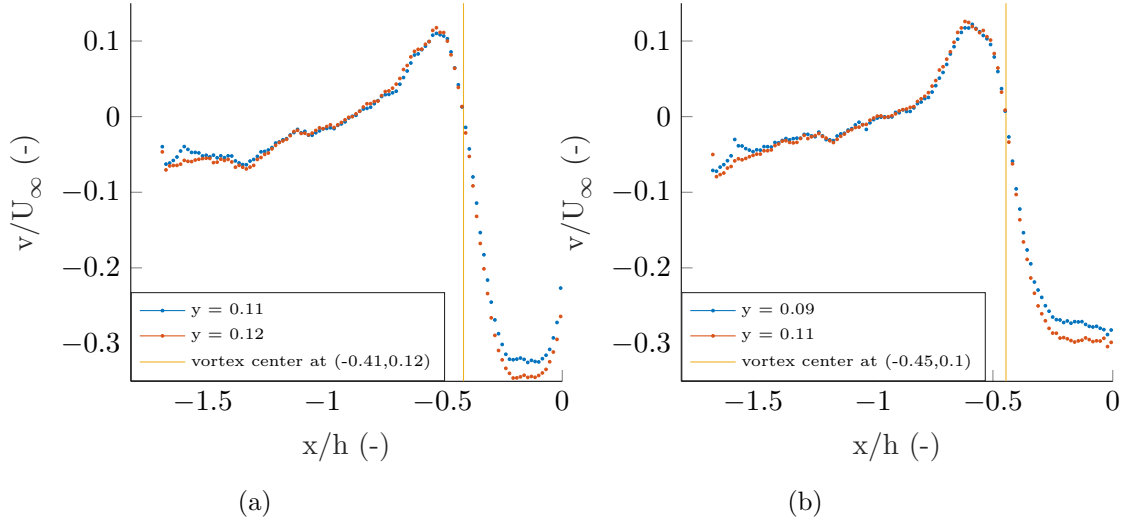


Figure 5.10: Velocity profile through vortex center of v -component for (a) $U = 10.8\text{m/s}$ and (b) $U = 22.7\text{m/s}$

of idealized vortices. A common idealization is the Gaussian vortex, composed of a viscous core containing nearly solid body rotation and the region outside the core being nearly irrotational (Kundu & Cohen, 2008). This vortex has no radial velocity ($u_r = 0$), the azimuthal velocity component is described by

$$u_\theta(r) = \frac{\Gamma}{2\pi r} \left(1 - \exp(-r^2/R^2)\right) \quad (5.17)$$

where R is a core-size parameter. At first sight it seems that the velocity profile looks like a Gaussian vortex velocity profile. To verify this a fit is calculated in the form of

$$v_{\text{vortex}} = \frac{a}{x} \left(1 - \exp(-x^2/R^2)\right). \quad (5.18)$$

For convenience the data was shifted such that the center of the vortex is located at $x/h = 0$. Figure 5.11 shows the calculated fits for $U_\infty = 10.8\text{m/s}$ and $U_\infty = 22.7\text{m/s}$. Coefficients found for $U_\infty = 10.8\text{m/s}$ are $a = -0.014$ and $R = 0.083$ and coefficients for $U_\infty = 22.7\text{m/s}$ are $a = -0.018$ and $R = 0.097$. From figure 5.11 it is clear that the measured data doesn't obey the relation which describes a Gaussian Vortex. However, the separation bubble, due to separation at the leading edge, and the flow reattachment is not included in this Gaussian vortex model. This presumably influences the velocity profile of the vortex observed.

5.3 Smoke visualization

In this section the performance of both a PIV and optical flow algorithm is investigated. This is done by deforming an image from the obtained data with known velocity fields and calculating the error between the exact and calculated velocity field. Hereafter the best performing algorithm is tested on the obtained data from the wind tunnel experiments.

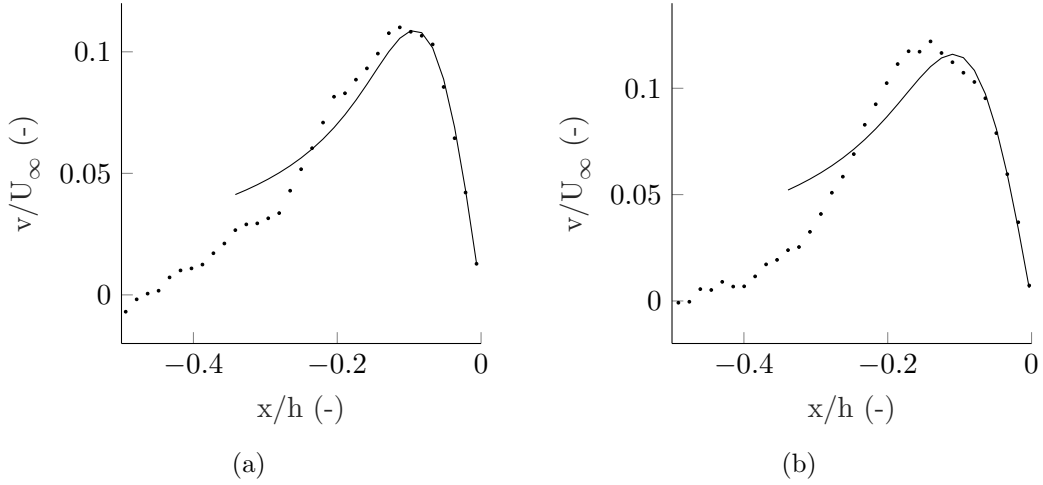


Figure 5.11: Calculated Gaussian vortex fit for the v -component velocity profile for (a) $U_\infty = 10.8\text{m/s}$ and (b) $U_\infty = 22.7\text{m/s}$. Data plotted for constant y and shifted such that vortex center is located at $x/h = 0$.

5.3.1 Image deformation

In order to save computation time a smaller portion ($388 \times 374\text{px}^2$) of an image of the captured data is used. The image the analysis is performed on is shown in figure 5.12. Two types of flow were studied.

A stagnation flow which is described by

$$u = 2Ax \quad (5.19)$$

$$v = -2Ay \quad (5.20)$$

where 3 values for A were chosen, namely $A = 1, 5$ and 10 . The PIV analysis was only performed for $A = 1$, the optical flow analysis is further extended with $A = 5$ and 10 . The other flow studied is described as a block moving with uniform velocity, we will refer to this flow as block flow from now on. This flow is described as

$$u = \begin{cases} 10 & \text{for } a < x < b, \ c < y < d \\ 0 & \text{otherwise} \end{cases} \quad (5.21)$$

$$v = \begin{cases} 5 & \text{for } a < x < b, \ c < y < d \\ 0 & \text{otherwise} \end{cases} \quad (5.22)$$

where x is the pixel location in the horizontal direction and y is the pixel location in the vertical direction. Values for a, b, c and d were chosen to be 150, 200, 100 and 300 respectively. The reason to choose for this block flow is that the smoothness assumption of the OFE algorithm doesn't hold at the edges of the block. Hence it is of interest how this algorithm deals with this block flow.

The flows described above were used to calculate the displacement field on a grid with equal size as the resolution of the image in figure 5.12. This image is transformed according to the calculated displacement field using MATLAB's built in function `imwarp`. The warped images with their corresponding displacement field are shown in figure 5.13.

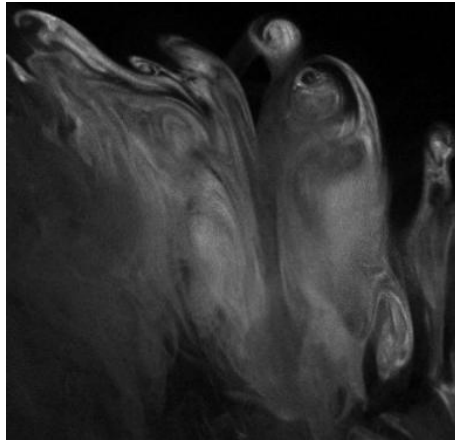


Figure 5.12: Small portion of original smoke image.

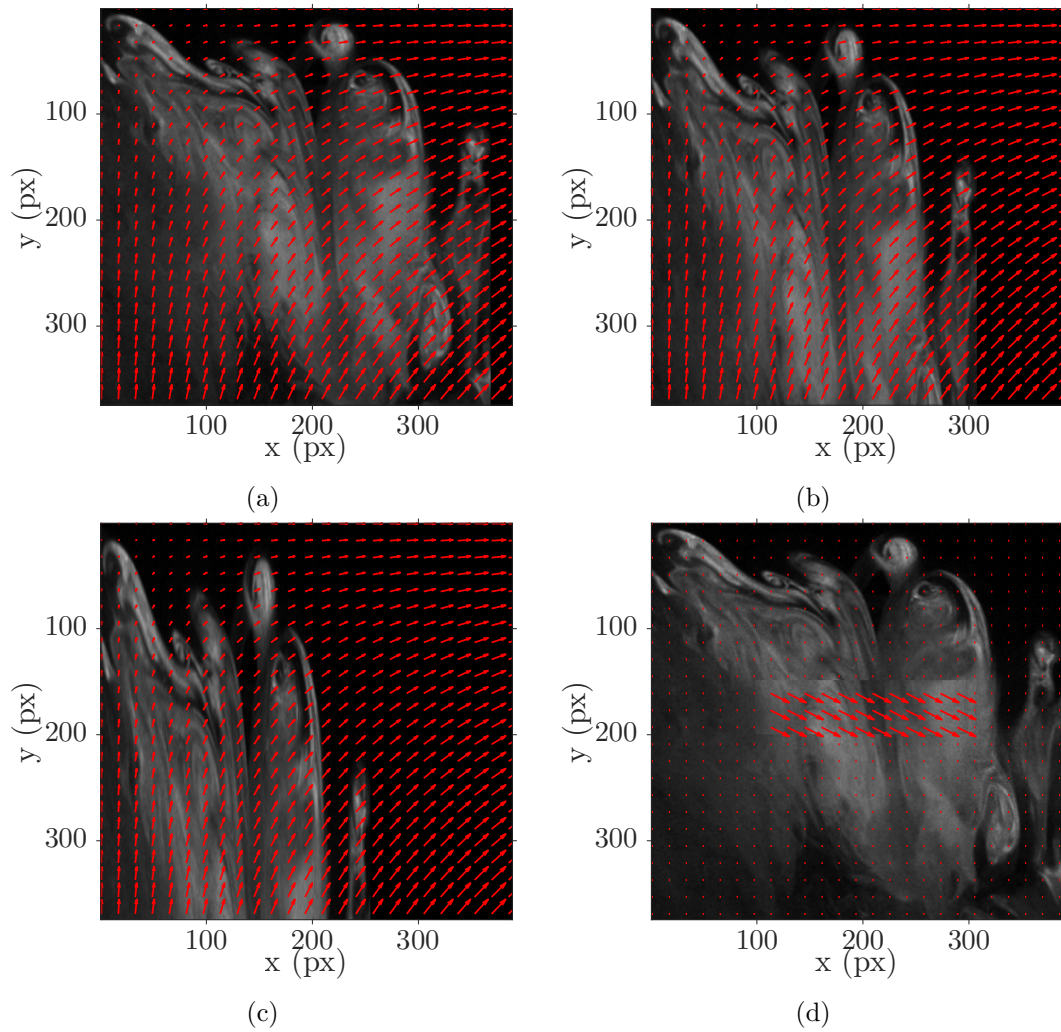


Figure 5.13: Warped image with corresponding displacement fields. Stagnation flow with $A = 1, 5$ and 10 in figures (a)-(c) and block flow in figure (d).

5.3.2 PIV algorithm analysis

Correlation method

For the PIV analysis the open source PIVlab code from Thielicke and Stamhuis (2014a) was used. The program features two correlation methods, FFT based correlation and direct cross correlation (DCC). The direct cross correlation computes the correlation in a spatial domain, whereas the FFT based correlation computes the correlation in the frequency domain. Both correlation methods were used for current analysis.

For the DCC approach the window sizes may have different sizes. If the interrogation area of image 2 is twice as large as image 1, a particle displacement up to half the size of the interrogation area in image 1 will not result in loss in information. No particles will have moved out of the interrogation area in image 2 (Thielicke & Stamhuis, 2014b). As this will provide more reliable results the interrogation area of image 2 is chosen to be twice as large as the interrogation area of image 1.

For the FFT based correlation approach interrogation areas must have the same size. The code, however, provides a multi pass calculation. Here first the correlation is calculated for a larger area, the displacement information is used to deform and displace the 2nd smaller interrogation area, see figure 3.5 for a schematic depiction of this deformation (Thielicke & Stamhuis, 2014b).

Interrogation area size for present analysis is based on the maximum displacement. This is 10.2px for the block flow, here a window size of 16px is chosen. And 28.3px for the stagnation flow, here the smallest window size of 32px is chosen.

According to Thielicke and Stamhuis (2014b) and references therein, the DCC approach generally results in more accurate results, but computation time is more expensive. However Thielicke and Stamhuis (2014b) show with quality tests that the FFT approach with the window deformation technique out performs the traditional DCC approach. Both correlation methods were used for current analysis.

Pre-processing

Image pre-processing generally improves the quality of the analysis, as the data can have a low signal to noise ratio. Even though no noise should be present in images used for present analysis, as image 1 is a warped version of image 2, the intensity gradients in parts of the image are small. For this reason the images were pre-processed using contrast limited adaptive histogram equalization (CLAHE). CLAHE operates on small regions in the image, spreading the most frequent intensities of the image histogram over the full intensity range (Thielicke & Stamhuis, 2014b). As a result, low contrast regions obtain a higher contrast, and therefore the pre-processed image will contain more details. A CLAHE window size of $10 \times 10\text{px}^2$ is used. Pre-processing might induce artefacts in the image, therefore the results were CLAHE was used are compared with runs where no pre-processing is used.

Post-processing

It is generally agreed that post-processing is necessary to obtain reliable results of a PIV analysis (Thielicke & Stamhuis, 2014b). Since the exact flow field is known it's convenient to set limits to acceptable displacement distances. The velocity limits

pre-processing	correlation	window size (px ²)	RMS (-)	mean error (%)
CLAHE	DCC	64 ² → 32 ²	9.02 · 10⁻²	6.7
CLAHE	FFT	64 ² → 32 ² ; 32 ² → 16 ²	2.45 · 10 ⁻¹	15.1
CLAHE	FFT	128 ² → 64 ² ; 64 ² → 32 ²	2.85 · 10 ⁻¹	17.6
–	DCC	64 ² → 32 ²	1.55 · 10 ⁻¹	11.4
–	FFT	64 ² → 32 ² ; 32 ² → 16 ²	5.06 · 10 ⁻¹	39.2
–	FFT	128 ² → 64 ² ; 64 ² → 32 ²	7.37 · 10 ⁻¹	53.1

Table 5.2: PIVlab stagnation flow $A = 1$

were set within the range of the minimum and maximum displacement of the imposed flow.

Results

In order to evaluate the performance of the PIV analysis a mean error (%) and a root mean square (RMS) of the error is calculated. The RMS error and mean error were calculated as follows

$$RMS = \sqrt{\frac{1}{N} \sum_i \sum_j e_{ij}^2} \quad (5.23)$$

$$e_{\text{mean}} = \frac{1}{N} \sum_i \sum_j e_{ij} \quad (5.24)$$

$$\text{with } e_{ij} = \frac{|\mathbf{u}_{\text{calc},ij} - \mathbf{u}_{\text{ex},ij}|}{|\mathbf{u}_{\text{ex},ij}|} \quad (5.25)$$

where N is the number of data points, i and j refer to row and column index of the data set, e_{ij} is the error at every point, $\mathbf{u}_{\text{ex},ij}$ is the exact velocity vector and $\mathbf{u}_{\text{calc},ij}$ is the calculated velocity vector. The results are summarized in tables (5.2-5.3). From this table it is obvious that using CLAHE for pre-processing results in a smaller error and that DCC outperforms FFT based correlation. The best performing settings for the stagnation flow results in an average error of 6.7% which is not small. However, the best performing settings for the block flow results in an average error of 30.4%, which is unacceptably large. The calculated vector fields with smallest error are shown in figure 5.14, where it is apparent that the stagnation flow agrees reasonably with the exact flow, but the block flow shows large deviations from the exact flow. Furthermore vectors are also found in regions where the displacement should equal 0.

5.3.3 OFE algorithm analysis

The optical flow code by Sun (2010) was used for present analysis. Their code features several optical flow methods, but they also implemented the classical Horn and Schunck (1981) method (Sun, Roth, & Black, 2014). Performance of this method is tested on the warped images. The smoothness assumption is not everywhere valid for the block flow, as the flow field contains discontinuities at the edges of the block. The smoothness assumption becomes less important during computation if the regularization parameter λ is small. For this reason the calculation was performed for

pre-processing	correlation	window size (px ²)	RMS (-)	mean error (%)
CLAHE	DCC	64 ² → 32 ²	6.77 · 10 ⁻¹	60.3
CLAHE	DCC	32 ² → 16 ²	3.68 · 10⁻¹	30.4
CLAHE	FFT	64 ² → 32 ² ; 32 ² → 16 ²	4.71 · 10 ⁻¹	39.7
CLAHE	FFT	128 ² → 64 ² ; 64 ² → 32 ²	4.68 · 10 ⁻¹	31.3
–	DCC	64 ² → 32 ²	6.43 · 10 ⁻¹	62.3
–	DCC	32 ² → 16 ²	7.12 · 10 ⁻¹	68.2
–	FFT	64 ² → 32 ² ; 32 ² → 16 ²	6.67 · 10 ⁻¹	61.6
–	FFT	128 ² → 64 ² ; 64 ² → 32 ²	7.37 · 10 ⁻¹	70.5

Table 5.3: PIVlab block flow

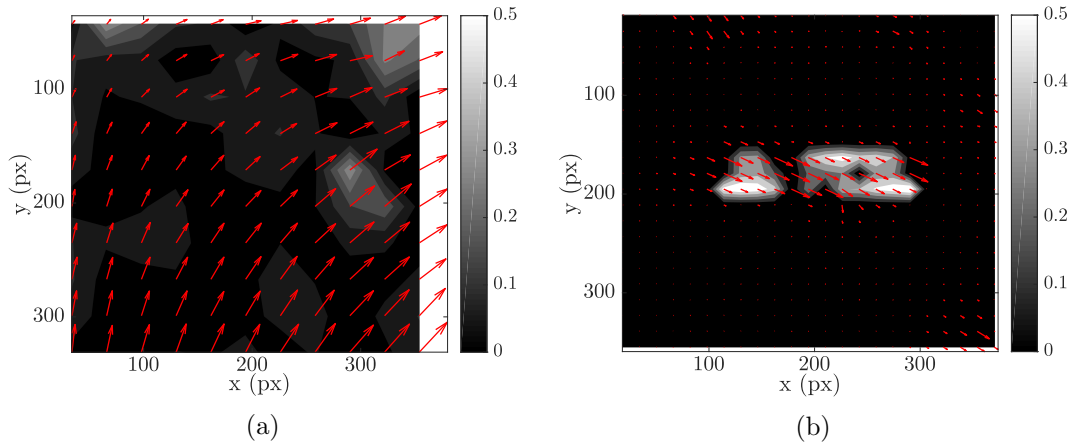


Figure 5.14: Calculated flows with PIVlab with the smallest error. (a) Stagnation flow, 10×11 vectors, average error 6.7%, root mean square of error $9.02 \cdot 10^{-2}$. (b) Block flow, 22×23 vectors, average error 30.4%, root mean square of error $3.68 \cdot 10^{-1}$

type of flow	λ (-)	RMS (-)	mean error (%)
block flow	1	$2.66 \cdot 10^{-2}$	5.6
stagnation flow ($A = 1$)	129	$1.61 \cdot 10^{-2}$	0.9
stagnation flow ($A = 5$)	27.8	$9.82 \cdot 10^{-2}$	4.6
stagnation flow ($A = 10$)	27.8	$6.27 \cdot 10^{-1}$	55.5

Table 5.4: Smallest average error and RMS error for the calculated flows with the OFE algorithm.

various λ to identify the best performing λ . The analysis for the stagnation flow was further extended with $A = 5$ and $A = 10$, as it is of interest to investigate how the code deals with larger displacement. Also the black edge in the warped images (see figure 5.13(a)-(c)) contain no information on the displacement and it is of interest how the code handles this features.

Computation was done with $\lambda \in [10^{-2}, 10^5]$ in 8 steps. The mean error and RMS are calculated with eqs. 5.23-5.25, as described in previous section. Figure 5.15a shows the RMS for the block flow. In this figure is visible that as λ increases the error increases, which is expected because the block flow contains discontinuities in the flow and therefore the smoothness assumption should be less important. This corresponds to a smaller λ . Figures 5.15b-5.15d show the RMS error for the stagnation flows. In figures 5.15b-5.15c a well defined minimum is visible, whereas for figure 5.15d the RMS error has the same order of magnitude. This indicates that the OFE algorithm has difficulties with the stagnation flow where $A = 10$.

After this a finer calculation was done to identify the best λ more accurate (not shown). The calculated flows with the smallest error are presented in figure 5.16. Table 5.4 shows the average and RMS error for these flows. From figure 5.16 it is apparent that the code has problems calculating the flow field for the stagnation flow with $A = 10$, with an average error of 55.5%. In general may be said that for the stagnation flows, the larger the displacement the larger the error.

The resolution of the vector field equals the resolution of the images, i.e., 388×374 vectors, which is very high compared to what a PIV algorithm can achieve. The average error for the block flow is 5.6%, which is not low. However compared to the result of the PIV calculation this seems very reasonable. Furthermore the average error of the stagnation flow with $A = 1$ is 0.9%, which is very acceptable, and more accurate compared to the PIV calculation. In sub figure (c) it is visible the error gets larger near the area where no flow information is present, the black edge described earlier.

5.3.4 Results on smoke image pair

Previous sections show that the optical flow calculation resulted in higher resolution vector fields and smaller errors. Therefore the analysis on a smoke image pair was continued with the optical flow code.

The calibration images were used to remove camera and perspective distortion, and to identify the same field of view. See figure 5.17 for the image pair used in current analysis. The images were fused in such a way that image 1 and image 2 have different color bands. In this way the movement is visible in a static image.

The flow is from right to left, which is clearly visible in the image pair. However, after closer inspection, when viewing the images short after each other on a screen,

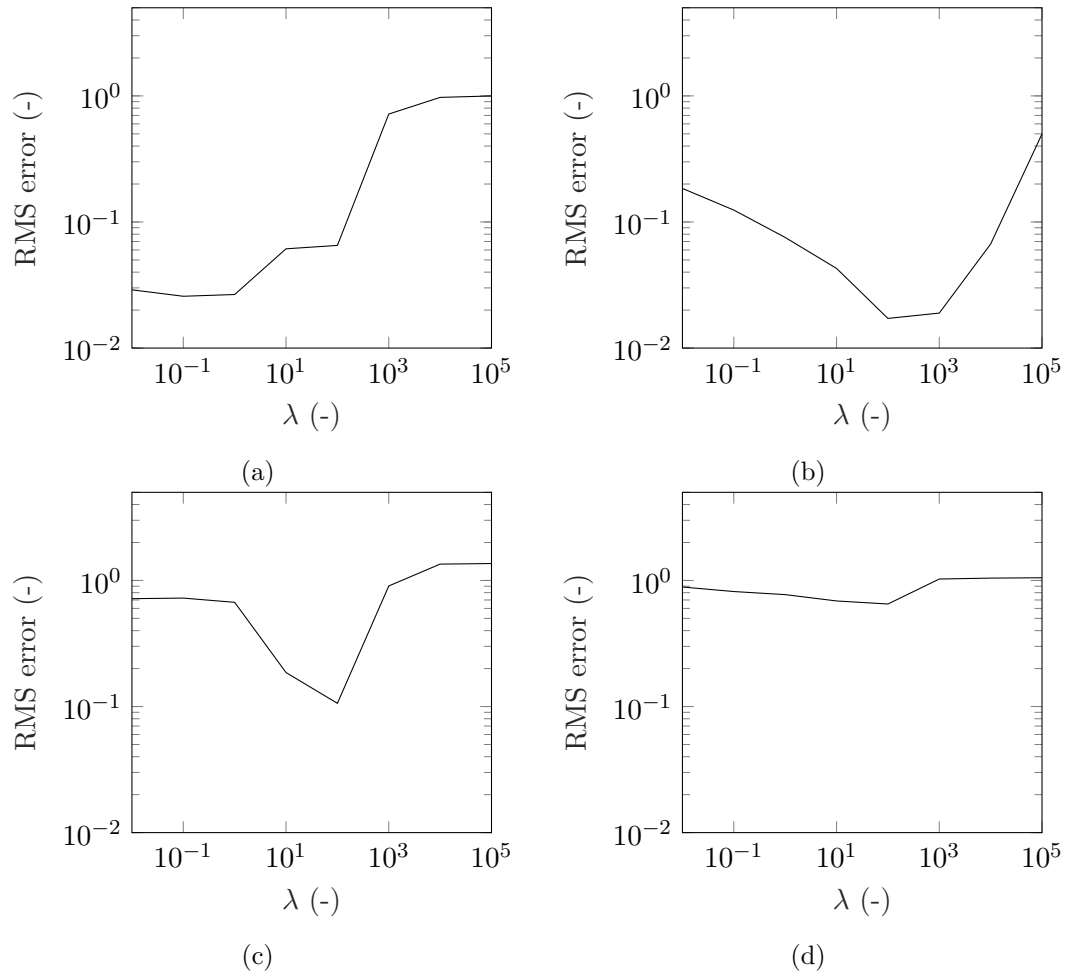


Figure 5.15: Root mean square of error for various values of λ for the flows: Block moving with uniform velocity (a), stagnation flow with $A = 1$ (b), stagnation flow with $A = 5$ (c), stagnation flow with $A = 10$.

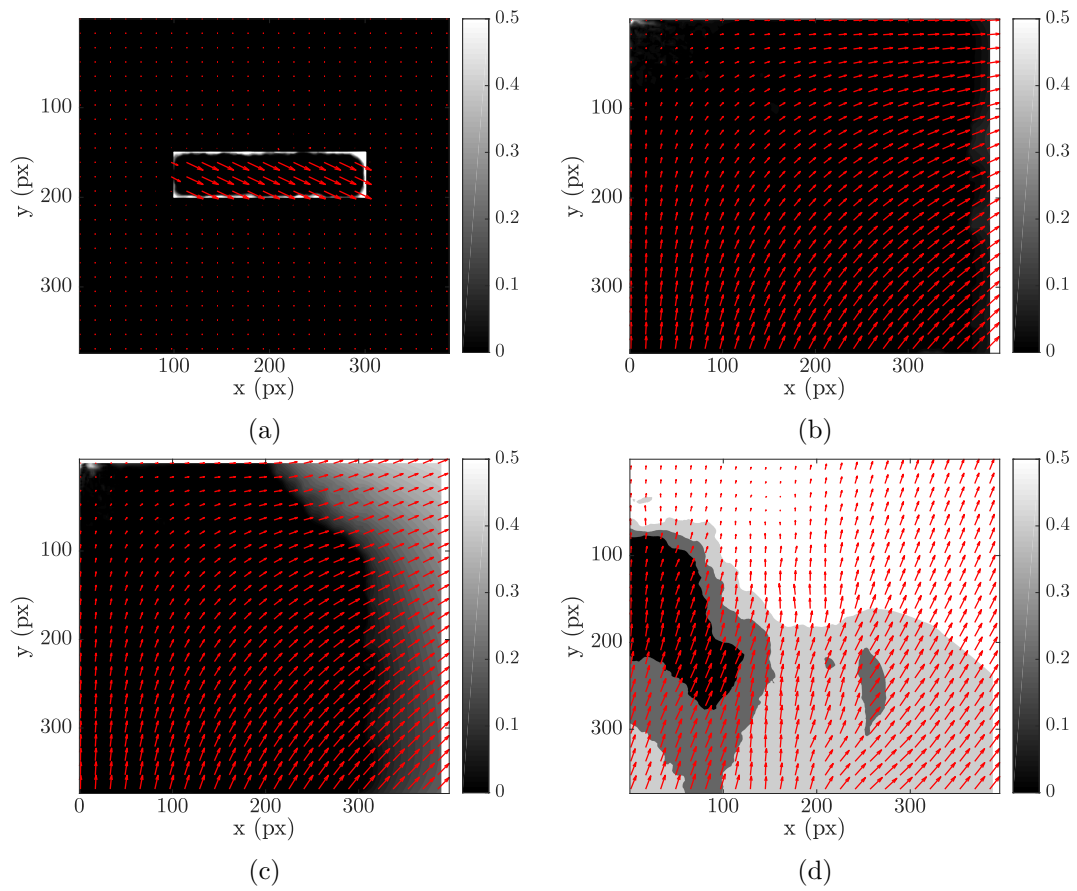


Figure 5.16: Calculated flows with optical flow code with the smallest error. Vector resolution equals the image resolution, i.e., $388 \times 374 \text{px}^2$, for clarity only 1/16 of vectors are shown (a) Block moving with uniform velocity for $\lambda = 1.00$, average value vectors surrounding flow is $3.55 \cdot 10^{-2} \text{px}$. (b) Stagnation flow with $A = 1$ for $\lambda = 129$. (c) Stagnation flow with $A = 5$ for $\lambda = 27.8$. (d) Stagnation flow with $A = 10$ for $\lambda = 27.8$.

also a distinct movement from the left to the right is visible. This can be explained by the fact that the cameras were viewing the scene from a different angle. As the smoke plume is wider than the laser sheet, the particles surrounding the laser sheet also scatter some of the light. This is visible in the images in some of the lower intensity regions. Since the cameras view the scene from a different angle, camera 1 sees a different portion of smoke outside the sheet compared to camera 2. Because the smoke particles are smaller than the wavelength of light, the individual particles are not visible in the images. Instead only a mist of the scatter is visible. This mist is present within several layers and regions of lower intensities in the laser sheet may appear as higher intensity regions due to addition of scatter from regions outside the laser sheet. Therefore it is extremely difficult to filter the scatter from the regions outside the sheet out the images. Unfortunately this artefact is present in all the data and induces apparent movement in the images, suggesting a movement which has nothing to do with the airflow.

Despite this artefact analysis was still performed to explore how the code deals with the real data. Runs were conducted with $\lambda = [1, 27, 40, 129]$, the best λ s identified in previous section and the default λ of the optical flow program. Figure 5.18 shows the calculated optical flow for $\lambda = 129$. Vectors were removed in the calculations where the background was removed. The other results are shown in appendix D. The flow present between the image pairs is unknown and can only be evaluated by visual inspection. This is very difficult, especially for such a dense vector field. From visual inspection no obvious spurious vectors were detected, only where no smoke is visible in the image and vectors are interpolated from the edges of the smoke. However, the main horizontal velocity component should be around $\sim 3.6\text{m/s}$ but the horizontal component of the calculated vectors is around $\sim 5.9\text{m/s}$, evaluated at 5 locations in the vector fields. Approximately 1.5 times larger! A manual evaluation, at 5 similar locations, of the horizontal displacement gives a horizontal component of around $\sim 5.8 - 6.7\text{m/s}$. It is not understood where these large differences come from.

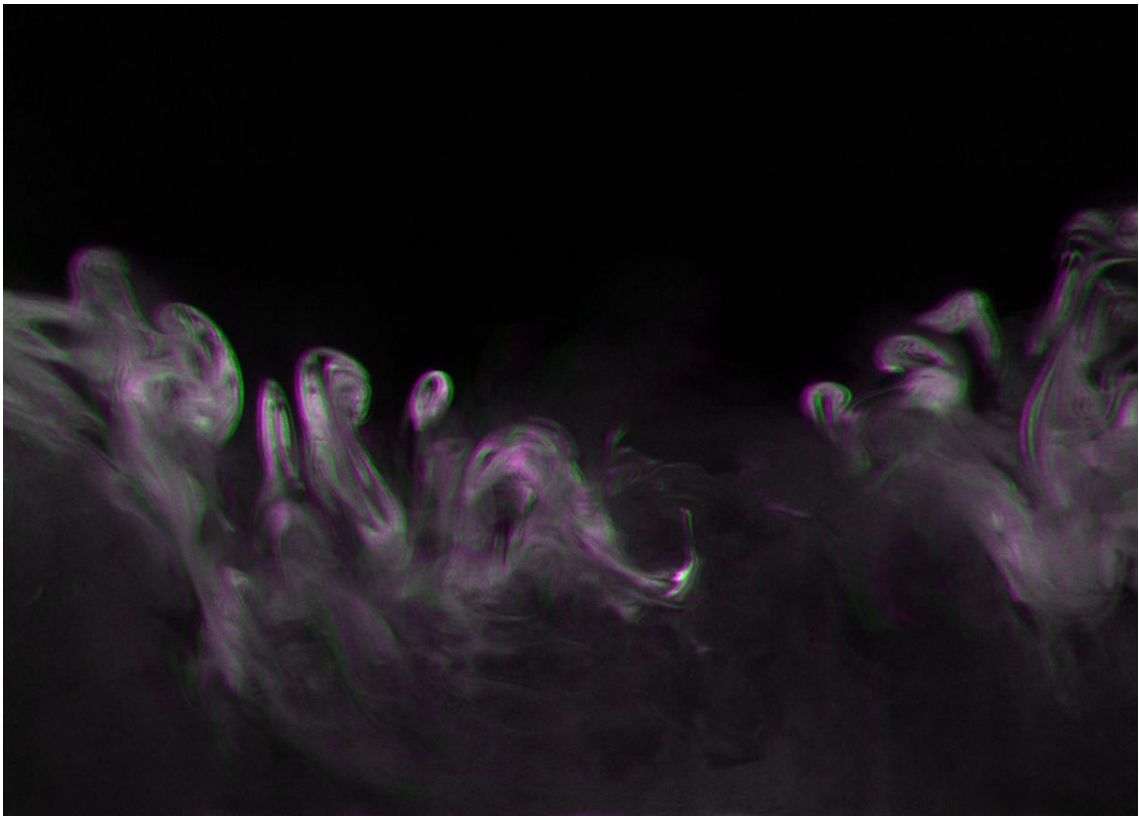


Figure 5.17: Fused image pair for $U_\infty = 3.6\text{m/s}$. Flow is from right to left. First image is green, second image is purple.

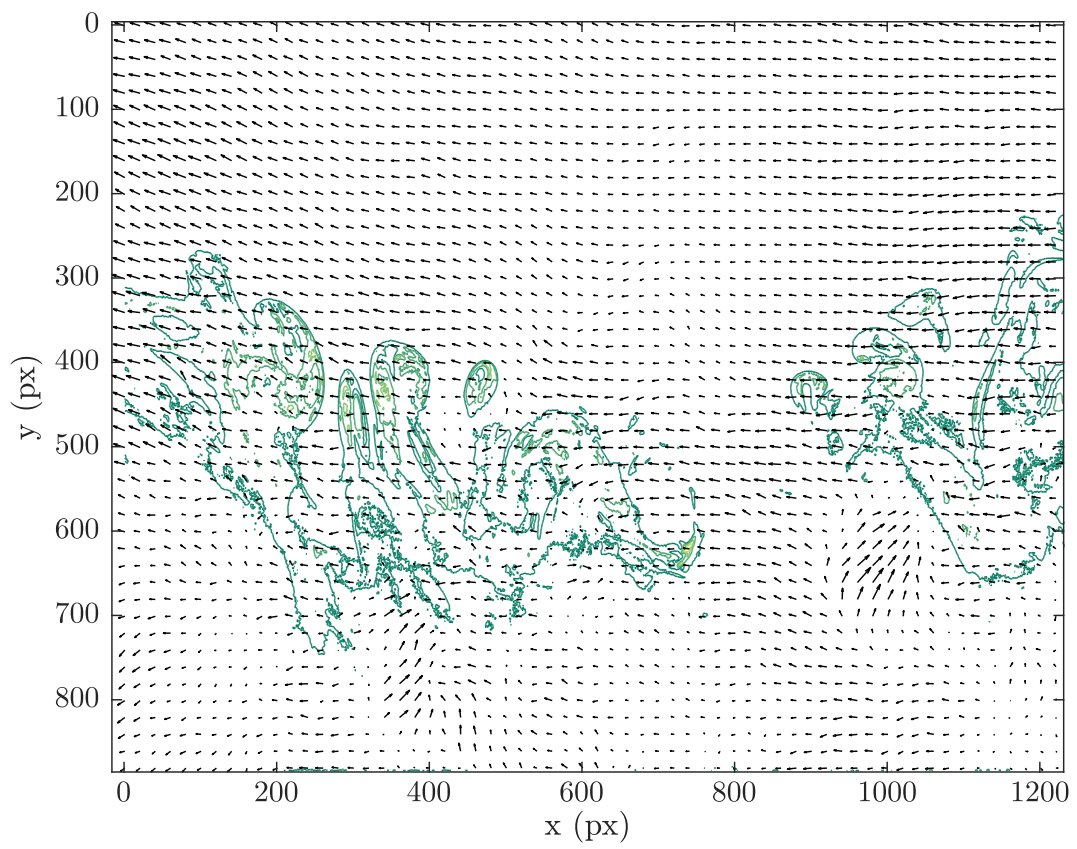


Figure 5.18: Calculated flows with optical flow code with $\lambda = 129$. For clarity only 1/20 of vectors are shown

Chapter 6

Discussion

The aim of current study was to develop a quantitative flow visualization setup using relative simple devices to study airflow around beach houses. Due to artefacts in the data, as described in section 5.3.4, it was not possible to obtain a velocity field which provides quantitative information of the flow field. In this chapter first the 4 distinct elements which are part of the quantitative flow visualisation setup are evaluated and the limitations are discussed. It should be noted that the selection of the used devices was limited to what was available and arrangeable. After that user convenience and limitations of the quantitative flow visualization setup are compared to more advanced equipment. Hereafter the selection of the optical flow algorithm is discussed. Finally some practical issues regarding the experiments are reported.

6.1 Limitations of the quantitative flow visualization setup

Tracer particles Propylene glycol vapour was used as tracer particles and injected into the flow by means of a smoke wand. The smoke generator was originally designed for qualitative flow visualization and the feasibility of using this in a quantitative flow visualization setup was investigated during present research.

Due to the fact that the particle size of the vapour drops were smaller than the wavelength of the light, no individual particles are visible in the image recordings. Because of this aspect the foreground and background could not successfully be filtered.

The location of injection was sensitive to the wind velocity, for a higher velocity the smoke wand had to be inserted further into the test section. This implies that for every experiment the location of injection had to be determined, which complicated the experiments.

The vapour plume thickness was sensitive to wind velocities, i.e., higher velocities resulted in a thinner plume. Consequence of this is that a smaller area of the flow is visualized for higher velocities and a smaller amount of scatter being available resulting in lower light intensities in the images. Furthermore the thickness of the plume was finite limiting the height of the area visualized.

As described in chapter 2 bluff body flow is characterized by circulation zones.

The pressure gradients which arise due to the vortices present in these circulation zones affect sediment transport. Therefore these circulation zones are areas of interest. It was observed during the experiments and from the data that the smoke smears out quickly in these zones, which results in small density gradients and thus small image intensity gradients. This complicates image analysis for these areas in the flow.

It should be noted that it was not possible to investigate other type of tracer particles. Besides the availability of devices, the anechoic chamber of the closed wind tunnel requires that no residue of tracers are allowed. Using solid particles, e.g. corn starch as used by Ryerson and Schwenk (2012), was therefore not possible.

Imaging device As imaging devices two basler cameras were used. As a consequence of using two cameras, the cameras were to view the scene from a different angle. In combination with the vapour plume to mark the flow, this resulted in artefacts in the data, as described earlier. Because the foreground and background could not successful be removed, the combination of using 2 cameras with vapour as marker did not succeed in capturing good quality data.

As there were no 2 equal optics available for the cameras it was necessary to use 2 different optics. The optics used had different aperture stops and one of the optics suffered from focussing issues. These aspects induced differences in the image pairs, complicating image analysis.

Illumination source At the start of the experiments two laser diodes modified with line optics were used to create the light sheet. The vapour particles have different scatter properties with respect to the difference in wavelength and spectral response of the cameras is also different for the different wavelengths. This however can be optimized by choosing the power of the lasers such that the image intensity of the two image pairs is approximately equal.

These lasers were designed for a relative high power output but not for a perfect beam profile. This means that the shape of the beam is not a tiny dot but has a more ellipse shape. The smallest size this can be focussed to limits the thickness of the line which can be created with line optics. The line was thin enough for current conditions.

Control system The in-house build timer box by F.B. Segerink (Optical Sciences group, University of Twente) showed good performance for dual pulse recordings. The pulse widths for the laser could be set separately, as well as the time delay Δt between the pulses. The range of signals it produces were designed for current conditions, but electrical components can be replaced if an other range of signals is needed. Other type of control systems are also possible to time the system, e.g. using a micro-controller or a programmable function generator. This will increase the flexibility of the system.

Image based velocimetry Using smoke as a tracer to visualize the flow complicated the experiments and analysis. However, when studying visible flows it is not necessary to visualize this flow. Therefore the setup comprising the two cameras, the

control system and the illumination sources excluding the smoke generator should be suitable to study visible fluid dynamics, e.g. droplet (impact) dynamics.

6.2 More advanced equipment

Up to a certain extent it was shown that it is feasible to design an image based velocimetry system using relative simple devices, although the specific components of the setup deserve further attention for it to fulfil all criteria. If all components are optimized it is still evident that this system is more complicated to use than a more advanced PIV apparatus. Furthermore the range of flow velocities which can be studied is limited by the amount of available light due to scatter of the particles. In this case the shortest pulse widths which generated enough signal in the images was limited to $17.5\mu\text{s}$, and therefore limits the maximum flow velocity which can be studied. There will always be a trade-off between price and user convenience.

6.3 Optical flow algorithm

In the present study the optical flow algorithm based on the Horn and Schunck (1981) method was used. The reason to use this algorithm was the fact that it was an open source tool and readily available to use. It was beyond the scope of present investigation to develop an algorithm ourselves. However, this optical flow method was based on a global method using a brightness and smoothness assumption. Other optical flow methods exist which are partly based on a global method (brightness assumption) and a local method (e.g., feature or edge tracking). In the view of our data the latter type of OFE might show a better performance.

6.4 Practical issues

Plane of interest For practical reasons, only planes parallel to the flow were subject to investigation during the experiments. The plane perpendicular to the flow is also interesting for investigation, as it would be possible to study the horseshoe vortex downstream of the obstacles. It is complicated to study this plane because the main velocity component is perpendicular to this plane. This means that the particles will have travelled very fast through the light sheet. For one to be able to study this plane a high speed system is necessary with very powerful lasers because the illumination and exposure times are limited by very small time scales.

Planar based velocimetry When using planar image based velocimetry, one can only study 2 components of the flow. If out of plane components are present, the obtained velocity field will not reflect the real velocities of the flow. This assumption might be valid for the center plane where the orientation of the houses is 0° degrees, for symmetry reasons. This assumption however is not valid for other orientation of the houses or other orientations of the house array.

Chapter 7

Conclusions & recommendations

In this chapter first concluding remarks are given on the first three objectives described in section 1.4. As noted before objectives 4 and 5 have not been completed, therefore the aim of present study was not fulfilled. The conclusions are presented as answers to the three research questions formulated in section 1.4. Hereafter some recommendations are given for future research.

7.1 Conclusions

To what extend can smoke be used as a tracer particle for a quantitative flow visualization setup?

Smoke in the form of propylene glycol vapour was used as a tracer particle in the visualization setup. The vapour particles were smaller than the wavelength of light, as a consequence of this no individual particles were visible in the images. Only a mist due to the scatter of the particles was visible. Due to the three-dimensional nature of the smoke plume and the scatter nature of the particles the foreground and background could not successfully be removed. The fact that the 2 cameras used had to view the scene from different angles induced an extra movement from image 1 to image 2 which had nothing to do with the airflow. Therefore smoke as used in current configuration with 2 cameras to record the displacement pattern is not a suitable tracer particle for a quantitative flow visualization setup.

To what extend can a high speed imaging system be developed using one or two moderate speed cameras and a special control system?

A high speed imaging system was developed using 2 basler ace-1300-30gm cameras and an in-house designed and constructed timer box. The signals produced by the timer box can all be adjusted individually. The pulse width for the illumination source can be varied from 800ns – 80 μ s and the time interval can be varied from 1.5 μ s – 80 μ s. Operating frequency can be set at 1, 10 and 100Hz and features an empty slot for an other frequency. Therefore it can be used for a wide range of flow velocities, and the signal range can be modified if desired. The cameras can be set to a minimum exposure time of 28 μ s. Smaller illumination times can be achieved with shorter illumination pulses. For longer exposure times the timing can be done with the cameras and only 1 illumination source is necessary and may be continuous. The maximum frame rate of the cameras is 30fps. Therefore the system is not suitable

for time resolved analysis, only for very slow flows $< 0.1\text{m/s}$ (based on a magnification factor 0.1mm/px). The timer box showed robust performance and is easy to use.

How do different algorithms perform in translating the measured data to sufficient accurate velocity fields?

Two algorithms were evaluated. The performance of a PIV algorithm (PIVlab provided by Thielicke and Stamhuis (2014a)) was compared to an OFE algorithm (provided by Sun (2010)). The performance of both algorithms were investigated on smoke images warped with an imposed displacement field. Two different type of flows were examined. A block flow and a stagnation flow. The first type of flow resulted in a RMS error of $3.68 \cdot 10^{-1}$ and an average error of 30.4% and a vector resolution of 22×23 vectors for the calculation with PIVlab. The calculation by the OFE algorithm resulted in a RMS error of $2.66 \cdot 10^{-2}$ and an average error of 5.6% with a vector resolution equal to the image resolution of $388 \times 374\text{px}^2$. The calculation for the stagnation flow resulted in a RMS error of $9.02 \cdot 10^{-2}$ and an average error of 6.7% and a vector resolution of 10×11 vectors for the calculation with PIVlab. The calculation by the OFE algorithm resulted in a RMS error of $1.61 \cdot 10^{-2}$ and an average error of 0.9% with a vector resolution equal to the image resolution. On this type of data the OFE algorithm outperforms the PIVlab algorithm, the errors are much smaller and the vector resolution is much higher. However when applying the algorithm on the real data it tends to over estimate the velocity values.

7.2 Recommendations

7.2.1 Alternative configurations image based velocimetry

The combination of devices for the quantitative flow visualization setup used during present study has shown not to be optimal. It is worthwhile to study other possible configurations.

1. Even though using smoke as a tracer particle seems difficult, Quenot, Pakleza, and Kowalewski (1998) have successfully calculated velocity fields from sequences of smoke images. Therefore it should be possible to use smoke as a tracer. Consequently it would be interesting to investigate the option of using a RGB camera and a red and blue laser sheet. A double exposed recording can then be separated into an image pair using the properties of the Bayer filter. This aspect of a RGB camera is described in more detail in section 4.3.3.
2. An other option which still remains to explore is using larger tracer particles (e.g., helium bubbles or corn starch) in combination with a 2 camera setup and 1 illumination source forming the light sheet. The fact that individual particles will be visible in the recording makes it more feasible to remove foreground and background. The approach will then be particle based comparable to the classical PIV approach.

7.2.2 Visualization of pressure gradients

Recently a high speed imaging Schlieren setup was developed by Giskes, Verschoof, Segerink, and Venner (2016). A Schlieren technique is often used to visualize fluid density differences which cause variations in refractive index of the fluid medium. Hence it is commonly used to study supersonic flows. In the subsonic regime fluid density is assumed to be constant, however variations in refractive index may also be caused by temperature or pressure gradients. Because pressure gradients present in the flow affect sand transport it is of interest to study this. To this extend it would be interesting to investigate the possibility of re-dimensioning the Schlieren setup developed by Giskes et al. (2016) for studying pressure gradients in the low speed wind tunnel. Pressure gradients will be much smaller than in the supersonic regime, on the other hand exposure times may be a lot higher.

7.2.3 Velocity measurements and sediment transport experiments

In view of studying airflow around beach houses one could also deploy more sophisticated techniques like PIV. Planar PIV would be a suitable starting point for investing planes of symmetry. Three-dimensional approaches like stereo PIV and Tomographic PIV can be used for other planes of interest.

Nevertheless a measured velocity field will only give insight on instantaneous sand transport. The flow field will create bedforms around the houses and these bedforms will alter the flow field. In order to gain an understanding in this complex interplay, scaled sediment transport experiments can be conducted in combination with velocity field measurements. Scaled sediment transport experiments suffer from scaling issues, as there are 2 distinct length scales in the problem, the one regarding the dimensions of the house and the other one regarding the grain size of the sand. The sand cannot simply be scaled as this will alter mass and therefore transport properties. Nonetheless these experiments may give qualitative insight on the interplay of aerodynamics and sediment transport.

Appendix A

Thwaites' Method

The derivation in this appendix follows the derivation in Kundu and Cohen (2008) which is after Thwaites (1949). Thwaites' method starts off from the Von Karman momentum integral equation

$$\frac{1}{\rho}\tau_0 = \frac{d}{dx}(U_e^2\theta) + U_e\delta^*\frac{dU_e}{dx} \quad (\text{A.1})$$

where τ_0 is the shear stress on the wall, U_e is the flow outside the boundary layer, θ is the momentum thickness and δ^* is the boundary layer displacement thickness. The Von Karman momentum integral can be found from integrating the boundary layer approximations. The boundary layer approximations were derived from the Navier-Stokes equations in the assumption that variations across the boundary layer occur over much smaller length scales than variations along the boundary layer. For a detailed derivation the reader is referred to Kundu and Cohen (2008).

The Von Karman momentum integral equation is one equation with 3 unknowns. There are no extra physical laws which can be used, therefore additional relations have to be found empirically. Thwaites (1949) introduced two empirical dimensionless functions $l(\lambda)$ and $H(\lambda)$:

$$\tau_0 \equiv \mu \frac{U_e}{\theta} l(\lambda) \quad (\text{A.2})$$

$$\frac{\delta^*}{\theta} \equiv H(\lambda) \quad (\text{A.3})$$

$$\text{with } \lambda \equiv \frac{\theta^2}{\nu} \frac{dU_e}{dx} \quad (\text{A.4})$$

Multiplying eq. A.1 with $\rho\theta/\mu U_e$, rearranging and using $\mu/\rho = \nu$ gives the following result:

$$\frac{2\theta^2}{\nu} \frac{dU_e}{dx} + \frac{\theta U_e}{\nu} \frac{d\theta}{dx} + \frac{\theta^2 \delta^*}{\nu \theta} \frac{dU_e}{dx} = \frac{\theta \tau_0}{\mu U_e} \quad (\text{A.5})$$

$$\text{or } \left(2 + \frac{\delta^*}{\theta}\right) \frac{\theta^2}{\nu} \frac{dU_e}{dx} + \frac{\theta U_e}{\nu} \frac{d\theta}{dx} = \frac{\theta \tau_0}{\mu U_e} \quad (\text{A.6})$$

Using relations A.2 and A.3

$$\left(2 + H(\lambda)\right) \frac{\theta^2}{\nu} \frac{dU_e}{dx} + \frac{\theta U_e}{\nu} \frac{d\theta}{dx} = l(\lambda) \quad (\text{A.7})$$

and noticing that

$$\frac{1}{2} \frac{d\theta^2}{dx} = \theta \frac{d\theta}{dx} \quad (\text{A.8})$$

leads to

$$\left(2 + H(\lambda)\right) \frac{\theta^2}{\nu} \frac{dU_e}{dx} + \frac{U_e}{2\nu} \frac{d\theta^2}{dx} = l(\lambda) \quad (\text{A.9})$$

$$\frac{U_e}{\nu} \frac{d\theta^2}{dx} = 2 \left[l(\lambda) - \left(2 + H(\lambda)\right) \frac{\theta^2}{\nu} \frac{dU_e}{dx} \right] \equiv L(\lambda) \quad (\text{A.10})$$

Thwaites (1949) found $L(\lambda) \approx 0.45 - 6.0\lambda$ from empirical data, which is a linear relation. Inserting this leads to the following differential equation

$$\frac{U_e}{\nu} \frac{d\theta^2}{dx} = 0.45 - 6.0\lambda \quad (\text{A.11})$$

$$\frac{U_e}{\nu} \frac{d\theta^2}{dx} = 0.45 - 6.0 \frac{\theta^2}{\nu} \frac{dU_e}{dx}. \quad (\text{A.12})$$

Multiplying the result with U_e^5 and rearranging gives:

$$U_e^6 \frac{d\theta^2}{dx} + 6\theta^2 U_e^5 \frac{dU_e}{dx} = 0.45\nu U_e^5 \quad (\text{A.13})$$

$$\frac{d}{dx} (\theta^2 U_e^6) = 0.45\nu U_e^5 \quad (\text{A.14})$$

Integration of eq.A.14 leads to an equation for $\theta(x)$:

$$\int_0^x \frac{d}{dx} (\theta^2 U_e^6) dx = \int_0^x 0.45\nu U_e^5 dx \quad (\text{A.15})$$

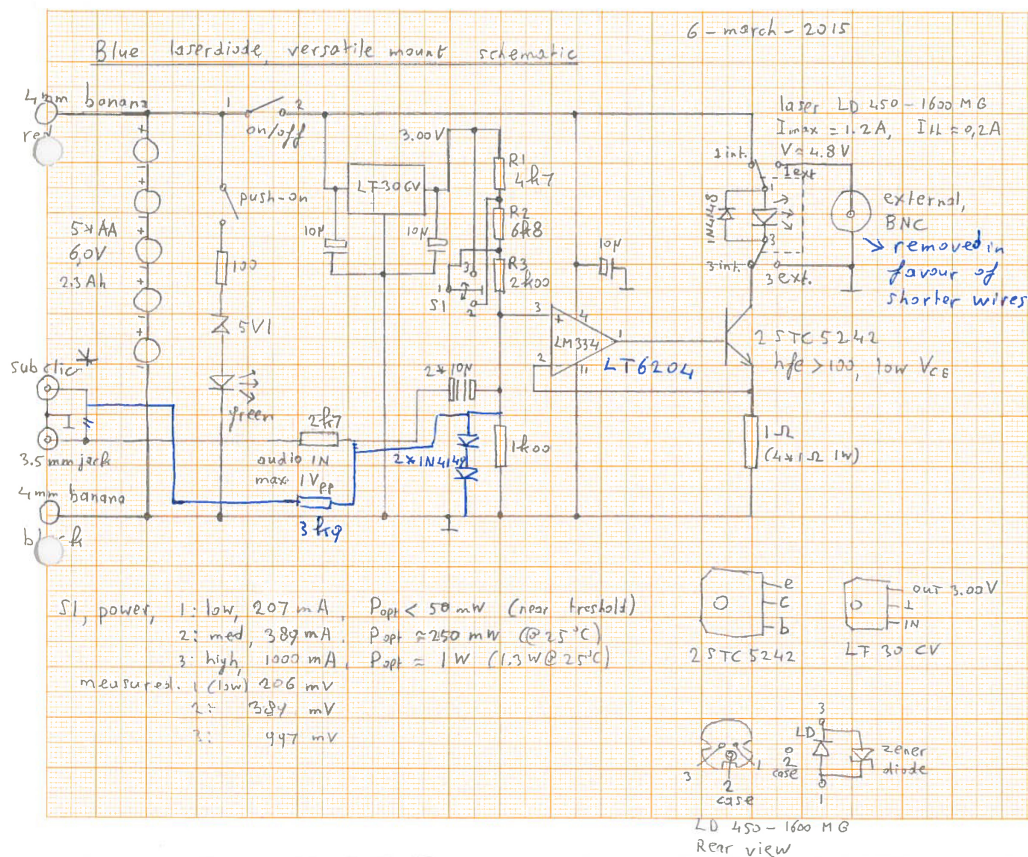
$$\theta(x)^2 U_e^6(x) - \theta_0^2 U_0^6 = 0.45\nu \int_0^x U_e^5 dx \quad (\text{A.16})$$

$$\theta(x)^2 = \frac{1}{U_e^6} \left[\theta_0^2 U_0^6 + 0.45\nu \int_0^x U_e^5 dx \right] \quad (\text{A.17})$$

From A.17 the momentum thickness can found given $U_e(x)$ and proper boundary conditions. By computing λ the boundary layer displacement thickness δ^* and shear at the wall τ_0 can be found. Boundary layer separation occurs if $\tau_0 = 0$, i.e. when $l(\lambda) = 0$, and thus the location of a separation point can be approximated using Thwaites' method.

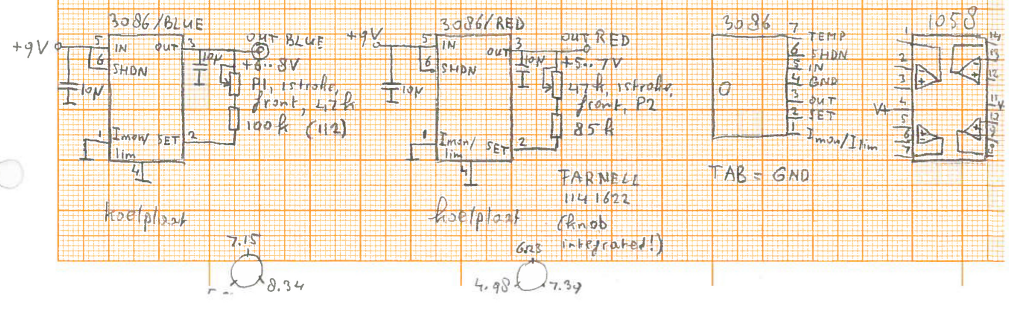
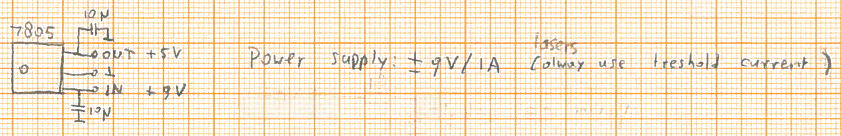
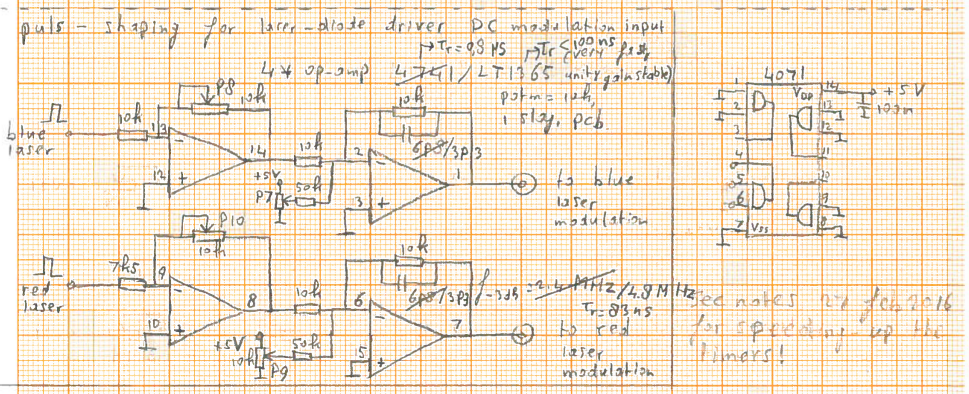
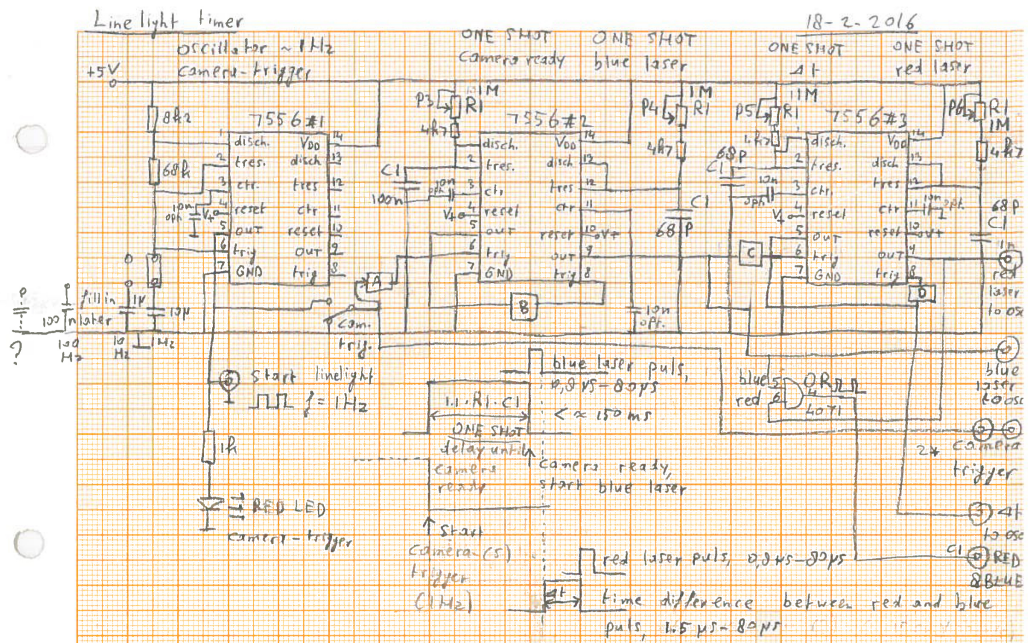
Appendix B

Laser diode and timer box schematics



*Modified 16 feb. 2016:

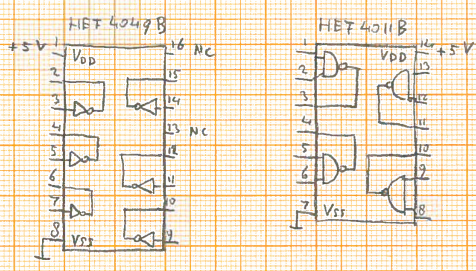
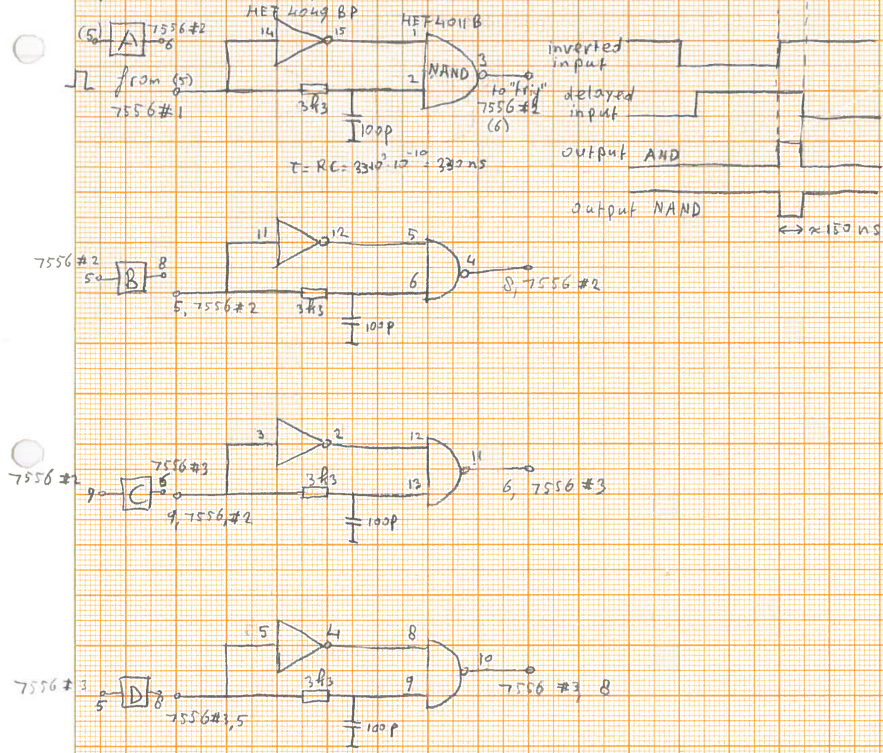
- Sub diode input connected to LM334 "+" input by 3kΩ.
 - useful for modulating the output power, ~2.5V peak needed
 - for 90% modulation, 6V power supply. Rise time ~2µs
 - Further modified with laser on-off LT6202 + protection diodes
- + shorter wiring 9-march-2016 (clipping) 7-march-2016



line light timer schematics part II

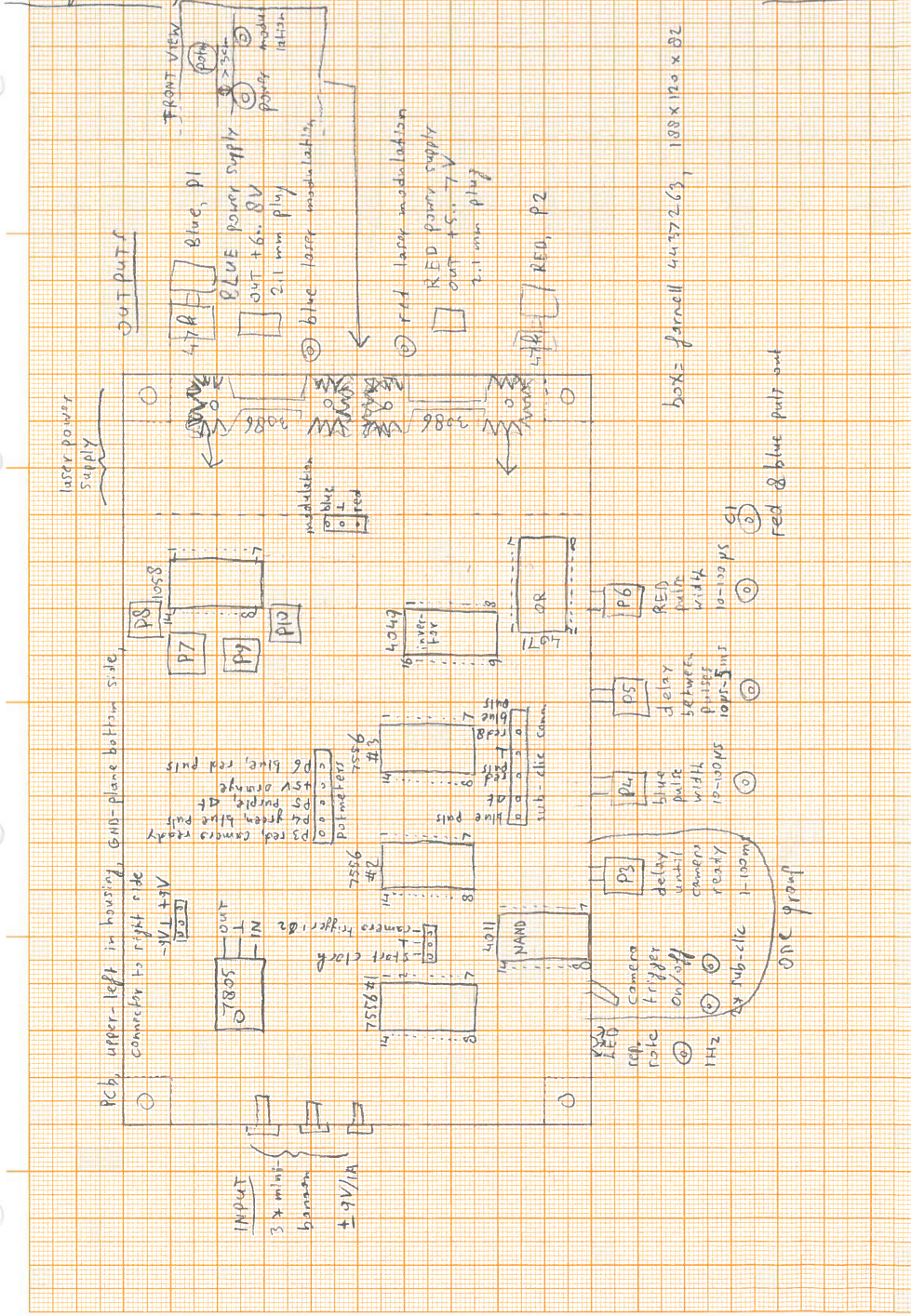
24 feb 2016

negative edge trigger for 7556 (if "trig" = low, "out" = high!)



line light timer layout

19-2-2016



box = jarnell 4437263, 188x120x82

red & blue put out

Appendix C

Vortex detection algorithm

The code finds vortex centres as follows:

Sign detection First 2 matrices are computed, containing the sign values for the u - and v -component. Since we're working with matrices with finite cell sizes, the line where the sign changes lays somewhere in between these matrix entries. For this reason is chosen to compute the contour lines for values of 1 and -1. Using the `DiscreteFrechetDist` function provided by Danziger (2013) the similarity between the lines is found, and lines corresponding to each other are paired, i.e. $u+$ with $u-$ and $v+$ with $v-$.

Intersection points From here on intersection points are found using the `lineSegmentIntersect` function provided by Erdem (2010). Intersections are only searched between combinations of $u\pm$ and $v\pm$ lines. The intersection points are grouped in sets of four and arranged in a square 2x2 matrix. If the intersection point is not on a grid point, linear interpolation is performed to find the corresponding velocity components.

Vortex check Looking only at the sign change of the velocity components is not sufficient to identify if a vortex is present. The sign values of the u -component should always be rotated 90° degree clockwise with respect to the sign value of the v -component. Furthermore, the sign of the u -component should not change in horizontal x -direction. If the velocity components fulfil these constraints, a vortex is present.

Vortex center detection If a vortex is present, linear interpolation is used to find the center points, i.e. the point is found where $u = 0$ on the lines $v+$ and $v-$ and the point where $v = 0$ on the lines $u+$ and $u-$. Thus for $u = 0$ two points are found and for $v = 0$ two points are found. Both pairs of points are connected and the intersection between the two lines are found. This is the center of the vortex. Note that the code can only find the smallest scale of vortices.

Appendix D

Optical flow vector fields

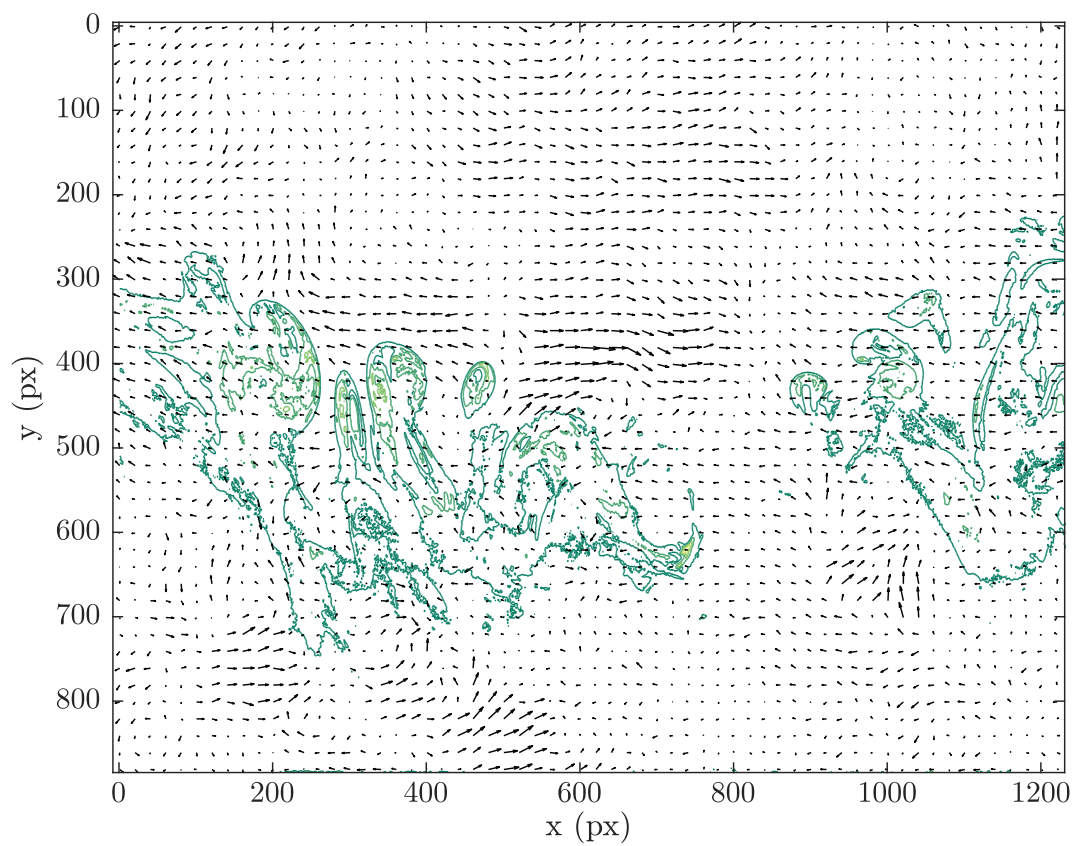


Figure D.1: Calculated flows with OFE code with $\lambda = 1$. For clarity only 1/20 of vectors are shown.

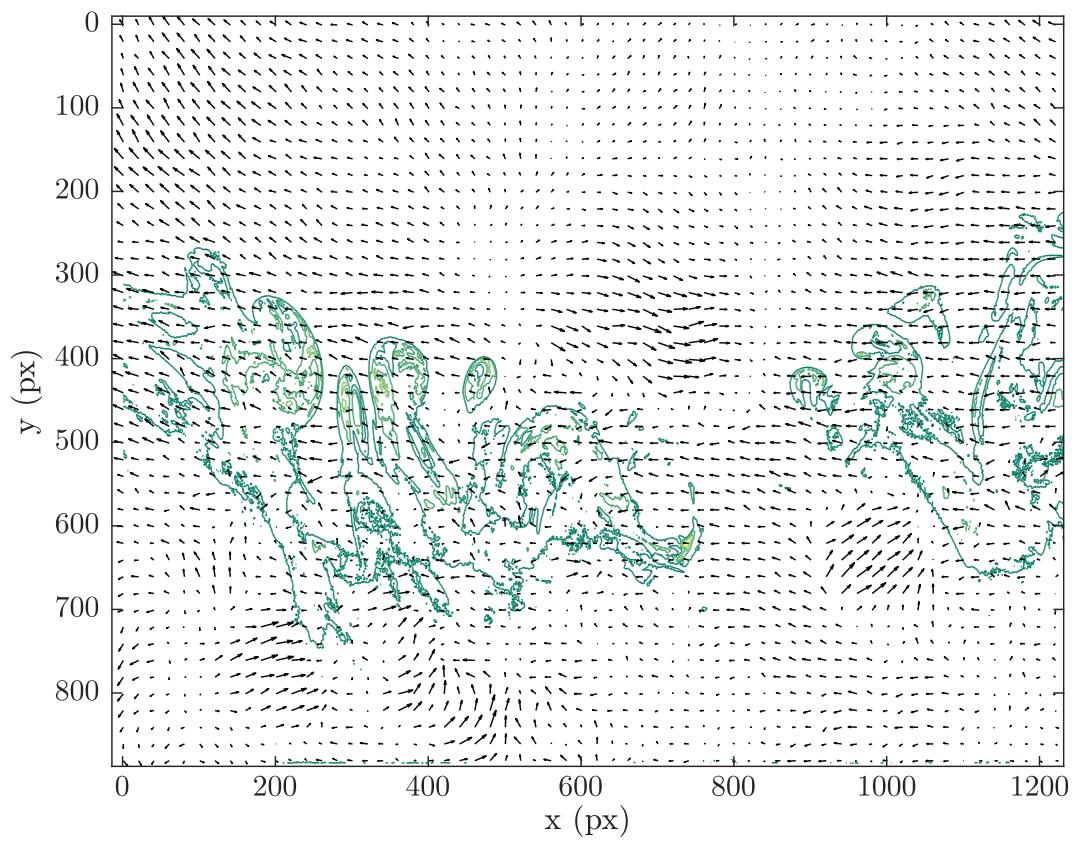


Figure D.2: Calculated flows with OFE code with $\lambda = 27$. For clarity only 1/20 of vectors are shown.

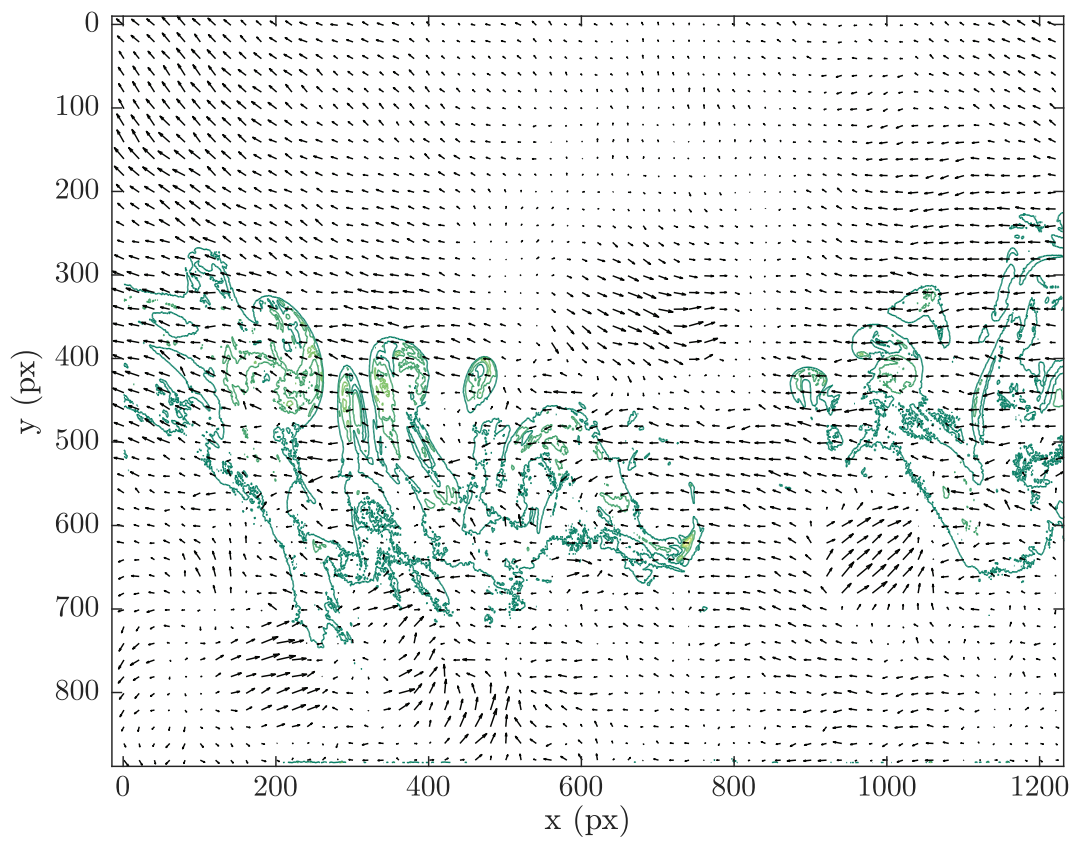


Figure D.3: Calculated flows with OFE code with $\lambda = 40$. For clarity only 1/20 of vectors are shown.

References

- Becker, S., Lienhart, H., & Durst, F. (2002). Flow around three-dimensional obstacles in boundary layers. *Journal of Wind Engineering and Industrial Aerodynamics*, *90*, 265279.
- Bruun, H. H. (1995). *Hot-wire anemometry: principles and signals* (1st ed.). New York, USA: Oxford University Press.
- Calluaud, D., Davd, L., & Texier, A. (2005). Vortex shedding process investigation downstream a surface mounted block. *Journal of Visualization*, *8(2)*, 99-108.
- Castro, I. P., & Robins, A. G. (1977). The flow around a surface-mounted cube in uniform and turbulent streams. *Journal of Fluid Mechanics*, *79(2)*, 307-335.
- Danziger, Z. (2013, May). *Discrete frechet distance*. Matlab code. (Retrieved 07.04.2016 from <http://nl.mathworks.com/matlabcentral/fileexchange/31922-discrete-frechet-distance/content/DiscreteFrechetDist>)
- D'Errico, J. (2009, June). *Slm - shape language modeling*. Matlab code. (Retrieved 11.04.2016 from <http://nl.mathworks.com/matlabcentral/fileexchange/24443-slm-shape-language-modeling>)
- Erdem, U. M. (2010, April). *Fast line segment intersection*. Matlab code. (Retrieved 09.05.2016 from <http://nl.mathworks.com/matlabcentral/fileexchange/27205-fast-line-segment-intersection>)
- Fleet, D., & Weiss, Y. (2005). Optical flow estimation. In N. Paragios, Y. Chen, & O. Faugeras (Eds.), *Mathematical models in computer vision: The handbook* (p. 239-258). Springer.
- Giancoli, D. C. (1998). *Physics: principles with applications* (5th ed.). New Jersey, USA: Prentice Hall.
- Giskes, E., Verschoof, R. A., Segerink, F. B., & Venner, C. H. (2016). *Schlieren study of a sonic jet injected into a supersonic cross flow using high-current pulsed leds*. (Manuscript submitted for publication)
- Horn, B., & Schunck, B. (1981). Determining optical flow. *International Journal of Computer Vision*, *17*, 185-203.
- Hultmark, M., & Smits, A. J. (2010). Temperature corrections for constant temperature and constant current hot-wire anemometers. *Measurement Science and Technology*, *21*, 105404.
- Kannuluik, W., & Carman, E. (1951). The temperature dependence of the thermal conductivity of air. *Australian Journal of Scientific Research, Series A: Physical Sciences*, *4*, 305-315.
- Kundu, P. K., & Cohen, I. M. (2008). *Fluid mechanics* (4th ed.). Burlington, USA: Academic Press Elsevier.
- Kustlijnkaarten 2015* (Tech. Rep.). (2014). Rijkswaterstaat.

- Lacey, R. W. J., & Rennie, C. D. (2012). Laboratory investigation of turbulent flow structure around a bed-mounted cube at multiple flow stages. *Journal of Hydraulic Engineering*, *138*(1), 71-84.
- Lawson, T. (2001). *Building aerodynamics* (1st ed.). London, UK: Imperial College Press.
- Lim, H. C., Castro, I. P., & Hoxey, R. P. (2007). Bluff bodies in deep turbulent boundary layers: Reynolds-number issues. *Journal of Fluid Mechanics*, *571*, 97-118.
- Lim, H. C., & Ohba, M. (2014). Interference effects of three consecutive wall-mounted cubes placed in deep turbulent boundary layer. *Journal of Fluid Mechanics*, *756*, 165-190.
- Luo, S. C., Chew, Y. T., & Ng, Y. T. (2003). Characteristics of square cylinder wake transition flows. *Physics of Fluids*, *15*, 2549-2559.
- Martinuzzi, R., & Tropea, C. (1993). The flow around surface-mounted, prismatic obstacles placed in a fully developed channel flow. *Journal of Fluids Engineering*, *115*, 85-92.
- Martinuzzi, R. J., & Havel, B. (2000). Turbulent flow around two interfering surface-mounted cubic obstacles in tandem arrangement. *Journal of Fluids Engineering*, *122*, 24-31.
- Martinuzzi, R. J., & Havel, B. (2004). Vortex shedding from two surface-mounted cubes in tandem. *International Journal of Heat and Fluid Flow*, *25*, 364372.
- McClean, J. F., & Summer, D. (2014). An experimental investigation of aspect ratio and incidence angle effects for the flow around surface-mounted finite-height square prisms. *Journal of Fluids Engineering*, *136*, 1-10.
- McHugh, S. (n.d.). *Digital camera sensor sizes*. Cambridge in colour. (Retrieved 03.2016 from <http://www.cambridgeincolour.com/tutorials/digital-camera-sensor-size.htm>)
- McKeona, B. J., Comte-Bellot, G., Foss, J. F., Westerweel, J., Scarano, F., Tropea, C., ... Cuerva, A. (2007). Velocity, vorticity, and mach number. In C. Tropea, A. L. Yarin, & J. F. Foss (Eds.), *Springer handbook of experimental fluid mechanics* (p. 215-448). Springer.
- Narasimha, R., & Prasad, S. N. (1994). Leading edge shape for flat plate boundary layer studies. *Experiments in Fluids*, *17*(5), 358-360.
- Pattenden, R. J., Turnock, S. R., & Zhang, X. (2005). Measurements of the flow over a low-aspect-ratio cylinder mounted on a ground plane. *Experiments in Fluids*, *39*, 1021.
- Quenot, G., Pakleza, J., & Kowalewski, T. (1998). Particle image velocimetry with optical flow. *Experiments in Fluids*, *25*, 177-189.
- Raffel, M., Willert, C., Werely, S., & Kompenhans, J. (2007). *Particle image velocimetry: A practical guide* (2nd ed.). Springer.
- Ryerson, W. G., & Schwenk, K. (2012). A simple, inexpensive system for digital particle image velocimetry (dpiv) in biomechanics. *Journal of Experimental Zoology*, *317*, 127-140.
- Sakamoto, H. (1982). Flow around a cubic body immersed in a turbulent boundary layer. *Journal of Wind Engineering and Industrial Aerodynamics*, *9*, 275-293.
- Sakamoto, H., & Haniu, H. (1987). Aerodynamic forces acting on two square prisms placed vertically in a turbulent boundary layer. *Journal of Wind Engineering*

- and *Industrial Aerodynamics*, 31, 41-66.
- Smits, A. J., & Zagarola, M. V. (2005). Applications of dense gases to model testing for aeronautical and hydrodynamic applications. *Measurement Science and Technology*, 16, 17101715.
- Sun, D. (2010, October). *Optical flow code*. Matlab code. (Retrieved 13.10.2016 from http://cs.brown.edu/~dqsun/code/cvpr10_flow_code.zip)
- Sun, D., Roth, S., & Black, M. (2014). A quantitative analysis of current practices in optical flow estimation and the principles behind them. *International Journal of Computer Vision*, 106(2), 115-137.
- Sychev, V. V., Ruban, A. I., Sychev, V. V., & Korolev, G. L. (1998). *Asymptotic theory of seperated flows* (1st ed.). New York, USA: Cambridge University Press.
- Thielicke, W., & Stamhuis, E. (2014a, March). *Pivlab - time-resolved digital particle image velocimetry tool for matlab (version: 7.10)*. Matlab code. (Retrieved 01.07.2016 from <http://dx.doi.org/10.6084/m9.figshare.1092508>)
- Thielicke, W., & Stamhuis, E. (2014b). Pivlab towards user-friendly, affordable and accurate digital particle image velocimetry in matlab. *Journal of Open Research Software*, 2(1), e30.
- Thwaites, B. (1949). Approximate calculation of the laminar boundary layer. *Aeronautical Quarterly*, 1(3), 245-280.
- User's manuel for gige cameras* (Tech. Rep. No. AW000893). (2015, October). Basler.
- van de Graaff, J., van Gent, M., Boers, M., Diermanse, F., Walstra, D., & Steetzel, H. (2007, May). *Technisch rapport duinafslag* (Tech. Rep.). WL—Delft Hydraulics and Alkyon and TU Delft.
- Wang, H. F., & Zhou, Y. (2009). The finite-length square cylinder near wake. *Journal of Fluid Mechanics*, 638, 435-490.
- Willert, C., Stasicki, B., Klinner, J., & Moessner, S. (2010). Pulsed operation of high-power light emitting diodes for imaging flow velocimetry. *Measurement Science and Technology*, 21, 075402-11.